Lightning Parameterization and Prediction: Conventional and Data-Driven Approaches

Wei-Yi Cheng

A dissertation
submitted in partial fulfillment of the
requirements for the degree of

Doctor of Philosophy

University of Washington

2021

Reading Committee:

Daehyun Kim, Chair

Dale Durran

Joel A. Thornton

Program Authorized to Offer Degree:
Department of Atmospheric Sciences

University of Washington

Abstract

Lightning Parameterization and Prediction: Conventional and Data-Driven Approaches

Wei-Yi Cheng

Chair of the Supervisory Committee:
Dr. Daehyun Kim
Department of Atmospheric Sciences

Lightning is a key component of Earth's weather and climate system, and its impact on our daily life will be increasingly important going into the future. An accurate lightning forecast is therefore critically important. However, lightning is still poorly represented in the numerical weather and climate models, because the physical mechanisms of lightning are not yet fully understood partially due to the lack of high-quality lightning observations. The recent progress in the lightning observations and machine learning (ML) techniques have provided a new opportunity to improve the understanding of lightning mechanisms and to improve the representation of lightning in numerical models. By taking advantage of the rich lightning observations from World-Wide Lightning Location Network (WWLLN), this study aims to better understand the relationship between lightning and environmental conditions and to explore the potential for improving lightning prediction using data-driven approaches.

I investigate the relationship between convective available potential energy (CAPE), precipitation, the number and size of storms and overshooting tops, and lightning stroke density (f) over the Central America region. It is found that the storm size required to produce lightning appears to be disproportionately high in the low-CAPE regime, which leads to a CAPE-threshold feature for lightning over the ocean. I show that applying the CAPE threshold for lightning over the ocean can improve the performance of a CAPE-based lightning parameterization scheme.

Various ML-based lightning parameterization methods are implemented by using grid-scale variables available from reanalysis data as inputs. By using 10 years of data, our results show that the ML-based lightning parameterization methods are able to outperform an empirical lightning parameterization method in terms of capturing the spatial and temporal variability of lightning. Lastly, I will show that implementing the ML-based lightning parameterization methods can also help improve the forecast skills of f in the weather models.

TABLE OF CONTENTS

LIST OF FIGURES

LIST OF TABLES

ACKNOWLEDGMENTS

I would like to thank my advisor, Daehyun Kim for his continued support and help throughout this project, as well as my committee: Chris Bretherton, Dale Durran, Joel Thornton, Shuyi Chen, and Robert H. Holzworth. I would also like to thank my reading committee, Daehyun Kim, Dale Durran, and Joel Thornton for their comments on this document. This work was supported by the NASA MAPP program (80NSSC17K0227), NOAA MAPP program (NA18OAR4310276), NOAA CVP program (NA18OAR4310300), DOE RGMA program (DE-SC0016223), and KMA R&D program (KMI2021-01210). The CNN training computation were run at Chonnam National University, Gwangju, South Korea.

DEDICATION

This work is dedicated to my family and friends, who have supported me endlessly.

Chapter 1

INTRODUCTION

1.1 Historical overview of lightning and human civilization

Lightning is one of the most powerful natural phenomenan on earth, which has greatly impacted the development of human civilization via various aspects since as early as the existence of mankind. During the Lower Paleolithic, the lightning-induced wildfires, which is the primary source of natural fires, provided a source of warmth and lighting, and protection from predators. It is believed that the ability to make use of the fire from wildfires leads to the rise of Homo erectus from its more primitive ancestors (Wrangham et al., 1999). The tropical forest with high potential of thunderstorms, therefore, became the primary habitat for ancient human before the time of fire could be controlled, where the human community and society was developed (Goudsblom, 1992).

Because of its destructive power and fascinating appearance, lightning has long been painted with a mysterious color and considered a spiritual element since the beginning of written history. As ancient humans sought answers about the natural world, lightning became an integral part of the superstitions and early religions in almost every early civilization. Early Greeks believed that lightning was a weapon of Zeus. Thunderbolts were believed to be invented by Minerva, the goddess of wisdom. Since lightning was a manifestation of the gods, any spot struck by lightning was regarded as sacred. Greek and Roman temples often were built at these sites, where the gods were worshipped in an attempt to appease them (Viemeister, 1961). In ancient Chinese culture, people struck by lightning were seen as being punished by Chinese dragon. The early Chinese literature also hints at that the origin of the Chinese dragon can be related to lightning, as the figure and the description of these dragons resemble the shape of lightning flashes in many ways (Wang and He, 2011).

As science and technology advance, the better understanding of its physical processes gradually lifted the veil of mystery off of lightning. However, even with the advanced technology that now exists, lightning is still currently one of the most lethal natural phenomena, and has profound impacts on human society. In this chapter, I will review the specific impacts of lightning on the present-day human society, including the short-term destructive hazards and the long-term climate impacts.

1.2 Lightning impacts in a changing climate

1.2.1 Fatalities and economic impacts

Recent studies estimated that the total number of global annual lightning fatalities ranges from 6,000 to 24,000 per year (Holle and Lopez, 2003; Cardoso et al., 2011). Holle (2016) presented a comprehensive comparison of reported lightning fatalities from 23 countries for an average duration of 10 years, The national reports offer a clear distinction between developing and developed countries in the numbers and trends of lightning casualties. While the fatalities and injuries are mostly concentrated in developing countries, the economic impacts of lightning on developed countries are not negligible. In the United States alone, lightning is responsible for economic loss exceeding 1$ billion per year, with damages from wildfires, disrupted power supply and transportation, and buildings destruction (Curran et al., 2000).

1.2.2 Forest fires

Lightning is a major cause for damage to trees and forests, either by directly killing trees on strike or by igniting fires and burning large numbers of trees with the spread of wildfires (Latham and Williams, 2001). A recent study by Abatzoglou and Williams (2016) revealed that in the western United States from 1992–2013, up to 40% of the total number of wildfires with an area larger than 0.4 ha can be associated with lightning-induced wildfires. Veraverbeke et al. (2017) focused on the boreal forests of North America during 1975-2015, and they found that lightning was responsible for over 76% of the fires with areas larger than

200 ha in the Northwest Territories, and to 87% of fires larger than 405 ha in interior Alaska.

The future trend of lightning-induced forest fire is, however, not yet clear. On a regional scale, Veraverbeke et al. (2017) predict that both ignition events and burnt areas will be increased in a warmer climate for boreal forests in North America. On a global scale, Krause et al. (2014) modeled the future trends of wildfires in different climate scenarios using the ECHAM6 GCM. They found that even in the extreme RCP8.5 scenario, the global burned area increased only by only 3.3% even though lightning frequency was calculated to increase by 21.3%. It is important to note that the forest fire forecast remains quite uncertain since the exact relationships between lightning frequency, fire occurrence and the area burnt is hard to establish. The factors impact the outcome of an ignition event by a cloud-to-ground flash, such as the terrain, tree density, precipitation, air temperature, soil moisture, and fuel availability are yet to be fully understood.

1.2.3 Transportation and renewable energy

On average, for every 3,000 hours of flight for any type of commercial transport aircraft, there will be one hit by a lightning stroke (Uman and Rakov, 2003). The effects of these lightning strikes on aircraft have been a continuing concern to aviation industry since the early days of the aviation era. While in-flight damages are known and operationally considered, the ground segment of aviation is also affected by lightning, as air-traffic control centers, communication towers and navigation beacons are extremely vulnerable to thunderstorms and lightning (Yair, 2018). Since the air travel hubs reside mostly near big cities, the urban effects on thunderstorm occurrence (discussed in the next chapter) is a serious concern for airport operations, including increasing risk of flight delays, cancellations and route disruptions.

Lightning damages are also a serious concern for cars, even though the passengers inside cars are normally protected due the Faraday Cage effect. Yanagawa et al. (2016) studied 179 incidents of vehicles struck by lightning and showed that most strikes to cars were to the antenna (15.6%) or roof (10.6%). It is important to note that the electric cars are more

vulnerable to lightning strikes than normal cars (Kanata et al., 2012). This is largely because the electrical systems can be damaged by the induced currents, and the over-voltages caused by non-direct lightning strikes is also a serious concern. As the numbers of electric cars is expected to rise, this type of risk to public safety is also expected to increase in the future (Yair, 2018).

As economy gradually adapting to sustainable energy production, the role of wind energy production is becoming increasingly important. However, the locations of wind farms in wind-prone areas make them act as triggers for direct attachment of lighting to the turbine blade. The surge of electric current often overwhelm the lightning protection systems and cause serious damages to wind turbines (Garolera et al., 2014). As a result, energy companies search for mitigation techniques to alleviate downtime and economic losses (Shohag et al., 2017). Montanyà et al. (2014) studied the incidence of lightning strikes to wind turbines in Spain, and found that the rotation of turbine blades initiated electrical discharges when thunderstorm conditions prevailed nearby. The results indicate that the rotating wind turbine blades may enhance their own vulnerability as they also act to trigger lightning.

1.2.4 Climate-chemistry feedback

Lightning is also one of the key climate-chemistry feedback mechanisms coupling changes in the climate system with changes in atmospheric constituents. Lightning has profound impacts on the composition of the troposphere through lightning-produced nitrogen oxides (LNOx). Although this source accounts for less than 15% of global surface NOx emissions from fossil fuel combustion, biomass burning and soils (Jaeglé et al., 2005), it has a disproportionately large influence on atmospheric chemistry because it is injected in the upper troposphere (DeCaria et al., 2005; Pickering et al., 1998). In that region, the longer NOx lifetime (Jaegle et al., 1998; Pickering et al., 1990) results in LNOx accounting for more than 70% of NOx in the tropics and subtropics in the upper troposphere year round, as well as more than 50% of NOx throughout the southern hemisphere where surface NOx sources are small (Grewe et al., 2001; Hauglustaine et al., 1994; Lamarque et al., 1996; Sauvage et al.,

2007). In addition, LNOx emissions dominate concentrations of upper tropospheric summertime NOx over North America (Allen et al., 2012; Cooper et al., 2007; Hudman et al., 2007).

LNOx has an O3 production efficiency 3-6 times that of surface NOx sources (Wild, 2007; Wu et al., 2007). Current models estimate that LNOx accounts for the production of 35-50% of global free-tropospheric O3 (Allen et al., 2010; Gordillo-Vázquez et al., 2019; Liaskos et al., 2015; Martin et al., 2007; Sauvage et al., 2007). LNOx has a strong influence on the budget of OH and thus the tropospheric oxidizing capacity. Labrador et al. (2004) show that OH is sensitive to LNOx emissions, which increase OH by 30% and decrease the lifetime of CH4 by 15%. Interannual variability in LNOx driven by the El-Nino-Southern Oscillation (ENSO) appears to be the main factor controlling the variability in tropical O3 and global OH concentrations (Murray et al., 2013; Turner et al., 2018).

By affecting the lifetimes of greenhouse gases (CH4 and O3) and the concentrations of aerosols, lightning plays a key role in climate-chemistry feedbacks. Changes in the mean climate impacts atmospheric chemistry through changes in thunderstorm activity and lightning frequency. In turn, the changes in atmospheric chemistry could accelerate or slow down the changes in the mean climate by affecting the concentrations of greenhouse gases (GHG) and aerosols.

Lightning-induced Wildfires also affect the carbon cycle through complex feedbacks, due to changes in the carbon sequestering capacity of the forest, the direct emission of volatile organic compounds and carbon dioxide (which in turn affect clouds and precipitation), and due to the large-scale reduction in albedo of the burnt area.

1.3 Lightning as a forecasting problem

Since lightning has significant impact on our daily life, to assess its potential threat and influence, it is critically important to have an accurate lightning forecast. On a shorter time scale (on the order of days), an accurate lightning forecast is critical to provide guidance for safety concerns. On a longer time scale (on the order of years), one must also consider how the

frequency and geographical distribution of lightning will be affected in the changing climate to navigate the policymakers in terms of urban development, transportation and energy strategy. With the on-going trends of population growth, urban expansion and greenhouse gasses production, it is certain that the future of lightning forecast, on both short and longer time scale, will become increasingly important.

Typically, the goal of lightning forecast is to predict the lightning flash rate (F; [flashes min^{-1}]), or lightning flash density (f; [flashes km^{-2} yr^{-1}]) over a certain area in advance. Since the generation of lightning can be related to the surrounding atmospheric condition (see discussion in Chapter 2), lightning forecasts are often treated as part of the forecasting of weather and climate. A wide range of numerical models have been developed and are available for the weather and climate forecasting. Examples of numerical models include numerical weather prediction (NWP) models and Earth System Models (ESMs). NWP models are atmospheric models with a horizontal resolution of about 10 - 100 km. The simulations performed using NWP models may be regional or global in scope, and are often used to make weather forecast over a short period of time (typically two weeks). Because of the chaotic nature of atmospheric dynamics, NWP models often lose all forecast skill gradually over the two-week period. ESMs, on the other hand, are numerical models with horizontal resolution of 100 km used to simulate an approximation of Earth's entire climate system over a much longer time period (typically 10 - 100 years). The spatial and temporal resolution of NWP and ESMs are often limited due to the constraints of computational resources. Therefore, many important small-scale processes are not resolvable in the models, including those that govern the generation of lightning. The unresolved sub-grid processes therefore have to be represented using the resolved variables via parameterization schemes.

Having an accurate representation of lightning is critical to have a skillful lightning forecast and simulation in both NWP and ESM. However, parameterizing lightning in numerical models is not a trivial task since the physical processes involved in the generation of lightning are extremely complex and several aspects are still uncertain. The challenges of having an accurate representation of lightning are two-fold. On one hand, the physical mechanisms

that governs the frequency of lightning are not yet fully understood. On the other hand, challenges also remain in describing the processes using resolvable variables. One critical bottleneck in advancing our knowledge of lightning mechanisms and improving the representation of lightning is the lack of observations, because lightning observations are difficult to make and often limited regionally.

Over the past decade, significant progress has been made for lightning observations, which offer a new opportunity to further our understanding of lightning mechanisms. This dissertation is aimed to improve the understanding of lightning mechanisms by utilizing the newly available rich lightning observational data, and to improve the representation of lightning in the numerical models.

The rest of this dissertation is organized as follows. The lightning parameterization problem, its history and remaining challenges associated with it are described in Chapter 2. In Chapter 3, I present the recent advance in lightning observations and machine learning techniques, and how these advances will be used in this study toward improving the representation of lightning in numerical models. A quantitative analysis of the CAPE-f relationship over the tropical ocean and land areas in the Central America based on observations will be presented in Chapter 4, which will help us better understand the physical mechanisms of lightning and provide guidance on how to improve some lightning paramterization schemes. In Chapter 5, I present the results of applying machine-learning techniques to lightning forecast and their potential advantages as compared to the physics-based lightning parameterization methods. Finally, the conclusions are provided in Chapter 6, along with some prospect on future works for continued improvement of lightning parameterization in NWP models and ESMs.

Chapter 2

REPRESENTATION OF LIGHTNING IN NUMERICAL MODELS

2.1 Physical mechanisms of lightning

While disagreement remains in the molecular and microphysical processes of lightning and its triggering process (Ziegler et al., 2001), the basic physical understanding of the thunderstorm charging processes have been established based on theory and observations. For example, it is generally accepted that the lightning flashes can only happen with a strong enough ambient electric field within the thunderstorms, which is built up from the charge separation (i.e., electrification) process (MacGorman et al., 1998).

The most popular theory for the charge separation process is the non-inductive process (Baker and Dash, 1994), which is generated through the following steps. First, the charge separation process requires the presence of various sizes of hydrometers, including the large graupel particles, ice crystal, and supercooled water droplets. Along the surface of the ice particles, there often exists a thin layer of liquid water formed by the deposition of supersaturated water vapor on ice surfaces (Asakawa et al., 2016), which is referred to as quasi liquid layer (QLL). In this QLL, there is a strong temperature gradient, which is colder in the interior and warmer on the exterior. That temperature gradient will cause the charge to be unevenly distributed, where the positively charged hydrogen atom will accumulate in the colder interior due to its smaller size, and the larger, negatively charged, hydroxide will accumulate in the exterior. In an environment with temperature below -10°C with moderate amount of supercooled liquid droplets (Jayaratne et al., 1983; Takahashi, 1978), more water droplets will be attached to larger graupel particles. When these droplets freeze, they will release latent heat and warm up the graupel, which reduce the rate of deposition on the

graupel surface, leading to a thinner QLL along the graupel surface.

Second, a key component for the the non-inductive charge separation process is the collision between the larger graupel particles and the ice crystals. After the collision, the mass of QLL will redistribute in a way that will be evenly distributed between graupel and ice crystals. Since graupel particles generally have thinner QLLs, there will be net mass transfer of QLL from ice crystal to graupel. Because the exterior of the QLL is occupied by the negatively charged hydroxide that will be redistributed to graupel more easily, there will be a net negative charge transfer from ice crystal to graupel particles. As a result, after the collision, graupel will carry a net negative charge, and the ice crystal will carry a net positive charge. Note that the direction of the charge transfer can also be sensitive to the environment temperature and the amount of supercooled water droplets (He et al., 2018).

Lastly, the presence of the convective updrafts in the thunderstorms plays an important role that helps lifting the lighter ice crystals (positively-charged) upwards, while the negatively-charged rimed particles fall downwards due to gravity. This process separates the charge in the thunderstorm clouds, leading to the classical charge distribution in thunderstorms: positive charges in the upper part of the cloud, negative charges between -25°C and -10°C. The charge transfer between ice crystals and rimed particles is often reversed when temperature is above -10°C, which may lead to a relatively thin positively charged layer from cloud base up to the -10°C level (Jayaratne and Saunders, 1984). When the in-cloud electric field reaches a certain threshold (e.g., 1 – 4 x 10^5 V/m at 6-km level, Winn et al., 1974, 1981), lightning discharges occur.

Lightning flashes can be categorized into two classes: intra/inter-cloud (IC) and cloud-to-ground (CG) lighting. The climatological ratio of IC with respect to total (IC+CG) lightning typically varies between 35% and 90% (MacGorman et al., 1998), depending on the geographical location. A large uncertainty remains as regards to what factors govern the spatial and temporal fluctuations of this ratio (Boccippio, 2002).

2.2 A brief overview of lightning parameterization methods

The basic understanding of the charge separation process described in Ch. 2.1 lay the foundation for the lightning parameterizations in numerical models. Most parameterization schemes are based on at least one of the three key components that are directly or indirectly associated with the charge separation process: (i) The size of the thunderstorm, which directly affects the electric field imposed by electrified clouds; (ii) The convective characteristics of thunderstorms, including convective updraft intensity, which separate the positively charged ice particles from the negatively charged ice particles; (iii) The collisions between different types of ice particles, which directly cause the ice particles to carry charge. While different approaches emphasize different aspects of the charge separation process, it is important to note that these approaches are not mutually exclusive in terms of the corresponding physical processes. For example, the size of thunderstorm can also be partly related to the intensity of convection. The development of each of these methods will be reviewed in more detail below, and a list of lightning parameterization schemes previously proposed in the literature are summarized in Table 2.1.

2.2.1 Size-based approaches

In a pioneering study, Vonnegut (1963; hereafter V63) conceptualize the thunderstorm as a quasi-steady-state electrical dipole, where the spatial scale of the electrical dipole is approximated by the size of the storm. V63 hypothesized that the storm electrical generator power can be used as a proxy to the lightning flash rate (F), assuming little variation of energy dissipated in each lightning flash. In V63's framework, there are two key components that decide the storm generator power: (1) The potential difference between the two dipoles, which is associated with the size of the storm; (2) The storm's charge separation process, which is associated with the non-inductive process and storm updraft velocity. This conceptual model forms the basis for the later development of parameterizations of lightning. For example, by using storm's cloud-top height as a proxy for both size and updraft velocity of

the storm, Williams (1985; hereafter W85) proposed a simple relation that relates F to the fifth-power of the storm's cloud-top height (H; $[km]$).

After finding out that the fifth-power relation cannot capture the observed land-sea lightning contrast, Price and Rind (1992; hereafter PR92) modified the power-law relation by applying logarithmic fitting to the observed lightning flash rate and cloud-top height over land and ocean separately. Based on limited observations, they came up with different parameterizations for continental and maritime lightning flash rates: $F \propto H^{4.9}$ over land and $F \propto H^{1.73}$ over the ocean.

However, Boccippio (2002, hereafter B02) demonstrated that the modification made in PR92 over ocean directly contradicts V63's theory, and leads to unrealistic predictions of oceanic updraft velocity. In an attempt to address the inconsistency, B02 proposed a few modifications to the V63's theory: (1) The charge geometry of the thunderstorm, rather than being spherical, should be closer to circular plates, as suggested by observations (Stolzenburg et al., 1998). (2) The lightning flash rates, rather than being scaled linearly as storm generator power, should be scaled with the net generator current, following charge conservation law. These proposed modifications suggested that the charge transport speed within the thunderstorm is the primary factor in deciding the lightning flash rate, and the electrical potential difference between the charge centers and the ground, as well as the size of the thunderstorms.

Regardless of its flaws pointed out by B02, the PR92 scheme has been being widely used in the global models since proposed, and has also been adopted and modified in many other lightning parameterization schemes. For example, while retaining the power-law relation to the cloud-top height, Michalon et al. (1999) modified PR92's formulation to account for the land–ocean cloud condensation nuclei (CCN) concentration differences. In an attempt to directly relate F to the strength of the convective updraft, Grewe et al. (2001) incorporated convective mass flux in the power-law relation. Yoshida et al. (2009) replaced the H with the cold-cloud depth, which is defined as the depth of the layer between the melting level and the storm top.

While being widely used and accepted, a large uncertainty remains in the the size-based lightning parameterization approach because the power-law relationship causes F to be very sensitive to even a small uncertainty in H. When studies try to verify the power-law relationship, they often come to inconclusive results (Ushio et al., 2001).

2.2.2 Approaches based on convective intensity

Another group of lightning parameterization schemes focuses on the characteristics of convection that are more directly associated with the convective intensity. Observational studies showed that F is well-correlated with some certain convective characteristics, including convective precipitation (Allen and Pickering, 2002; Meijer et al., 2001; Petersen et al., 1998; Tapia et al., 1998), CAPE (Murugavel et al., 2014; Pawar et al., 2012), cloud ice water path (Petersen et al., 2005), updraft volume (Deierling and Petersen, 2008), and precipitation ice mass (Deierling et al., 2008). Partly motivated by these observational results, lightning parameterization schemes were developed using parameters that are indicative of convective intensity. For example, Allen and Pickering (2002) proposed to use polynomial functions of convective precipitation and upward convective mass flux at 440-hPa level to estimate F.

Among the variables that are indicative of storm intensity, arguably CAPE has been most heavily investigated in connection with lightning generation mechanisms (Fuchs et al., 2015; Petersen et al., 1996). This is because CAPE is directly associated with the convective updraft velocity: By assuming the air parcel rises moist adiabatically from the surface with no entrainment and water loading, CAPE can be linked to the maximum updraft velocity a storm can produce (w_{max}; i.e., CAPE $= w_{max}^2/2$; Holton, 2004). Since updraft velocity plays a critical role in the charge separation process, it is intuitive to use CAPE as a key component in lightning parameterization. The positive correlation between CAPE and F in observations was first reported by Williams (1992) and Rutledge et al. (1992), who found that F increases rapidly with CAPE on the monthly and daily time scale using observations from multiple locations in the tropics, including Mexico, southern Brazil, Botswana, Florida, and northern Australia. Following these studies, the correlation between CAPE and lightning activity has

been repeatedly confirmed in other regions over the tropics. For example, Murugavel et al. (2014) showed that lightning activity and CAPE are well-correlated during the monsoon season over central and north India. Over Bangladesh, it is also found that CAPE and lightning flash counts is highly-correlated on monthly time scale with correlation coefficient over 0.9 (Dewan et al., 2018).

Romps et al. (2014; hereafter R14) proposed a lightning parameterization scheme that predicts F using the products of precipitation rate (P) and CAPE. When applied to the Continental United States (CONUS) area, the R14 method was able to capture the seasonal and diurnal variability of F as well as its geographical distribution (Romps et al., 2018; Tippett et al., 2019). With its high performance and simplicity, the R14 parameterization was also applied to lightning prediction in NWP models. Tippett and Koshak (2018) demonstrated that the subseasonal lightning forecast over CONUS based on the R14 method has statistically significant skill until about forecast day 15. Overall, the R14 parameterization performs better on shorter time scales (daily and monthly) than on longer time scales (annual and semi-annual; Tippett et al., 2019).

2.2.3 Ice flux-based approaches

As the computation power increases and the representation of cloud microphysics becomes more detailed in numerical weather model, another branch of lightning parameterization schemes are developed that focus on the microphysical processes of the charge separation process. This type of parameterization schemes often targets the collision of different types of ice particles in the clouds. For example, McCaul et al. (2009) proposed two simple formulations to represent lightning flash rate by accounting for the collision rate of different frozen ice hydrometeors (i.e., graupel, snow, and ice). They tested their parameterization scheme in a cloud-resolving model, and demonstrated that the model is able to capture the general character of most convective events. Dahl et al. (2011) represent F by the amount of graupel predicted by their regional model, which is used to calculate the storm-scale charging process. Finney et al. (2014) proposed a lightning parameterization method that estimates

F using the upward vertical ice flux at the level of charge separation (440 hPa level).

While the ice flux-based lightning parameterization methods adopted a more accurate physically-based approach to represent the electrification process, a thorough verification of such methods is difficult to conduct because the concentration of ice particles in clouds is difficult to observe. Consequently, most of the evaluations of such methods are performed using the model simulations. However, the model simulated convection and the convective cloud microphysics remains one of the major uncertainties in the global climate models (Zhao et al., 2016). Therefore, the applicability of the ice flux-based lightning parameterization schemes on global climate models and associated uncertainty is worthy of further investigation.

2.2.4 Hybrid approaches

New lightning parameterization schemes have been proposed recently that adopted a hybrid approach, which combines two or more aspects of the charge separation process into the parameterization formulation. For example, Lopez (2016) proposed a lightning parameterization method that relates F to three variables: (i) Q_R, the rate of collisions between graupel and other types of hydrometeors within the charge separation level, which is essentially the convective precipitation fluxes used as a proxy for the charging rate; (ii) the diluted CAPE that includes the entrainment of environmental air into the convective plume; and (iii) Z_b, the convective cloud base height, used as a proxy for the horizontal extent of the convective ascent. Lopez (2016)'s parameterization takes into account all three aspects of the charge separation process, and the formulation for lightning flash rate is: $F \propto Q_R \times \sqrt{CAPE} \times min(Z_b, 1.8)^2$. Lopez (2016) showed that their lightning parameterization scheme improves the climatology of F and its seasonal variation when compared with other types of parameterization methods.

Alternatively, Stolz et al. (2017) proposed a data-driven approach to represent lightning flash rate. By fully utilizing observations of lightning flash rate with other observational datasets, Stolz et al. (2017) thoroughly assessed the predictive power of the normalized CAPE, near-surface cloud condensation nuclei, warm cloud depth, 850-500 hPa average rela-

tive humidity, and magnitude of 1000-500 hPa vertical wind shear in capturing the variability of F in the global domain. They found that the predictor variables accounted for a significant portion of the variance in F.

While the hybrid approaches have a clear advantage in representing the charge separation process in a more comprehensive manner, a thorough verification of such methods have not yet been performed. In particular, the uncertainty of such methods is worthy of examination since the hybrid approaches still rely heavily on the model simulated convective cloud microphysics. In the next section, we will discuss the uncertainty of the future lightning projection in more details.

Table 2.1: Summary of the previously-proposed lightning parameterization schemes.

Parameterization type	Key variables	Formulation	Reference
Size-based	Cloud-top height (H)	$F_l \propto H^{4.9}$ $F_o \propto H^{1.73}$	Price and Rind (1992)
		$F_l \propto H^{5.09}$ $F_o \propto H^{4.38}$ or $F_l \propto H^{6.39}$ $F_o \propto H^{4.92}$	Boccippio (2002)
	Cold cloud depth (CCD)	$F \propto CCD^{4.9}$	Yoshida et al. (2009)
Modified size-based	Cloud droplet number concentration (C)	$F \propto C^{2/3}H^5$	Michalon et al. (1999)
	Updraft vertical velocity (w), cloud thickness (d)	$F \propto (w \times \sqrt{d})^{4.9}$	Grewe et al. (2001)
Convective intensity-based	Convective precipitation (P)	$F_{CG} \propto f(P)$	Allen and Pickering (2002)
	Convective mass flux (M)	$F_{CG} \propto f(M)$	
	Convective available potential energy (CAPE)	$F \propto f(CAPE)$	Williams (1992); Pawar et al. (2012)

	CAPE, P	$F \propto CAPE \times P$	Romps et al. (2014)
Ice flux-based	Upward graupel flux at -15°C level (F_1); Vertical integral of graupel, snow, and cloud ice (F_2)	$F \propto F_1$, or $F \propto F_2$	McCaul et al. (2009)
	Graupel mass concentration (A), graupel- and ice-mass fields (ΔQ), terminal fall speed of the graupel (v_g)	$F \propto \frac{Av_g}{\Delta Q}$	Dahl et al. (2011)
	Upward vertical ice flux at 440-hPa level (ϕ_{ice})	$F \propto \phi_{ice}$	Finney et al. (2014)
Hybrid approach	Collision rate between ice particles (Q_R), Boundary layer depth (Z_B)	$F \propto f(Q_,CAPE, Z_B)$	Lopez (2016)
	Normalized CAPE (NCAPE), near-surface cloud condensation nuclei (CCN), warm cloud depth (WCD), 850-500 hPa average relative humidity (RH), 1000-500 hPa vertical wind shear (SHEAR)	$F \propto f(NCAPE, CCN, WCD, RH, SHEAR)$	Stolz et al. (2017)

2.3 Remaining challenges

Many lightning parameterization schemes are developed over the past few decades following the advance in lightning observations and numerical models. However, still many challenges remain in the lightning parameterization schemes that are currently being used in numerical models. In particular, the forecast of lightning remains largely uncertain in the numerical models. Given the known impacts of lightning summarized in Chapter 1, it is critically important for NWP and ESM models to accurately represent lightning to reduce lightning-induced hazards and to yield reliable future climate projections. Unfortunately, however, the lightning forecast and the future projection of lightning frequency remains largely uncertain (Clark et al., 2017; Finney et al., 2014; Romps, 2019).

On a shorter time scale, despite the sophisticated NWP models employed, thunderstorms remain relatively unpredictable on a daily time scale (Clark et al., 2009). As summarized in Chapter 2.2, most lightning parameterization methods rely on the atmospheric variables outputted from NWP models. An accurate lightning forecast rely on the simulated deep convective systems, which are a prerequisite for the generation of lightning. Thunderstorm prediction is therefore often hampered by the poor predictability of deep convective clouds (Walser et al., 2004). The rapid growth of error in the simulation can lead to large uncertainties in the location, timing and intensity of the deep convective systems. On the other hand, the lightning forecast also relies heavily on the lightning parameterization methods in the NWP models. The uncertainties introduced from the lightning parameterization methods and its relative importance compared to the simulated convective systems remains relatively unexplored.

On a longer time scale, Clark et al. (2017) showed that the future projection of the global mean lightning flash density are highly sensitive to the lightning parameterization method chosen. In their study, a set of numerical simulations are performed using a GCM. The simulations consist of three parts: a reanalysis simulation and two fully coupled historical and future scenario simulations. The reanalysis simulations are run by nudging atmospheric

fields toward ERA-Interim reanalysis data during the 13 years period (1996-2008), where the simulated lightning can be compared with the observations that are available from satellites. The historical and future simulations are based on two greenhouse gas emission scenarios, namely, RCPs 4.5 and 8.5 (Thomson et al., 2011; Riahi et al., 2011).

Clark et al. (2017) tested eight different lightning schemes in their simulations. These lightning schemes include five size-based methods that are based purely on cloud-top height (Price and Rind, 1992; Boccippio, 2002; Michalon et al., 1999; Yoshida et al., 2009), a modified size-based methods that takes into account the cloud droplet number concentration (Michalon et al., 1999), and two convection-based methods that are based on convective precipitation and convective mass flux (Allen and Pickering, 2002). The time average of the lightning flash density (LFD) distribution from observations and each of these simulations during the 13 year period 1996–2008 are shown in Figure 2.1.

By normalizing the simulated global LFD by that during the reanalysis period, the trend of global LFD is shown in Figure 2.2. The simulations made with size-based lightning parameterization methods have a near linear response with respect to changes in global surface temperature. However, simulations using convection-based methods give a weaker positive or a negative trend, suggesting that the simulated response is highly dependent on the type of lightning parameterizations. Their results therefore suggest that the uncertainty in the lightning parameterization schemes is a key source of the uncertainty in the future projection of the global LFD. The diverse representation of lightning in ESMs (see Table 2.1) also reflects the lack of understanding of the physical processes that governs the number of lightning flashes on the spatial scale of ESMs' grid size.

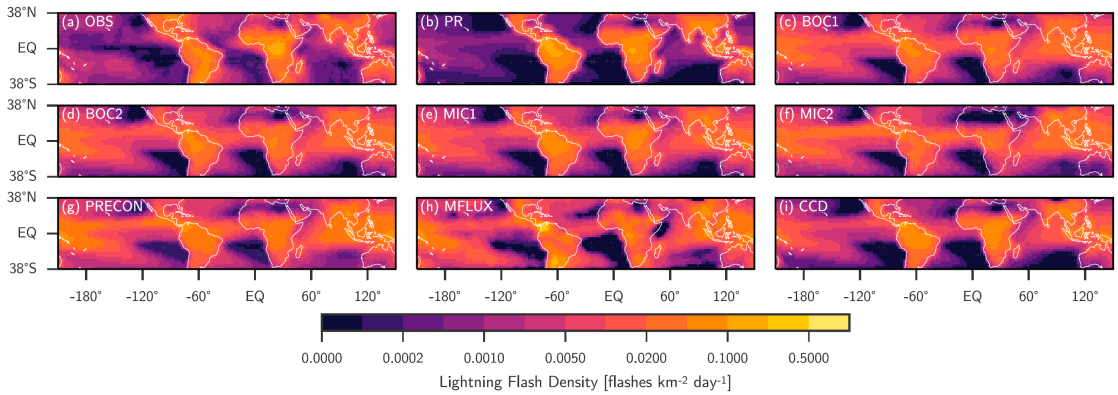

Figure 2.1: Time average (a) LIS/OTD satellite product and (b–i) simulated LFD in the ERA experiment (nudged to match reanalysis meteorology) for the 13 year period 1996–2008.. Figure adapted from Clark et al. (2017).

The uncertainty in the lightning parameterization schemes is largely due to the lack of understanding of lightning mechanisms. Most lightning parameterization methods are derived empirically from correlations between other convection-related quantities based on limited knowledge and observations. However, their applicability to the global scale for a long-term time period is not yet well established due to the limited lightning observations. In the next Chapter, I will discuss the recent development of lightning observations, as well as the recent development of machine learning techniques, which allow us to improve our understanding of lightning mechanisms and the representation of lightning in numerical models using a data-driven approach.

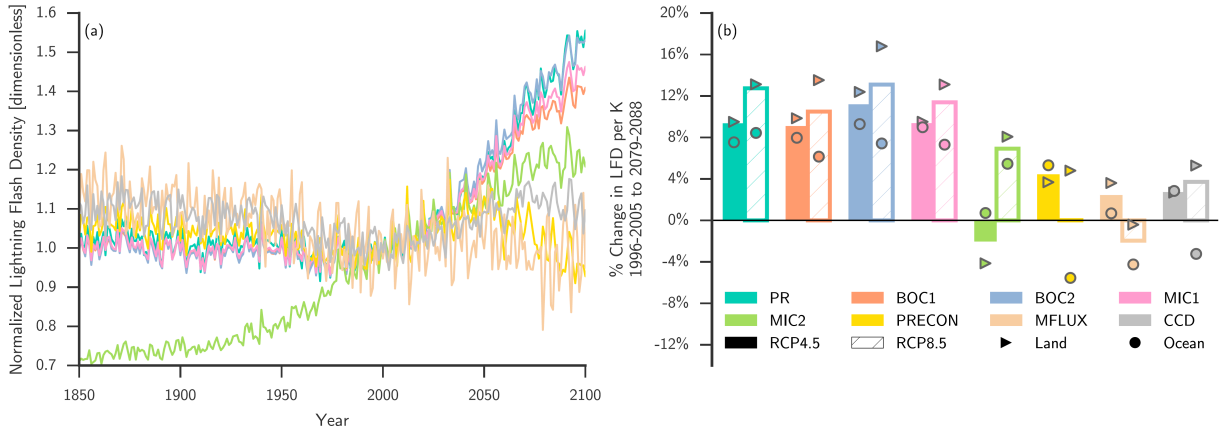

Figure 2.2: (a) Time series of normalized annual global mean LFD in the RCP8.5 simulation for each parameterization tested. The LFDs of the parameterizations are normalized such that the time mean LFD between 1996 and 2011 is one. (b) Percent change in LFD per degree warming from 1996–2005 to 2079–2088 in the RCP4.5 case (solid bars) and RCP8.5 case (hatched bars). The triangle and circle symbols indicate the percent change of area average LFD per K global warming from 1996–2005 to 2079–2088 over land and ocean, respectively. Figure adapted from Clark et al. (2017).

Chapter 3

ADVANCES IN LIGHTNING OBSERVATIONS AND MACHINE LEARNING

3.1 Advances in lightning observations

The earliest systematic lightning detection network can be dated back to the development of automatic multisensor lightning locating systems (LLSs) in 1920s (Cummins and Murphy, 2009). At that time, the lightning detection is based on the radio atmospheric signal (i.e., sferics). Measurements of electromagnetic fields produced by lightning were typically obtained using radio receivers in the very low frequency (VLF; 3–30 kHz) and low frequency (LF; 30-300 kHz) range. Before the development of weather radars, thunderstorms are tracked primarily using narrow-band VLF "sferics" detection systems consisting of two or more spatially separated receivers. This type of detection method can locate thunderstorms with location accuracy of several tens of kilometers, which was a broadly utilized tool during World War II (Norinder, 1953).

In the late 1950s, time-of-arrival (TOA) geolocation techniques were first employed for the purpose of lightning detection (Lewis et al., 1960). The core concept of this technique is that while the difference in the arrival time at two stations defines a hyperbola, the source location of the lightning can be identified by using the intersections of multiple hyperbolas provided by multiple stations. A major challenge for the early TOA systems was the need for precise time synchronization of multiple remote sensors. In the 1980s, the National Lightning Detection Network (NLDN; Orville, 2008) is established, by employing the TOA sensors installed throughout the CONUS, with the average distance between sensors of approximately 300–400 km. The NLDN system located lightning in the interior of the network of TOA measuring, which enables the location accuracy to be within the range of < 1 km

using information from more than three sensors. By the time of 2010s, there are more than 60 ground-based LLSs networks worldwide that utilize the TOA technique operating in the VLF/LF range. Examples of large networks include the European Cooperation for Lightning Detection (EUCLID; Schulz et al., 2016; Poelman et al., 2016), the Lightning Detection Network (LINET; Betz et al., 2009), the Japan Lightning Detection Network (JLDN; Sugita and Matsui, 2012), the Brazilian National Network (BrasilDAT; Naccarato and Pinto Jr, 2009), and the Canadian Lightning Detection Network (CLDN; Burrows et al., 2002).

While the ground-based LLSs provide consistent lightning observations, most of these LLSs are operating on a regional basis and are unable to provide lightning observations globally. The space-based approaches were first developed to provide near-global lightning observations. In 1995, National Aeronautics and Space Administration (NASA) launched the Optical Transient Detector (OTD), which is a scientific payload on the MicroLab-1 satellite, covering a near-global domain from 75°S to 75°N. Two years later, the Tropical Rainfall Measuring Mission (TRMM) satellite was launched with the Lightning Imaging Sensor (LIS) onboard, which made observations of lightning flashes over a wide tropics between 35°S and 35°N. OTD and LIS combined have provided over a decade (1995 - 2010) of high-quality lightning observations. The sensors on both OTD and LIS monitor the 777.4 nm atomic oxygen multiplet, detecting pulses of illumination produced by lightning. Both satellites were operating in low earth orbit, viewing an earth location for a short period of time (3 minutes for OTD and 90 seconds for LIS) when satellites passed overhead. While the satellites serve as excellent tools for lightning observations that covers a wide range in time and space, their scanning strategy prevent them from observing any region continuously in time, which limits their usage. For some region, the total scanning time is only 60 hours in total during the period of 1995 – 2010 (Cecil et al., 2014), which is considered short for a relatively infrequent phenomenon such as lightning. Thus, continuous high-quality observations of lightning on a global scale remain an challenge even in early 2010s (Cummins and Murphy, 2009).

Over the past decades, the ground-based lightning detection networks have been developed rapidly throughout the world to catch up the spatial coverage of satellite observations.

In particular, the World Wide Lightning Location Network (WWLLN; Rodger et al., 2006) is developed, which utilizes a time-of-group-arrival (TOGA) method in VLF band to locate lightning strikes. The TOGA is determined relative to GPS at each site from the progression of phase versus frequency using the whole wave train. The stable propagation and low attenuation of VLF waves in the Earth–ionosphere waveguide (EIWG) allows a wide spacing of receiver sites of several thousand kilometers, so that a global lightning detection could be provided using as little as ∼10 receiver sites (as of the time of writing, WWLLN consists of more than 70 sensors worldwide). The detection efficiency of WWLLN is approximately 70% for all strokes with peak current greater than 40 [kA] (Holzworth et al., 2019), with location errors less than 10 km based on comparisons with observations from NLDN and CLDN (Abreu et al., 2010; Abarca et al., 2010). Over the CONUS area, it is found that the performance of WWLLN is comparable to NLDN as the spatial correlation of lightning flashes between the WWWLN and the NLDN is as high as 0.75 in 2008–2009 (Abarca et al., 2010). The rich global lightning observation data provided by WWLLN provide a new opportunity to further our understanding of lightning mechanisms, and to help improve the lightning representation in numerical models.

3.2 Advances in machine learning techniques

Together with the lack of understanding in the physical mechanisms of lightning, another major challenge of representing lightning in numerical models lies in the parameterization process. Since numerical models cannot fully resolve the physical processes of lightning generation, the unresolved sub-grid scale processes therefore have to be represented using the resolved variables by building relationships between the sub-grid scale processes and the resolved quantities: parameterization. However, the best way to simulate lightning based on model-resolvable variables is not clear (Clark et al., 2017).

One possible pathway for progress on this issue is through data-driven approaches, specifically the machine learning (ML), a subset of the artificial intelligence (AI). Simply speaking, the ML techniques train an algorithm to extract desired patterns from the data, which then

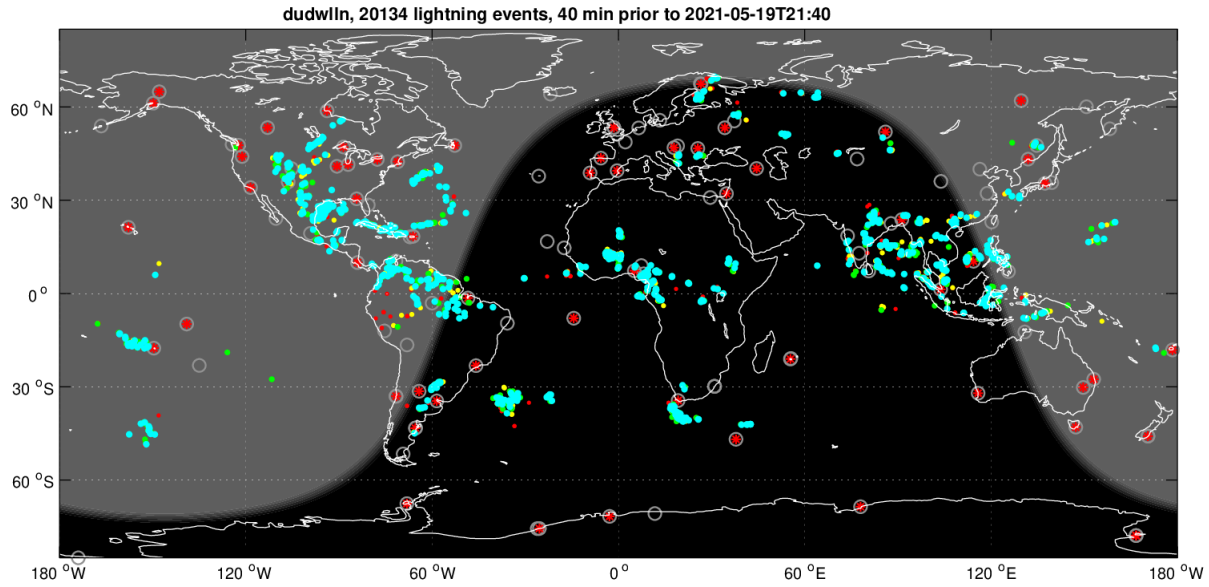

Figure 3.1: An example showing the lightning stroke detected by WWLLN. Lightning stroke positions are shown as coloured dots, where the colors indicate the time of detection, from the last 10 min (blue), 10 - 20 min (green), 20 - 30 min (yellow), to 30 - 40 min (red). Red asterisks in white circles are active WWLLN lightning sensor locations. The terminator (day-night boundary) is shown, with the daylit section of the globe in grey. Figure adapted from http://wwlln.net/.

can be used for the prediction with unseen data samples.

In the case of the supervised learning, a set of labeled datasets that contain input-output pairs will be provided (the training data), and the ML model will learn the patterns within the dataset through the "training" process: as the input data is fed into the model, the model will find the algorithm to best fit the data by minimizing a human-defined cost function, which is usually a measure of the difference between the true labels and the predicted labels, until the model has been fitted appropriately. The trained ML model will then be applied to make a prediction for unseen data samples (the testing data), assuming that the training and testing data are independent and identically distributed.

The application of ML techniques to various aspects of weather/climate forecasting is drawing increasing attention and yielding promising results. One of the most popular use cases of ML in meteorology has focused on the improvement of physics parameterizations in numerical models. Most current parameterization schemes in numerical models are based on our physical knowledge. While this makes the parameterization schemes potentially more efficient and human-interpretable, it may also lead to oversimplifications that exert a limitation to the model performance. In contrast to conventional parameterizations, an ML-based parameterization is more "flexible" because they have numerous free parameters that can be trained to minimize the error, instead of relying on a few mathematical formulas. For example, Rasp and Lerch (2018) developed a neural-network-based cloud parameterization for a low-resolution GCM, where the ML model is trained by feeding in the outputs from a high-resolution cloud-resolving version of the model. They show that the NN parameterization is capable of emulating the high-resolution model with much lower computational expense. Likewise, other ML-based parameterization applications also showed promising results, including radiative transfer (Belochitski et al., 2011), atmospheric chemistry (Mallet et al., 2009), and subgrid turbulence modeling (Ling et al., 2016; Wang et al., 2017).

Another branch of use cases of ML in meteorology focuses on the prediction of weather and climate. In this type of applications, the ML models are usually trained purely from past weather observations without explicitly specifying the physical processes, and let the

ML models "learn" the physics by extracting the behaviors from the rich datasets. The idea behind this type of application is to bypass the complex dynamics and physics modules in the numerical models and instead build a data-driven algorithm to predict the weather/climate directly using ML. This is often a computationally challenging task because the physical processes are often extremely complex and highly nonlinear: to let the ML models fully capture the behavior of the weather and climate systems, it often requires a large training sample size and a lot of computational resources to achieve a high performance.

Over the past decade, the rapid growth of reliable weather data from observations and models and the efficient computing from graphics processing units (GPUs) have accelerated the advance of the ML-based forecasting. For example, Ham et al. (2019) used a neural-network-based ML model to predict the evolution of the El Niño Southern Oscillation (ENSO). In their ML model, the input variables include the sea surface temperature (SST) and oceanic heat content (HC) in the past, and the output is the future Niño 3.4 index. To increase the limited amount of training samples from observations, they utilize an ensemble of GCM simulations of the historical period together with the reanalysis data by using the transfer learning techniques. Their results show that neural-network-based ML model is capable of predicting the types of El Niño events 12 months in advance, and has a higher correlation skill of Niño 3.4 index for all-season compared to traditional dynamical forecast systems.

Weyn et al. (2019) predicted the geopotential height at 500 hPa and 700-300 hPa thickness at 6 hourly time steps using a neural-network-based ML model. In their study, the ML model is trained using the the Climate Forecast System (CFS) Reanalysis product with 6-hourly time resolution over Northern Hemisphere in the period from 1979 to 2007. The trained model easily outperformed the dry barotropic vorticity model, while performed worse than an operational NWP model. In Weyn et al. (2020), the authors expand the domain of the ML model by mapping the atmospheric variables to cubed sphere, which allows the ML model to be trained over the global domain without encountering the issues with the boundary conditions near the edge of the domain. The revised model showed significant improvement

over its predecessor in terms of the stability of the model and maintaining the forecast skill over a longer forecast lead time. While the ML model is still not able to outperform the operational weather forecasting models, the ML model based on data-driven approach has a clear advantage as it requires much less computational resources, suggesting that there are potential room for improvement either by increase the number of atmospheric variables as input or by utilizing large-ensemble forecasting.

The recent development of ML approaches allow us to fully capitalize on the rich global lightning observation data provided by WWLLN. In particular, there is a huge potential of using ML techniques to help improving the lightning parameterization in the numerical models and to further achieve a better lightning forecasting.

3.3 Progressing lightning parameterization and lightning forecasting

the recent progress on the lightning observations and ML techniques have allowed us to explore some of the unsolved challenges in the lightning parameterization problems. For example, while R14 method has proven successful over CONUS (Romps et al., 2018; Tippett and Koshak, 2018), its performance drops significantly when applied globally, Specifically, it is found that R14 method produces too frequent lightning over the tropical ocean basins (Gordillo-Vázquez et al., 2019; Romps et al., 2018). Romps et al. (2018) concluded that the CAPE differences between land and ocean alone are not enough to explain the land-sea differences in f, and other mechanisms may be important in controlling f. Several mechanisms have been proposed to explain the land-sea differences in f, some of which points to the effects of storm size on the updraft intensity (see discussion in Chapter 4.1). However, the observational evidence is still lacking, largely due to the lack of consistent and reliable global lightning observations.

With the development of WWLLN and ML techniques, this dissertation is aimed to improve the understanding of lightning mechanisms and to improve the representation of lightning in the numerical model. More specifically, I will address three key questions in this dissertation: (1) *How does the size of convection affect the lightning frequency, and how does*

it affect the land-sea lightning frequency contrast? (2) *Can we improve the representation of lightning using grid-scale variables available from reanalysis data?* (3) *Can we extend the prediction skills of lightning by utilizing machine-learning based lightning parameterization methods?*

I will address the first question by combining WWLLN data with satellite observations to examine the relationship between f, storm size, and other atmospheric variables in Chapter 4. With the amount of observations that are available from WWLLN and satellites, I will be able to examine the previously proposed hypothesis on the land-sea f contrast using observations. At the end of the Chapter, I will demonstrate that the results can help improve the understanding of the physical mechanisms of lightning and improve the representation of lightning of the CAPE-based lightning parameterization methods in the numerical model.

The second the third questions will be addressed in Section 5, where I will implement the ML-based lightning parameterization methods by using grid-scale variables available from reanalysis data. Several ML methods are tested, including the random forest model and neural network model, where the models are applied to predictions of f. By using 10 years of data, our results show that, even with the same input variables, the ML-based lightning parameterization methods are able to outperform an empirical lightning parameterization method in terms of capturing the spatial/temporal variability of lightning. I will also show that the ML methods can help improve the forecast skills of f in the NWP models.

Chapter 4

CAPE THRESHOLD FOR LIGHTNING OVER THE TROPICAL OCEAN

4.1 Land-Sea lightning frequency contrast

From an analysis of station thunder days, Brooks (1925) first proposed that the global lightning distribution exhibits a 5- to 10-fold land-sea contrast on a global basis. It was later confirmed from the optical observations of lightning from the Defense Meteorological Satellite Program (DMSP) satellite, which revealed an order of magnitude contrast in total lightning occurrence between land and ocean (Orville and Henderson, 1986). Recent observations from the Optical Transient Detector (OTD) and Lightning Imaging Sensor (LIS) from the Tropical Rainfall Measuring Mission (TRMM) satellite again confirmed such a contrast in lightning activity (Christian et al., 2003). It is noted that the land sea lightning frequency contrast is likely sensitive to the instruments. Virts et al. (2013) documented that the land and ocean lightning contrast observed by World Wide Lightning Location Network (WWLLN; see http://wwlln.net) is much smaller than that from satellite observations. Nevertheless, both instruments suggest that the lightning frequency over land is significantly higher than that over ocean.

When attempting to parameterize the global lightning frequency in the ESMs, various approaches have encountered difficult times representing the land-sea lightning contrast. For example, in PR92, where the total lightning flash rates (F) is estimated using cloud-top height, their simple formulas cannot capture the land-sea lightning contrast and they have to adjust their formulas over land and ocean separately, which violates V63's theory and is demonstrated to be inconsistent with observations (Boccippio, 2002). In R14, F is estimated using the product of CAPE and precipitation (P). While it is shown that CAPE x P method

can successfully represent the lightning climatology and seasonal variation over the CONUS, it failed to explain the land-sea contrast (Romps et al., 2018). In the ice-flux-based method proposed by Finney et al. (2014), it is shown that the F and ϕ_{ice} exhibits a linear relationship with the correlation coefficient of 0.63 over land. However, the correlation drops significantly over ocean to 0.25.

Several theories have been proposed to explain the land-sea lightning contrast, which are missing in the existing parameterization methods (Williams and Stanfill, 2002). These theories include:

4.1.1 a. Aerosol effects

The higher aerosol concentration over land leads to more invigorated convection (Koren et al., 2005). This causes the convective cores to be elevated over land, resulting in higher lightning flash rates (Stolz et al., 2015, 2017; Thornton et al., 2017). However, the impact of aerosols effect has been questioned by Williams and Stanfill (2002) by showing the lack of lightning frequency changes between aerosol-rich October and aerosol-poor November in the Amazon region.

b. Entrainment effect

The drier environment over land leads to a deeper subcloud mixed layer, which causes the convective updrafts over land wider at birth, and more protected from the effects of convective environment (Lucas et al., 1994; Williams and Stanfill, 2002). Consequently, under the same environmental condition, the charge transfer speed is faster over land due to the smaller entrainment rate and the stronger convective updrafts (Bang and Zipser, 2016).

In a recent study, Lopez (2016) attempted to incorporate the entrainment effect into the lightning parameterization method. In their study, the cloud-base height (Z_B) is used as a proxy for the horizontal extent of the convective ascent, which is assumed here to increase with Z_B. However, there is still a lack of observational evidence on the relationship between

cloud-base height and lightning activities, which is partially due to the lack of consistent and reliable lightning observations.

While studies have hinted at that CAPE and storm size may be key factors for lightning generation and is important for land-sea lightning frequency contrast, a thorough examination of the relationship between CAPE, f and storm size has not yet been performed, which is largely limited by the insufficient global lightning observations. The newly developed ground-based lightning observations from WWLLN provides an unique opportunity to further our understanding of lightning mechanisms. By taking advantage of the rich WWLLN dataset, in this Chapter I aim to investigate the relationship between CAPE, storm size, and f over the Central America region.

4.2 Data and methods

4.2.1 Data

Brief descriptions of the datasets used in this study are given in Table 4.1. All data are obtained for 2012-2015. The lightning flash density is obtained from WWLLN (http://wwlln.net/), a ground-based network of more than 70 sensors around the globe that detect electromagnetic radiation (i.e., sferics) emitted by lightning strikes at very low frequency (3–30 kHz). The WWLLN preferentially detects cloud-to-ground lightning and detects generally one or two strokes within a lightning flash (Abarca et al., 2010; Abreu et al., 2010). A later study from Rudlosky and Shea (2013) found that the multiplicity (number of WWLLN strokes per flash) was close to 1.5 during the period between 2009 and 2012 over the western hemisphere. Following previous studies on the comparison between WWLLN and Lightning Imaging Sensor (Bürgesser, 2017), we will match WWLLN strokes to flashes directly and the lightning stroke density will also be denoted as f in this study.

Table 4.1: A brief description of the dataset used in this Chapter

Variable	Dataset	Horizontal resolution	Data frequency	Domain	Availability
Lightning flash density (f)	WWLLN	10 km	Hourly	Global	2004-present
Convective available potential energy (CAPE)	ERA5	0.25°	Hourly	Global	1950-present
Precipitation (P)	TRMM 3B42	0.25°	3-hourly	35°S - 35°N	1998 - 2019
Brightness temperature (T_B)	GridSat-GEOS	4 km	3-hourly	75°S - 75°N 150°E - 5 °W	20

The detection efficiency of WWLLN is approximately 70% for all strokes with peak current greater than 40 [kA] (Holzworth et al., 2019), with location errors less than 10 km based on comparisons with observations from the short-range lightning observation networks in North America (Abarca et al., 2010; Abreu et al., 2010). The rain rate is taken from the Tropical Rainfall Measuring Mission (TRMM) Multi-satellite Precipitation Analysis (TMPA). The TRMM dataset used in this study is the post-real-time data of version 7 (3B42), with a temporal resolution of 3 hours and spatial resolution of $0.25^{\circ}\times 0.25^{\circ}$(Huffman et al., 2007). CAPE values are obtained from ECMWF Reanalysis 5th Generation (ERA5; Hersbach et al., 2020), a reanalysis dataset providing the best estimate of the atmospheric state variables. The CAPE values are diagnosed in ERA5 using the vertical integration of thermal buoyancy (B). The integration starts at the Level of Free Convection (LFC) and continues until the Equilibrium Level (EL), in which the parcel loses its buoyancy. The mathematical formula can be expressed as (Markowski and Richardson, 2011):

$$CAPE = \int_{LFC}^{EL} B dz \tag{4.1}$$

where

$$B \approx \frac{T_{v,parcel} - T_{v,environment}}{T_{v,environment}} \tag{4.2}$$

In the above equation, the thermal buoyancy is purely due to density differences between the rising air parcel and the environment, where where $T_{v,parcel}$ and $T_{v,environment}$ are the virtual temperature of the parcel and the environment, respectively. For computational efficiency, the calculation of CAPE in ERA5 is approximated to:

$$CAPE = \int_{z_{dep}}^{z_{top}} g(\frac{\theta_{ep} - \bar{\theta}_{esat}}{\bar{\theta}_{esat}}) dz, \tag{4.3}$$

where z_{dep} is the parcel departing level, z_{top} is the neutral buoyancy level, g is the constant of gravity, and θ_{ep} and θ_{esat} denote the equivalent potential temperatures of the par-

cel and the saturated equivalent potential temperature of the environment, respectively (Groenemeijer et al., 2019). Multiple departing levels are tested and only the maximum CAPE yielded is retained. The entrainment and water loading effect are not considered. Because w_{max} is more closely related to CAPE$^{1/2}$ as discussed in Chapter 2.2, we will use CAPE$^{1/2}$ instead of CAPE in the following.

The brightness temperature (T_b) is obtained from the GridSat-GOES data developed at NOAA's National Climatic Data Center (Knapp and Wilkins, 2018). The GridSat data are calibrated in equal angle map projection for different satellite projects. We use the IR band (10.7μm Channel 4) product, which provides the cloud-top or surface temperature observations with a spatial resolution of 4 km and temporal resolution of 3 hours that cover from 75°N to 75°S and from 150°E to 5°W.

The relationship among lightning flash rate, rain rate, CAPE, and the number and size of convective elements is analyzed over the Central America region (0°N – 20°N, 60°W – 105°W, Figure 4.1). In this region, the WWLLN dataset has the highest lightning detection efficiency due to the densely populated stations (Hutchins et al., 2012). The analysis is performed in the 72 3°× 3°boxes (45 white ocean boxes + 27 black land boxes) indicated in Figure 4.1. It is noted that many of these boxes could be considered as coastal regions, where the sharpest transition in the frequency and energy of lightning strokes has been observed, while the underlying physical mechanisms remain poorly understood (Hutchins et al., 2013).

4.2.2 Identification of contiguous convective objects and convective overshooting tops

In each 3°x 3°box, we first identify the convective pixels whose T_b is less than 210 [K] and then group them into contiguous convective objects (CCOs) following the 4 connectivity rules, i.e., two convective pixels belong to the same CCO if they share a common side (Tobin et al., 2012, 2013). The sensitivity test results suggest that the statistics of the number of CCOs is insensitive to the T_b threshold used to identify the convective pixels within the range of 210 [K] to 240 [K] (not shown). To prevent the statistics from being contaminated by the small CCOs near the edge of convective systems, the CCOs with less than 10 convective

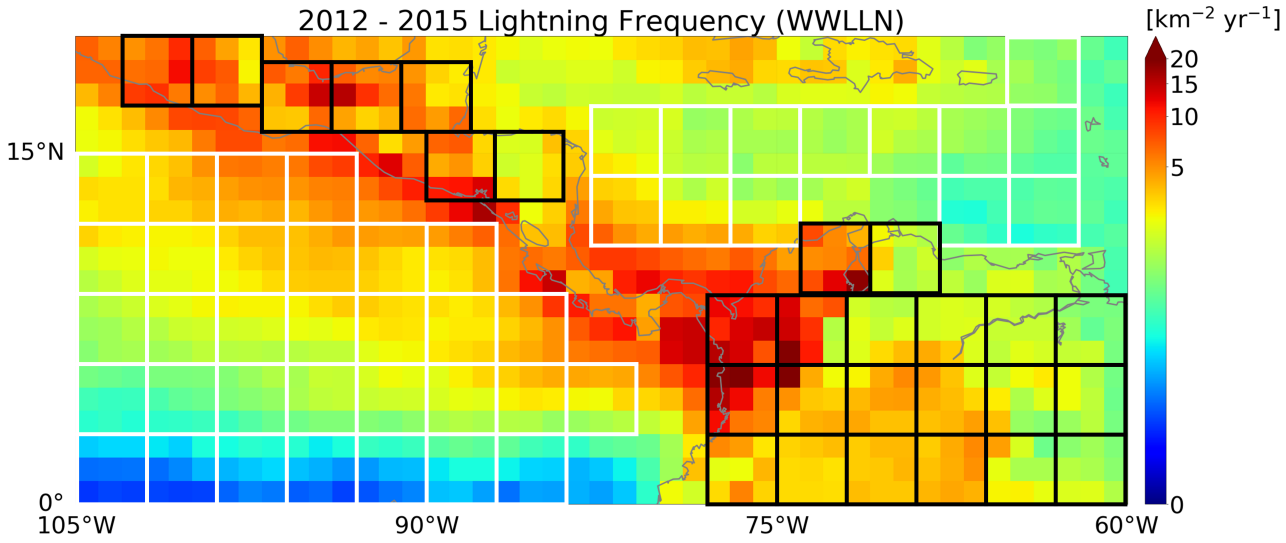

Figure 4.1: The annual mean lightning flash density [km^{-2} yr^{-1}] from WWLLN. The white/black 3°by 3°boxes indicate the ocean/land domains used in the analysis.

pixels are disregarded. Increasing the minimum number of convective pixels required would decrease the number of CCOs and increase the mean CCO size, but changing the minimum number within the range of 1 to 20 does not affect our conclusions.

While one can infer the number and size of convective storms within a domain by inspecting characteristics of CCOs, the presence of a CCO does not guarantee that it hosts active updrafts. A decaying convective system that largely consists of anvil clouds without active updrafts, for example, can be detected as a CCO. Therefore, as a more direct proxy for deep and active updrafts, we identify overshooting tops (OTs). The strong upward momentum of convective updrafts often causes the rising air to protrude above its equilibrium level near the tropopause and penetrates into the lower stratosphere, forming a domelike feature above a cumulonimbus anvil named OTs. Identification of OTs in satellite imagery has long been used in methods of severe weather detection. In a modeling study, Trapp et al. (2017) showed that there exists a robust correlation between midlevel updraft area and the horizontal area of its associated overshooting top area, identified as contiguous areas of cloud top temperatures colder than 5 [K] minus the tropopause temperature (Figure 4.2). Their results show that the size of OTs could be used as a proxy for updraft width.

In this study, the method of OT identification follows that of Bedka and Khlopenkov (2016) and Marion et al. (2019), which are based on the gradients of T_b. An hypothetical T_B field is provided in Figure 4.3 to illustrate the two-step detection method. Specifically, the algorithm first looks for the local minimum in the T_b field, and then searches for the edges of the OT in eight directions by finding the inflection points in Tb field. Beginning at the location of the minimum T_b ($T_{b,min}$), a scalar array of Tb values is assembled along the eight radials extending from this point. The 1-D second derivative along the radial ($\frac{d^2T_b}{dr^2}$) is then calculated using a simple finite difference approximation. The edge of the OT along each radial is defined as the first point where ($\frac{d^2T_b}{dr^2}$) ≤ 0. The area of each OT is then calculated assuming the OT is circular in shape: $OTA = \pi r_m^2$, where r_m is the mean radial. An example of the identified CCOs and OTs in a snapshot is given in Figure 4.3.

In this study, for each 3-hourly snapshot, the morphology of the convective systems

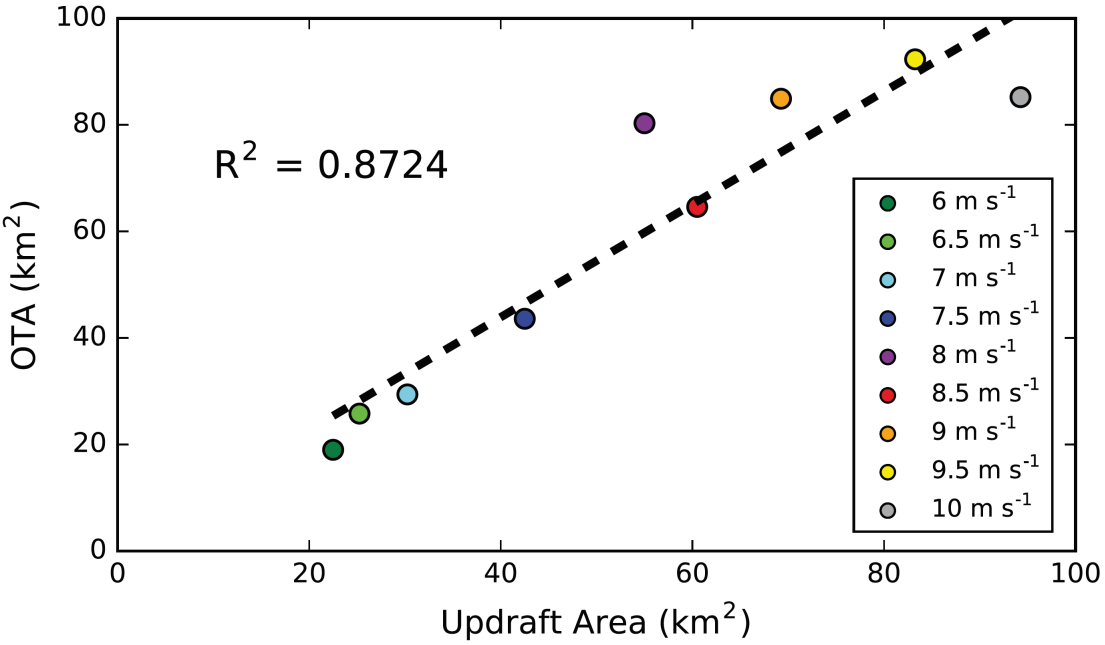

Figure 4.2: A scatterplot showing the relationship between peak overshooting-top area (km^2) and peak midlevel (z = 6.25 km) updraft area (km^2). The different colors indicate the hodograph radii assigned in the experiments. Figure adapted from Trapp et al. (2017).

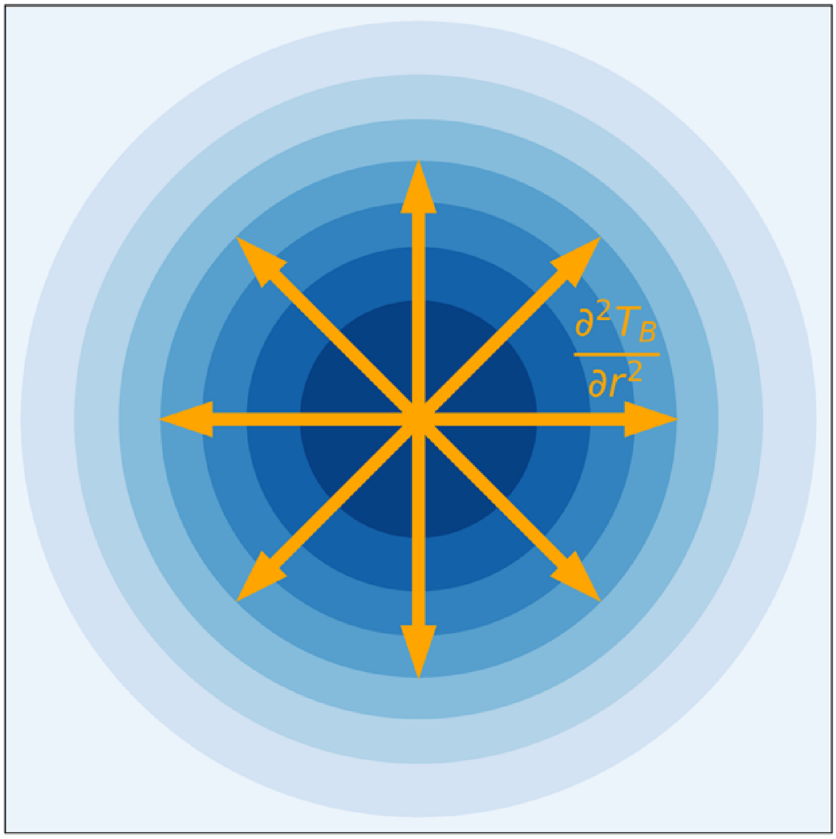

Figure 4.3: Brightness temperature (T_B) field associated with a hypothetical overshooting top. Darker shading indicates relatively lower T_B. The orange arrows depict the eight radials along which the 1-D Laplacian of T_B is computed. The overshooting top edge is equated with the point along the radial where the 1-D Laplacian first becomes 0. Figure adapted from Marion et al. (2019).

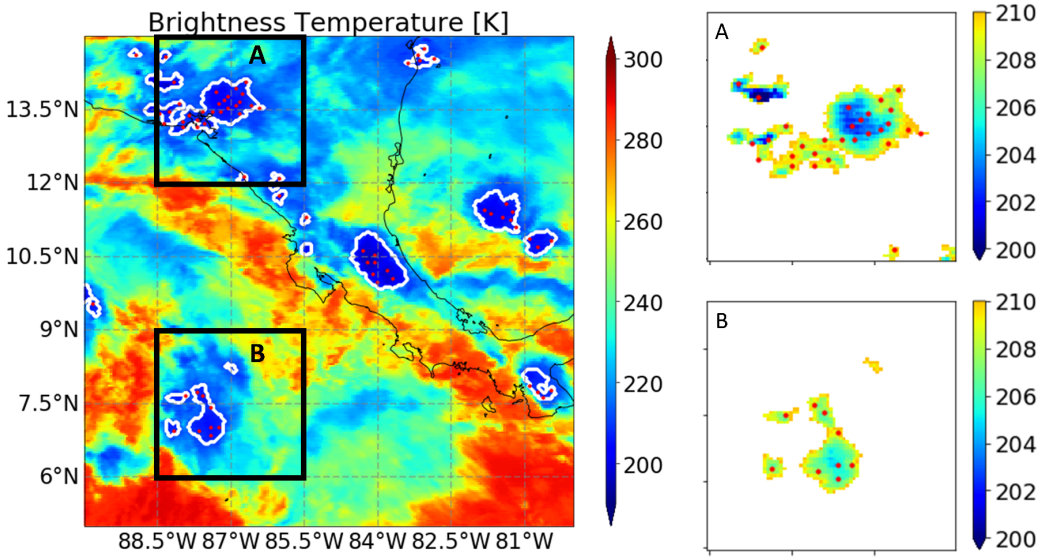

Figure 4.4: An example snapshot of brightness temperature (T_b [K], shaded) field at 2014-06-16T00:00:00 with the identified Contiguous Convective Objects (CCOs) and Overshooting Tops (OTs). On the left panel, the white contours indicate the CCOs, and the red dots indicate the centers of OTs embedded within CCOs. The panels on the right show the zoom-in view on two regions indicated as black squares on the left panel. In the zoom-in view, the shadings show only the Tb inside of CCOs, and the red dots indicate the centers of OTs embedded within CCOs.

within each 3°× 3°grid box (Figure 4.1) will be characterized using the identified CCOs and OTs. The number of convective storms will be quantified by counting the number of CCOs (N_{CCO}), while the horizontal size of individual storms will be quantified by averaging the areas of all CCOs within the grid (A_{CCO}). The use of A_{CCO} as a proxy for the size of active convection will be augmented by computing the total area of OTs for each CCO and then averaging those over all CCOs within each domain (OTA_{CCO}). Figure 4.5 shows that A_{CCO} and OTA_{CCO} are positively correlated with each other over both land and ocean. It is worth noting, however, that for given A_{CCO}, convective storms over land tend to have a greater OTA_{CCO}, likely because the CCOs over ocean contain a higher fraction of high anvil clouds or thick cirrus, due to the greater moisture supply from the environment.

4.3 Role of storm size on the CAPE-f relationship: regional analysis over Central America

Figure 4.6 shows f as a function of CAPE$^{1/2}$ and precipitation (P) in the 45 ocean (Figure 4.6a) and 27 land (Figure 4.6b) grids over the Central America region (Figure 4.1). Overall, f increases with increasing CAPE$^{1/2}$ and P over both land and the ocean, indicating their predictive potential for f. An interesting feature in Figures 4.6a and 4.6b is that f is much lower over the ocean than over land when CAPE is low (Figure 4.6c), especially when CAPE$^{1/2}$ is smaller than about 25 [m s^{-1}]. To examine the cause of the stark land-sea f contrast in the low-CAPE regime, we partition f into lightning probability ($Prob$) and lightning intensity (Int) such that $f = Prob \times Int$. The results show that both factors have contributions to the suppressed f over the ocean in the low-CAPE regime. In the low-CAPE environment, oceanic storms have a lower probability to generate lightning (Figure 4.6d - 4.6f) and when the storms do generate lightning flashes, the number density of lightning is also lower (Figure 4.6g – 4.6i).

As a result of f being suppressed over the ocean in the low-CAPE regime, the CAPE-f relationship shows a notable land-sea contrast, where f is larger over land when CAPE$^{1/2}$ is lower than 25 [m s^{-1}] (Figure 4.7). Over land, f increases almost linearly with increasing

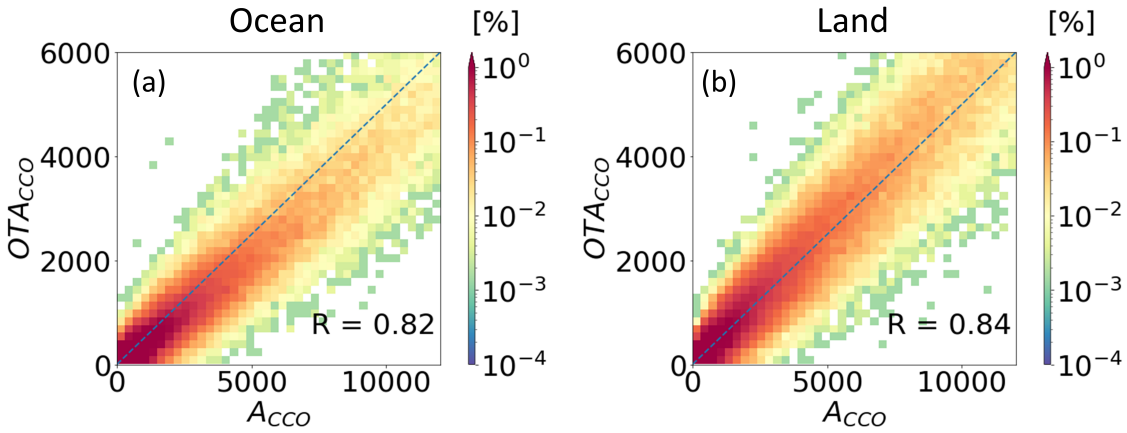

Figure 4.5: Joint probability density of A_{CCO} and OTA_{CCO} over (a) ocean and (b) land. The dashed reference line shows the constant 2:1 line.

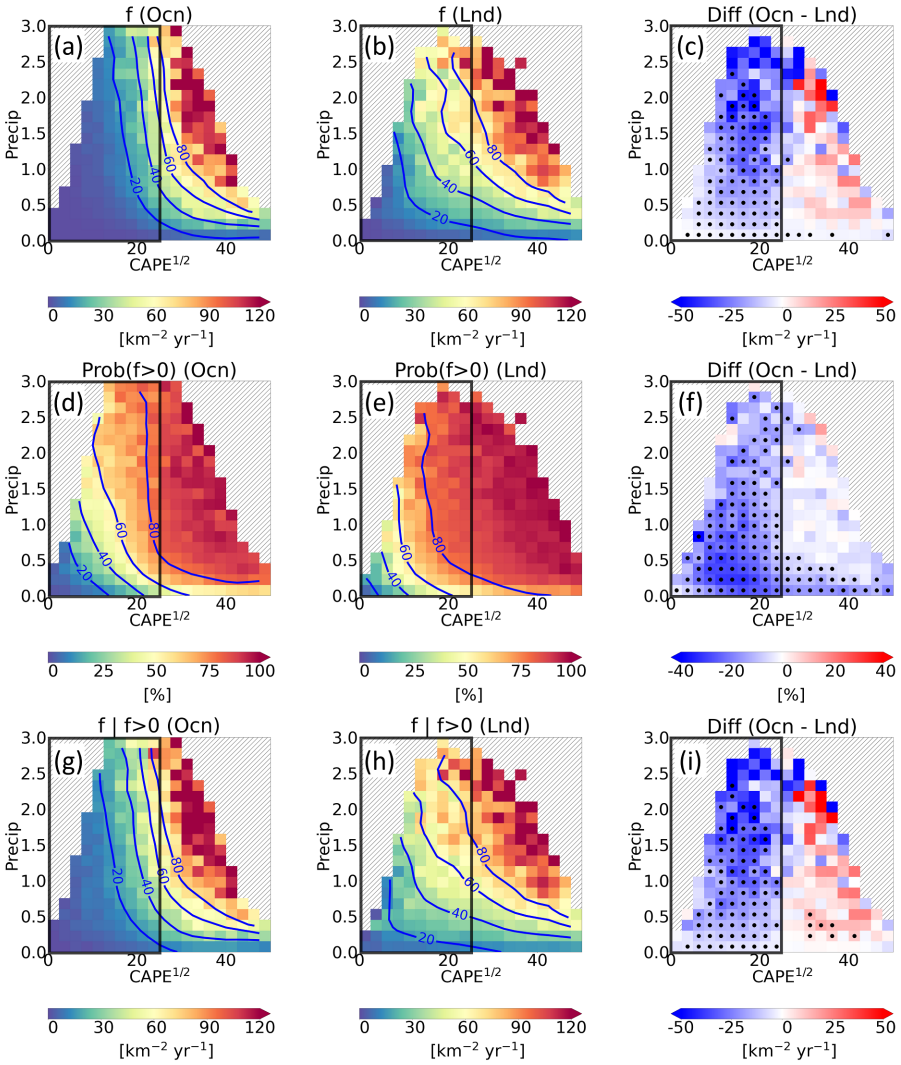

Figure 4.6: The shadings show the composite (a - c) lightning flash density [km^{-2} yr^{-1}], (d - f) probability of lightning [%], and (g - i) lightning intensity [km^{-2} yr^{-1}] in different bins of $CAPE^{1/2}$ [J kg^{-1}] and precipitation [mm $3hr^{-1}$], respectively. The contours are the same as the shadings, except that a Gaussian smoothing is applied to better illustrate the trends. The composites are made over the ocean (left column) and land (middle column) separately. The differences between ocean and land are shown in the right column, and the differences that are statistically significant at the 99% confidence level are indicated using black dots. The bins with a sample size fewer than 30 are hatched. The black boxes highlight the low-CAPE regime ($CAPE^{1/2}$ ¡ 25 [m s^{-1}]).

$\text{CAPE}^{1/2}$ with a slope of about 1.5 [km^{-2} yr^{-1} m^{-1} s]. Over the ocean, however, the changes in f with increasing $\text{CAPE}^{1/2}$ is nonlinear and can be divided into two segments around $\text{CAPE}^{1/2} = 15$ [m s^{-1}]. When $\text{CAPE}^{1/2} < 15$ [m s^{-1}], f increases with CAPE slowly with at the rate of about 0.3 [km^{-2} yr^{-1} m^{-1} s]. Once CAPE exceeds 15 [m s^{-1}], however, f increased rapidly with CAPE with the slope of about 2.4 [km^{-2} yr^{-1} m^{-1} s]. While there exists a non-negligible spread in f for given CAPE both over land and the ocean, the standard error in the slope is relatively small (0.02 over land, and 0.03 and 0.11 for the low-CAPE and high-CAPE regime over ocean, respectively), indicating that there exists a robust trend of increasing f with increasing CAPE. It is also noted that the difference in the slopes between the low-CAPE and high-CAPE environment over the ocean are statistically significant at the 99% confidence level. The nonlinear CAPE-f relationship can be inferred from the findings of Solomon and Baker (1994), who suggested that a threshold value in CAPE must be reached before a significant charge separation can be generated. However, our results show that the nonlinear CAPE-f relationship exists primarily over the ocean, while in Solomon and Baker (1994) they investigated a continental storm and did not mention any land-ocean difference in the CAPE threshold value.

Previous studies have hypothesized that the entrainment effect is the key to land-ocean f difference, where the drier and deeper subcloud mixed layer causes the convective updrafts over land to be wider and better protected from the effects of the entrainment of environmental dry air. Based on this entrainment hypothesis, it is intuitive to speculate that the suppressed f over ocean (i.e., the CAPE-threshold for f) is due to storm size being smaller. To test this, we composite in Figure 4.8 a few properties of the convective storms in the same manner f is composited in Figure 4.6. To highlight the part where the land-sea differences in f are most pronounced, the low-CAPE regime (i.e., $\text{CAPE}^{1/2} < 25$ [m s^{-1}]) is indicated with a rectangle (black solid line). We first compare the composite number of convective pixels ($T_b < 210$ K) as a gross measure of the intensity of the convective systems (Figure 4.8a - 4.8c). Not surprisingly, the total number of convective pixels increases with both $\text{CAPE}^{1/2}$ and P and is generally larger over the land (Figure 4.8c), indicating that there are generally

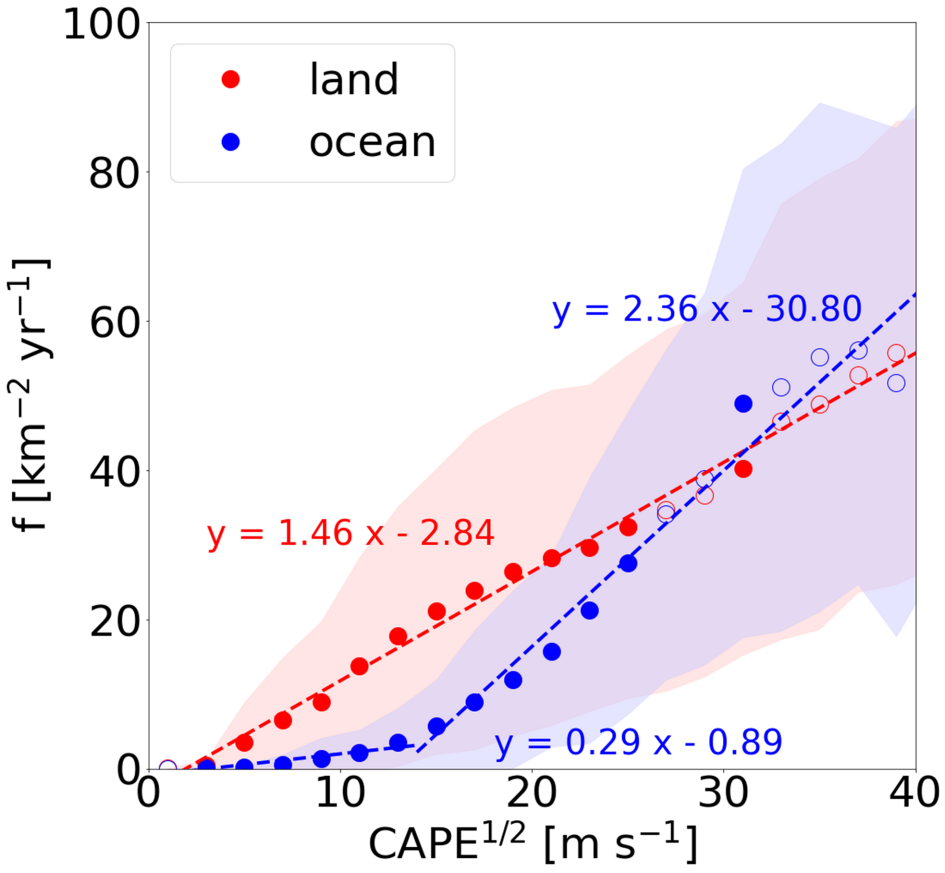

Figure 4.7: The composite lightning flash density (f; [km^{-2} yr^{-1}]) as a function of CAPE$^{1/2}$ [m s^{-1}] over the Central America land region (red) and ocean region (blue). The closed circles indicate the difference in f between land and ocean is statistically significant at the 99% confidence level. The red and blue shadings indicate the range within one standard deviation from the composite mean. The best-fitted lines for land and ocean are shown in the dashed line. For ocean grid points, the regression lines are obtained separately for CAPE1/2 values smaller and greater than 15 [m s^{-1}] (black dotted line).

fewer intense convective activities over the ocean, given CAPE and P. Although oceanic convection has fewer convective pixels than continental convection, N_{CCO} is generally larger over the ocean when P is greater than 0.5 [mm], particularly in the low-CAPE regime (Figure 4.8d - 4.8f). With a fewer number of convective pixels but a larger N_{CCO}, oceanic storms are generally smaller than continental storms, which is evidenced by the difference in A_{CCO} (Figure 4.8i).

Figures 4.9a – b display different statistics of OTs as a function of CAPE and P. In general, the changes in total OTA on the CAPE-P space agrees well with that of convective pixels (Figure 4.8a – b), and the trends of OTA_{CCO} are also similar to that of A_{CCO}, as the OTA_{CCO} is well correlated with A_{CCO} (Figure 4.6). On the other hand, the number of OTs exhibits a trend that is opposite to that of N_{CCO} (Figure 4.8d - f). This result suggests that while there are more CCOs over the ocean than over land for given CAPE and P, the oceanic CCOs are smaller and contain fewer OTs. In other words, oceanic convection is generally more scattered and weaker.

While the larger A_{CCO} and OTA_{CCO} over land seem to be supporting the entrainment hypothesis that the higher f over land is due to land convective updrafts are better protected from dilution because they are embedded in larger storms, the land-sea differences in A_{CCO} are similar across all CAPE bins (Figure 4.10). Together with Figure 4.7, which shows that the land-sea difference in f that appears most strongly in the low-CAPE regime, the results presented in Figure 4.10 suggest that the sensitivity of f to A_{CCO} and OTA_{CCO} varies with CAPE.

In Figure 4.11, f is plotted as a function of $\text{CAPE}^{1/2}$ and A_{CCO}. As expected, f increases with $\text{CAPE}^{1/2}$ for any given bins of A_{CCO} over both land and ocean. On the other hand, for any given CAPE, f also increases with A_{CCO}, which is likely due to that the updrafts embedded within larger storms are better protected from the mixing with environmental dry air. It is important to note that there exists an L-shape pattern of the constant f lines in Figure 4.11a, where f loses its sensitivity to either variable when the other is too small. The L-shape pattern comes largely from the lightning intensity (Figure 4.11g – i), while

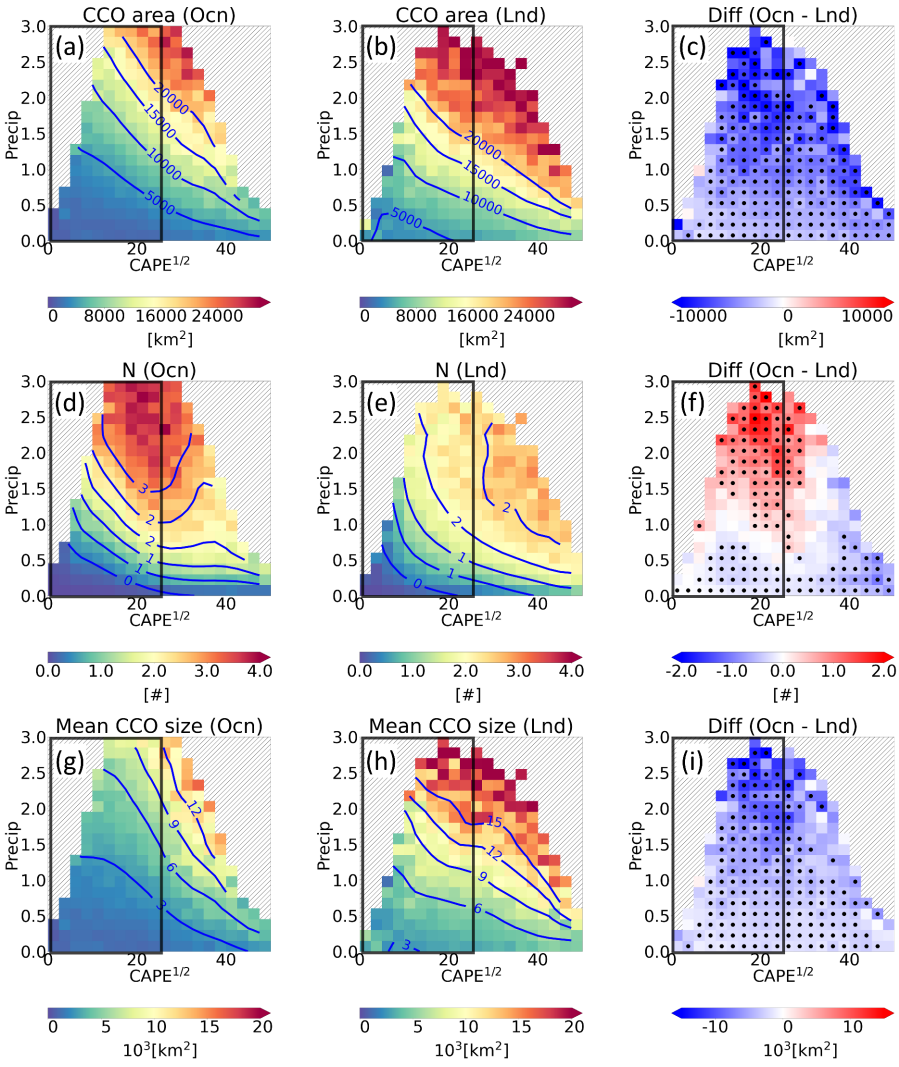

Figure 4.8: Same as Figure 4.6, except that the shadings are (a - c) the CCO area [km^2], (d - f) the number of CCOs [#], and (g - i) the mean CCO size [km^2].

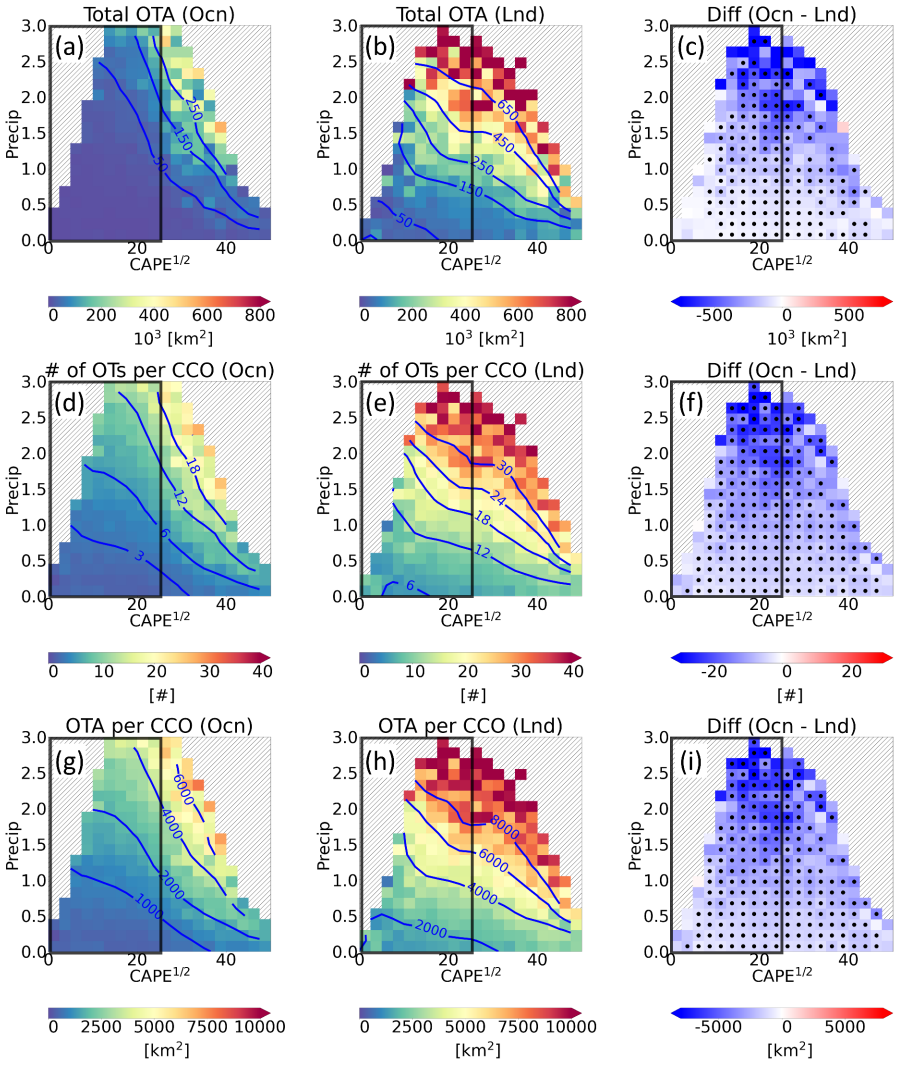

Figure 4.9: Same as Figure 4.6, except that the shadings are (a - c) the total OTA [km^2], (d - f) the number of OTs per CCO [#], and (g - i) the OTA per CCO [km^2].

the probability of lightning is more of a function of $\text{CAPE}^{1/2}$ (Figure 4.11d – f). In the upper left part in the CAPE-A_{CCO} space, f is in the 'CAPE-dependent regime', where f is largely a function of $\text{CAPE}^{1/2}$ and is insensitive to the changes in A_{CCO}. The opposite is the case in the lower right part, which will be referred to as 'size-dependent regime'. In the size-dependent regime, f is largely regulated by A_{CCO}, and its dependency on $\text{CAPE}^{1/2}$ is relatively weak. Similarly, it is found that f also increases with OTA_{CCO} (Figure 4.12). The similarity between Figure 4.11 and 4.12 is not surprising, given that A_{CCO} and OTA_{CCO} are well-correlated (Figure 4.5), but it is worth highlighting that the number of overshooting tops required for storms to produce lightning also appears to be disproportionately high in the low-CAPE regime.

4.4 Discussions

4.4.1 Updraft velocity threshold for lightning

The L-shape pattern in Figure 4.11a supports the hypothesis of the updraft speed threshold for lightning: in the low-CAPE environment, since the environmental forcing is relatively weak, the updrafts are unable to exceed the updraft speed threshold unless the storms are disproportionally large and protected near perfectly from the environmental dry air. In this regime, f is limited by CAPE, and increasing updraft width can only provide limited help to increase the updraft speed, thus f is more sensitive to CAPE. On the other hand, in the high-CAPE environment, since the environmental forcing is large, the storm size becomes the limiting factor for reaching the updraft speed threshold. For example, it is shown in Figure 4.11a that when CAPE1/2 is smaller than 20 [m s^{-1}], f is below 40 [km^{-2} yr^{-1}] even for A_{CCO} as large as 10,000 [km^2]. On the other hand, when $\text{CAPE}^{1/2}$ is greater than 40 [m s^{-1}], even the storms with a OTA_{CCO} smaller than 2,000 [km^2] can produce f greater than 50 [km^{-2} yr^{-1}].

A plausible hypothesis for the CAPE-threshold for lightning over the ocean is that the generation of lightning requires the updraft speed to exceed a certain threshold. The updraft

speed threshold for lightning generation has been reported in previous studies and three possible mechanisms have been proposed. In Williams (1992), it was speculated that the mass of ice-phase condensates and their collision rates in the mixed-phase region (where 0°C $\geq$ T $\geq$ -40°C) is nonlinearly associated with the updraft speed. The second mechanism was proposed by Zipser and Lutz (1994), who argued that when the updraft speed is weaker than a certain value (i.e., 6 - 7 [m s^{-1}] in 0°C to -20°C temperature range), the mixed-phase region is dominated by small ice particles. In this case, the formation of the large/riming particles is prohibited because the supercooled liquid water is quickly depleted. Therefore, the charge separation process can only be effective when the updraft speed is greater than a certain threshold. The third mechanism was based on a modeling study of New Mexico thunderstorms performed by Solomon and Baker (1994), in which they found that graupel particles cannot remain suspended in the charging zone (where -10°C $\geq$ T $\geq$ -25°C) when updraft speed is less than a certain threshold value ($\sim$ 2.5 [m s^{-1}]). Based on the modeling results, they suggested that the CAPE must be greater than a threshold ($\sim$ 400 [J kg^{-1}]) for lightning to be triggered in thunderstorms. A further investigation into the microphysics of charge separation processes is needed to shed some light on the physical relationship between updraft velocity and the generation of lightning.

It is worthwhile to note that the L-shape pattern is less apparent over land (Figure 4.11a and 4.11h), which may suggest that the entrainment effect on f in the low-CAPE regime is much weaker over land. This may imply that there are other mechanisms over land that can promote the generation of lightning in the low-CAPE environment, as continental convection tends to have a higher probability of lightning for the smallest storms in the low-CAPE environment (i.e., $A_{CCO} \leq 2000$ [km^2] in Figure 4.11f). There are a few factors that may explain the higher f over land in the low-CAPE environment. Firstly, the higher aerosol concentration over land may lead to more invigorated convection (Talukdar et al., 2019), which may cause the convective cores to be elevated, resulting in a higher concentration of mixed-phase particles and therefore higher f (Stolz et al., 2015, 2017; Thornton et al., 2017). The aerosol effect can directly affect the probability of lightning, even when the storm

sizes are small. Secondly, the effect of the topography may provide mechanical lifting, where the additional lifting force may assist the updraft to reach the updraft velocity threshold to produce lightning in the low-CAPE environment. More detailed observations on the profiles of updraft velocity, aerosol, and the effect of topography are therefore needed to better understand the necessary environmental conditions to generate lightning.

4.4.2 Implications on electrified shower clouds and global electric circuit

The global electric circuit (GEC) is the electrical pathway by which charge is exchanged between the conductive Earth's surface and the conductive ionosphere: the negative charge is transferred to Earth's surface under the electrified storms, and transferred back to the atmosphere in the fair weather region. In the early study on the atmospheric electricity, Wilson (1920; hereafter W20) speculated that thunderclouds and electrified shower clouds (ESCs) are the two main generators for the GEC. Here, the ESCs in W20 are defined as the electrified clouds in which the charge separation process is operating, but the potentials just fall short of what is required to produce lightning discharges. Despite that lightning is absent in ESCs, W20 hypothesized that the descent of negatively charged precipitation from ESCs still served as a key component to maintain the GEC.

Since no measurement of ESCs was available, W20's hypothesis can only be tested in the early days using the thunder day observations. By compiling the thunder day reports from surface meteorological stations worldwide, Whipple (1929) showed a clear similarity between the curve of global thunder days and the diurnal variations of the electric field (the Carnegie curve). This similarity is often held up in support of W20's global circuit hypothesis. However, these two curves differ in two respects: 1) The amplitude variation of the thunder days curve over land is more than twice that of the Carnegie curve; 2) The maximum in the thunder days curve coincides with afternoon thunderstorms in Africa (1400–1500 UTC), whereas the Carnegie curve is maximum when afternoon storms in South America are active (1900–2000 UTC). This discrepancy suggests that the thunderstorms alone are not enough to fully explain the Carnegie curve.

This discrepancy remains a long-standing puzzle, until recent observations support that the ESCs are indeed an important missing piece to the maintenance of GEC. However, the contribution from ESCs to GEC exhibits a marked difference between land and ocean. Mach et al. (2010, 2011) investigated the role of thunderstorms and ESCs as generators in the GEC. They concluded that the mean total conduction current in electrified storms is 2.0 kA globally, where contributions to the GEC from land and ocean thunderstorms are 1.1 and 0.7 kA, respectively, and electrified shower clouds contribute 0.04 and 0.22 kA for land and ocean storms, respectively. By using TRMM PR observations, Liu et al. (2010) categorized ESCs as the deep convective clouds with mixed phase processes (the maximum height of 30 dBZ $<$ -10 (-17) °C over land (ocean), but without single lightning flash observed. They also found that ESCs are much more frequent over the ocean, and the diurnal variation of precipitation from thunderstorms and ESCs match closely with the Carnegie curve. They concluded that the contribution of the ESCs to the GEC is not negligible in comparison with the thunderstorm contribution.

While these studies have provided new insights into the physical maintenance of GEC, it is not yet clear why ESCs are much more frequent over the ocean. Our study shows that this is because most oceanic convection is triggered in low-CAPE environment (89% of the oceanic convection is in the environment with $\mathrm{CAPE}^{1/2} < 30$ [m s^{-1}]). In this low-CAPE environment, for convection to produce frequent lightning, storms have to grow exceptionally large, as shown in Figure 4.11. As a consequence, most oceanic convection is unable to reach the critical updraft velocity to produce frequent lightning. However, charge separation processes are still involved in most of the oceanic deep convection, hence leading to the formation of ESCs over the ocean.

Based on the results presented in this Chapter, I argue that the land-sea differences in the ESCs are related to two factors: (i) CAPE is typically lower over ocean, so that oceanic convection requires larger storm size to produce frequent lightning, and hence less oceanic storms can produce frequent lightning and more ESCs over ocean; (ii) Oceanic storms are generally less clustered, which makes the oceanic storms even more difficult to reach the

critical storm size to produce frequent lightning. The combined effect of these two factors leads to more frequent ESCs over ocean, which is often neglected due to limited ESCs observations over the ocean.

4.5 Implications on improving lightning parameterization schemes

To illustrate the influence of the CAPE-threshold for f over the tropical ocean on the performance of the R14 parameterization, a simple modification is made to R14's formulation. In the modified scheme, the lightning flash density over the ocean (f_o) is parameterized as:

$$f_o = \begin{cases} 0 & \text{if CAPE} < 625 \\ CAPE \times P & \text{if CAPE} \geq 625 \end{cases} \tag{4.4}$$

With Eq. 4.4, oceanic lightning is eliminated in the low-CAPE environment based on the observations in Figure 4.7. While the atmosphere is relatively stable and is not expected to be associated with high f in the low-CAPE environment, an accurate representation of f in such environment is still of significance because the majority of the oceanic environment falls into the low-CAPE regime. Figure 4.13 shows that the majority of the oceanic storms (about 80%) occur in the low-CAPE environment with $\text{CAPE}^{1/2} < 25$ [m s^{-1}].

The observed climatology maps of f and CAPE over the Central America area (35°S – 35°N, 30°W – 150°W) during 2012 – 2015 are shown in Figures 4.14a and 4.14b, respectively. In observations, the land-sea f ratio is about 4.3. Figure 4.14c shows the estimated f using the original R14 scheme, which overestimates the lightning over the ocean with the land-sea f ratio of about 2.9. In Figure 4.14c, f is overestimated most apparently in two regions: the equatorial Atlantic region (5°S – 10°N, 30°W – 60°W); and the equatorial Pacific region (0°N – 10°N, 120°W – 150°W). Over these two regions, CAPE is generally smaller than 600 [J kg^{-1}] (Figure 4.14b). With the modified R14 scheme (Eq. 4.4), the land-sea f ratio increases substantially (about 4.5) and becomes closer to the observed value (Figure 4.14d). The improvement mainly comes from reducing f in the oceanic regions where the

climatological CAPE is low. This result strongly suggests that it is necessary to implement a CAPE-threshold in CAPE-based lightning parameterization schemes.

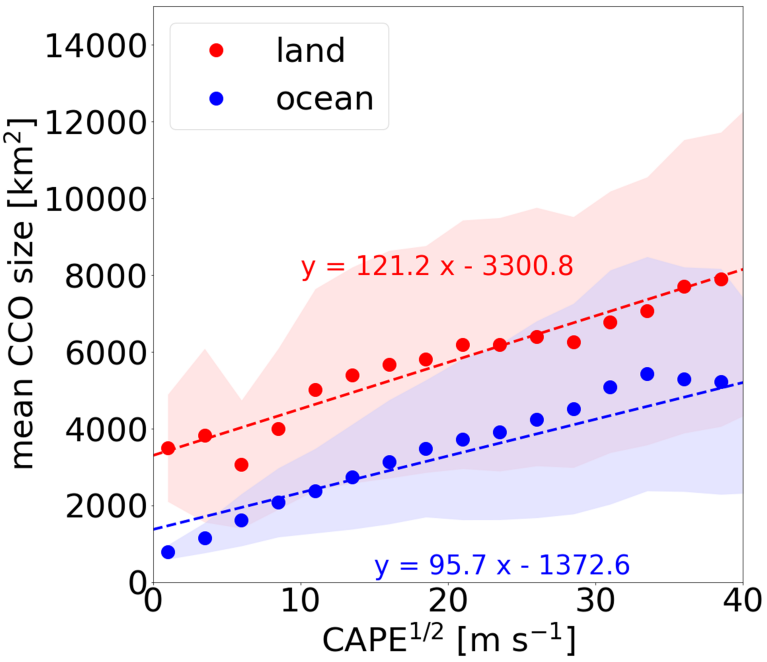

Figure 4.10: Same as Figure 4.7, except the y-axis shows the mean CCO size [km^2].

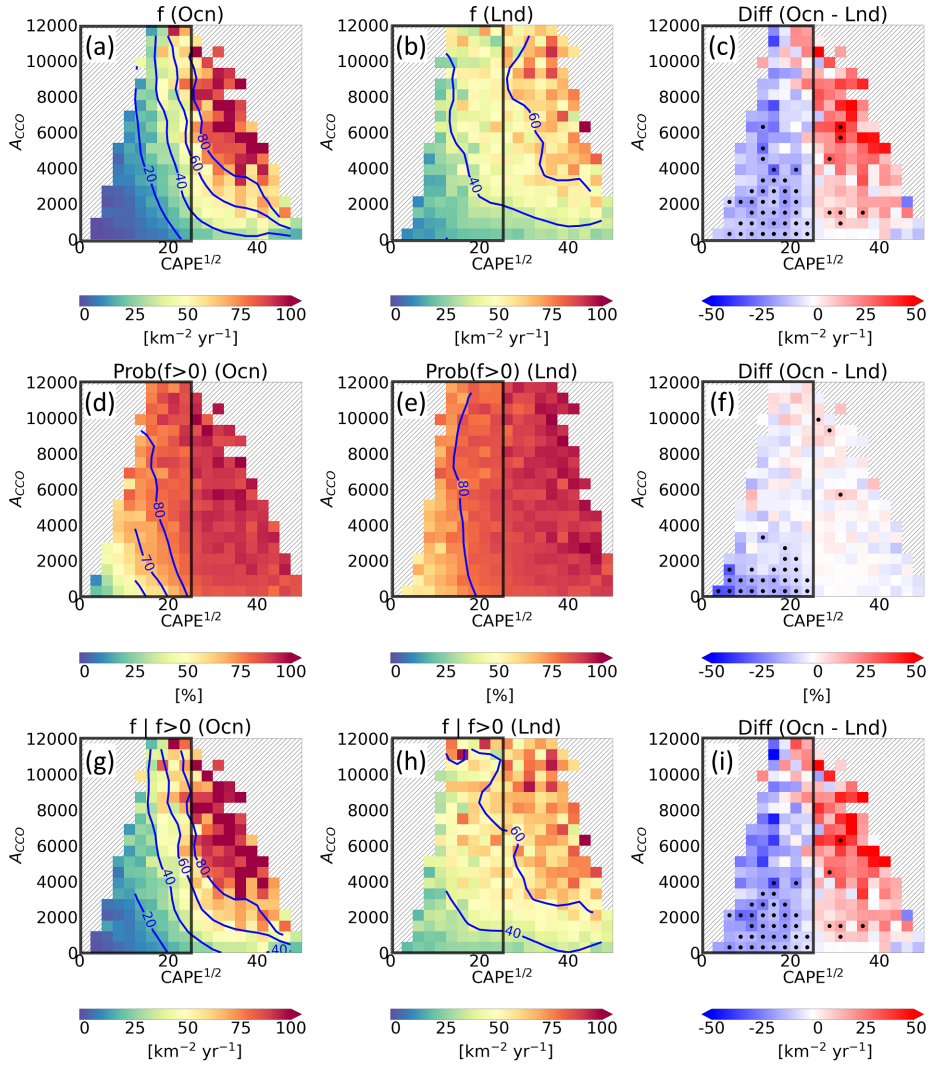

Figure 4.11: Same as Figure 4.6, except that the y-axis shows the A_{CCO} [km2].

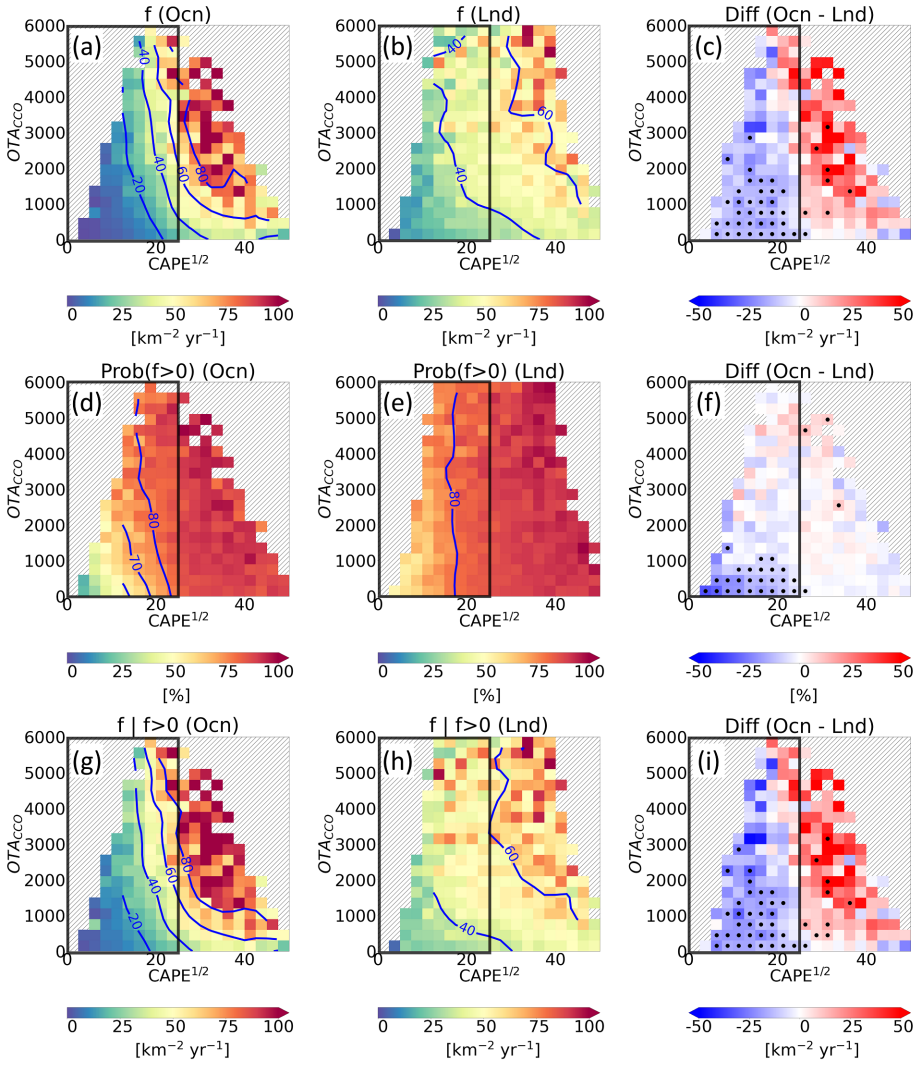

Figure 4.12: Same as Figure 4.6, except that the y-axis shows the OTA_{CCO} [km2].

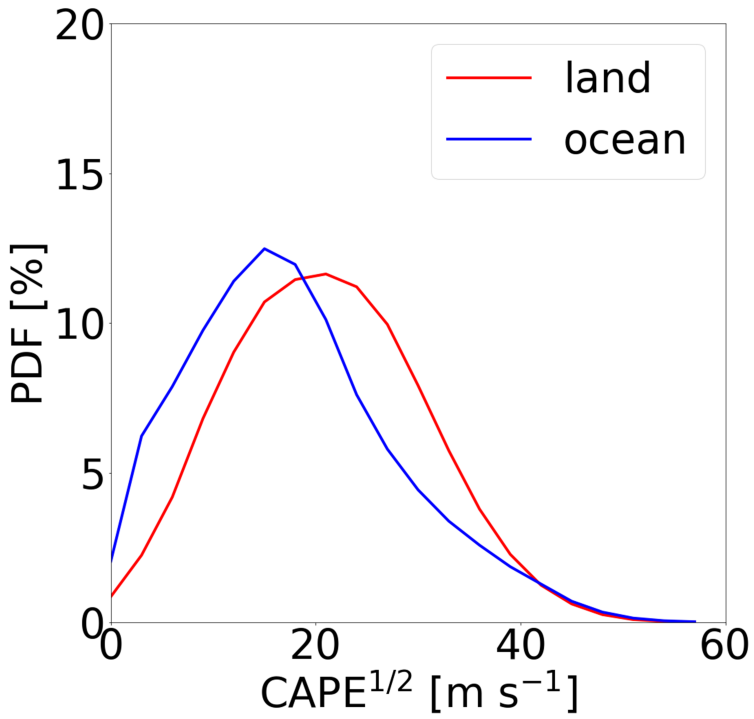

Figure 4.13: The probability distribution function (PDF; [%]) of CAPE$^{1/2}$ [m s^{-1}] over land region (red curve) and ocean region (blue curve).

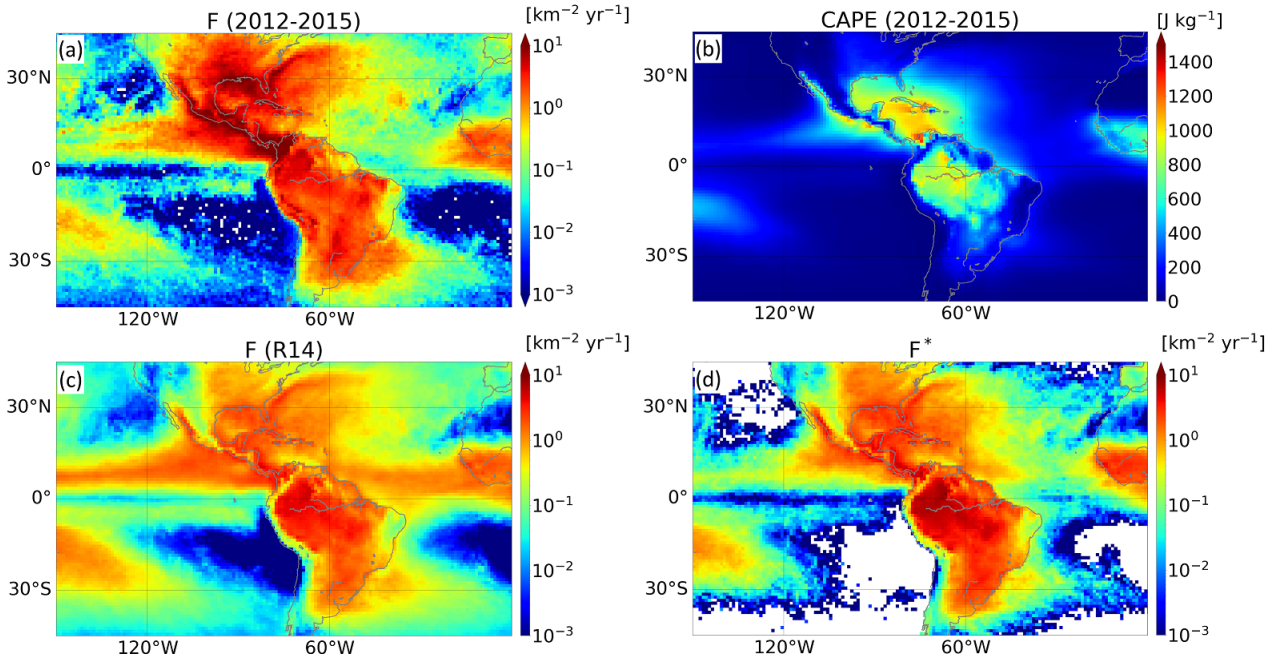

Figure 4.14: The climatology map of (a) observed lightning flash density (f) [km^{-2} yr^{-1}], (b) CAPE [J kg^{-1}], (c) f from the original R14 method, and (d) f from the modified R14 method (Eq. 4.4). In (c) and (d), f is normalized such that the total lightning counts are the same as (a).

Chapter 5

MACHINE-LEARNING-BASED LIGHTNING PARAMETERIZATION SCHEMES: IMPLEMENTATION AND THEIR FORECAST SKILLS

In this chapter, I will assess the extent to which machine learning (ML) techniques can help improve the lightning forecast skill. One way of forecasting lightning is by utilizing atmospheric models (e.g., GCMs, NWP models, etc.), with a lightning parameterization scheme that produces lightning flash density using other information available in the host model. As an example, one can use atmospheric models to forecast CAPE and precipitation, and use these variables to represent the number of lightning flashes using lightning parameterization schemes, such as those proposed by Romps et al. (2014). Under this strategy, the lightning forecast skill will be limited by: (i) the forecast skill of the large-scale variables from atmospheric models, and (ii) the accuracy of lightning parameterization schemes. The objective of this study is to examine the extent to which we can improve the lightning forecast skill by improving the accuracy of lightning parameterization schemes, in particular, by using ML-based methods. I believe ML-based lightning schemes have the potential to achieve better performance within the framework that uses the forecasted large-scale variables as input to the lightning parameterization schemes for the following two reasons. First, unlike the conventional lightning parameterization schemes that are developed based on incomplete physical understanding of lightning, ML algorithms can potentially find the best representation of lightning by optimizing the thousands of free internal model parameters determined using the training data. While the input variables of conventional lightning parameterization schemes contain the information that are critical to lightning generation, the mathematical formulas are constrained to be simple so that they remain human-interpretable. The sim-

plicity of the formulas can sacrifice the performance, especially when the exact formula is unknown. Therefore, even with the same input variables, ML-based lightning parameterization schemes have the potential to perform better. Second, while the physical mechanisms of lightning are not yet fully understood, there are likely other important factors that are not used as inputs when using the conventional approaches. The ML-based lightning schemes can expand the input variables easily, which may help us utilize the information that are potentially important for lightning generation, but are missing in the conventional schemes.

The rest of this chapter is organized as follows. The ML algorithms used to find the best representation of lightning using large-scale variables, and the datasets used in this Chapter, will be introduced in Chapter 5.1. I will then apply the ML models to build the relationship between large-scale variables and lightning by using observations, and to examine if the ML-based lightning schemes have the potential to perform better than conventional approaches in Chapter 5.2. Finally, ML-based lightning schemes will be used to evaluate the extent to which the lightning forecast skill can be improved by using a more accurate lightning schemes using ML techniques in Chapter 5.3.

5.1 Data and Machine Learning Algorithms

5.1.1 Data

The datasets used for training the ML models are summarized in Table 5.1 and 5.2. Two separate datasets are used as inputs for the training tasks, and the lightning flash density (f) will be provided by WWLLN as output fields for both tasks. In Chapter 5.2, I will evaluate the performance of ML-based lightning schemes using the observed large-scale variables as inputs. The input variables include precipitation (P) from TRMM, and variables provided by ERA5 reanalysis (see Chapter 4.2 for data description), including CAPE, 500-hPa geopotential height (Z500), 1000-hPa geopotential height (Z1000), thickness between 300-hPa and 700-hPa levels (Z300-700), and 2-meter temperature (T2M). Besides CAPE and P, Z500 and Z300-700 are selected because the spatial patterns of these variables capture

the evolution of synoptic-scale disturbances in the mid-latitudes (Weyn et al., 2019), while Z1000 and T2M are important surface parameters that are often used as input features in ML models to represent deep convection (Mostajabi et al., 2019; Ukkonen and Mäkelä, 2019). The analysis domain is over the contiguous United States (CONUS) area. The data are collected from 1 Jan 2010 to 31 Dec 2019. The original temporal resolution is 3 hours for TRMM, and 1 hour for ERA5, with spatial resolution of 0.25 °for both datasets. All data used in this study are coarse-grained to daily temporal resolution and 1°by 1°spatial resolution via temporal and spatial averaging. The time periods from 2010 - 2015 were used for model training, and 2016 were used for model validation. Data from 2017 - 2019 were set aside for the testing dataset used for final model performance evaluation.

In Chapter 5.3, I will evaluate the lightning forecast skill of ML models that take the forecasted large-scale variables as inputs. These large-scale variables will be provided by the hindcast dataset from NCEP Global Ensemble Forecast System (GEFS). The current GEFS version (v11) uses semi-Lagrangian dynamics with 64 vertical levels (Zhou et al., 2017). The forecasts consist of model integrations that start every 7 days from 6 Jan 1999 to 28 Dec 2016, and each integration run for 35 days. Here we use only the forecasts that starts from 6 Jan 2010 to 28 Dec 2016, for a total of 365 forecasts. The model horizontal resolution is 34 [km] for forecast days 1 to 8, and then decreases to 70 [km] for forecast days 9 to 35. The GEFS hindcast dataset were assembled in support of NOAA's Subseasonal Experiment (SubX), a Climate Testbed project focused on subseasonal predictability and predictions. Daily (UTC) averages of forecasted fields are provided for the SubX project at 1°by 1°horizontal resolution. Each start has 11 ensemble members (1 control and 10 perturbed members generated using an ensemble Kalman filter), and only the ensemble means are considered here. The input variables include CAPE, P, surface temperature (Ts), surface dew point temperature (Tds), and large-scale vertical motion at 500-hPa (w500). Note that the input variables are different than that in Chapter 5.2) because there is significant amount of missing data in geopotential height in the GEFS dataset. The 7 years of data (2010 - 2016) are randomly separated into training and testing dataset with the ratio of 5:2.

Table 5.1: A brief description of the datasets used in Chapter 5.2.

Dataset	Variable Acronym	Description	Period
WWLLN	f	Lightning flash density	2010 - 2019
TRMM	P	Precipitation	
ERA5	CAPE	Convective available potential energy	
	Z500	500 hPa geopotential height	
	Z1000	1000 hPa geopotential height	
	Z300-700	Thickness between the levels between 300 hPa and 700 hPa	
	T2M	2-meter temperature	

Table 5.2: A brief description of the datasets used in Chapter 5.3

Dataset	Variable Acronym	Description	Period
WWLLN	f	Lightning flash density	2010 - 2016
GEFS	CAPE	Convective available potential energy	
	P	Precipitation	
	Ts	Surface temperature	
	Tds	Surface dew point temperature	
	w500	Large-scale vertical motion at 500 hPa	

5.1.2 Machine learning algorithms

Enabled by the lightning dataset provided by WWLLN, I use the supervised ML techniques to build the relationship between large-scale variables and lightning frequency. Supervised learning is a subset of ML, where the labeled datasets will be provided to train the ML models to map an input to an output. In each supervised ML model, there are many free model parameters within the model, whose values will be determined through the training process. During the training process, the accuracy of the ML models will be measured by the cost function, which is a measure of the difference between the predicted values and the values from labeled data. The ML algorithms are designed to adjust these free model parameters in the ML model to minimize the cost function. For each of the ML

model, there is also another kind of parameter that cannot be directly learned from the regular training process. These parameters express "higher-level" properties of the model, and are therefore called hyperparameters. Hyperparameters are usually fixed before the actual training process begins.

In the applications of lightning schemes in the current study, the ML algorithms will be categorized into two classes: (1) the column-based approach, where the input variables are the atmospheric variables in a given grid, and the output variable is f of the same grid. This approach is similar to the traditional lightning parameterization methods, where a quasi-equilibrium state is assumed in a grid so that f can be represented using grid-mean atmospheric state variables; and (2) the map-based approach, where the inputs are a set of two-dimensional maps of different atmospheric variables, and the output is also the map of f. In this approach, the ML models are fed not only with the local information, but also the information from adjacent cells. The map-based approach may have a higher potential than the column-based approaches if the large-scale weather pattern contains some information about the unresolved processes that are important for lightning generation, which is a hypothesis that can be tested by examining the performance of the column- and map-based approaches.

Here I use a few supervised machine learning techniques that are suitable for our purpose, and the explored hyperparameter space and resulting optimal values are shown in Table 5.3.:

Random Forest (RF)

RF is an ML estimator that consists of an ensemble of individual decision trees, and the schematics of the RF architecture is shown in Figure 5.1. The decision tree is a flowchart-like structure in which each internal node represents a test on an input variable, and each node will be split into two branches based on the outcome of the test, and the end node (or leaf node) represents a prediction following all test results made previously. Decision trees are constructed via an algorithmic approach that identifies ways to minimize the entropy in the dataset, so that the labeled output data in each end node will be as homogeneous

as possible. For a given input sample, each individual decision tree in an RF model will make a prediction, and the model's final prediction is determined by the majority vote of the decision trees in it. The purpose of having multiple trees is to reduce the variance of the prediction since individual decision trees are prone to overfitting. RFs are widely used as they generate reasonable predictions across a wide range of data while requiring little configuration and do not require heavy preprocessing of data.

In this study, RF will be used as a column-based method, where the atmospheric variables in a grid cell will be the input variables, and the outputs will be the observed lightning frequency in the grid cell.

Neural Networks (NN)

NN will be used as a column-based method in this study. NN are composed of a set of connected nodes (neurons), with the structure of an input layer, one or more hidden layers, and an output layer. The schematics of the NN architecture is illustrated in Figure 5.2. Each node connects to another and has an associated weight and threshold, and the weight at each node will be determined through the training process. Depending on the activation function, the output of any individual node may determine if that node is activated, which controls whether the node's output will be passed along to the next layer of the network. There can also be multiple layers of nodes, with the outputs of one layer becoming the inputs to the next layer (i.e., deep neural network). By using multiple layers of transformations, deep neural networks are able to capture complex, hierarchical interactions between features. The layers between the input layer and the output layer are called hidden layers because the physical interpretation of their activation is not always clear.

Convolutional Neural Networks (CNN)

CNN is a type of neural network algorithm which are especially useful for image recognition. Specifically, a CNN has one or more layers of convolution units. A convolution unit receives its input from multiple units (in proximity) from the previous layer. Therefore, the

input units (that form a small neighborhood) share their weights, which have two particular advantages when compared to NN. Firstly, the number of units in the network is reduced (since they are many-to-one mappings), such that there are fewer parameters to learn which reduces the chance of overfitting as the model would be less complex than a densely connected NN. Second, the input information is considered altogether in the small neighborhoods. This feature is particularly helpful for applications such as image recognition, as the neighboring inputs (pixels) usually carry related information.

The specific CNN architecture used here is modeled on the popular U-Net architecture (Ronneberger et al., 2015), a variation on traditional encoder-decoder networks (Baldi, 2012). Larraondo et al. (2019) tested several auto-encoder CNN for diagnosing precipitation from geopotential height fields in reanalysis data and found the U-Net can achieve the better performance. Figure 5.3 shows the schematics of the CNN architecture used in this study. Starting from the left in Figure 5.3, the input fields are restructured into the blue rectangles as the state tensor, the blue arrows indicate the convolutional operations, which are then followed by max-pooling operations (indicated as red arrows). The max-pooling operations reduce the spatial dimensionality of the state by a factor of 2 in both horizontal coordinates by taking the maximum value within each 2 x 2 grid. Note that the spatial resolution progressively becomes coarser after each time the convolution operation is applied. While this characteristic allows the CNN to learn ways to represent how lightning is influenced by the large-scale atmospheric patterns, the high-resolution information (of atmospheric fields) is lost during the convolution operations. Finally, the last few layers of the U-net architecture are a mirrored up-sampling process (shown by green arrows), whereby each spatial point of the image is copied to a 2 x 2 sub-grid, doubling the spatial dimensionality until the final convolutional operation yields an output state with the same dimensions as the input. To mitigate the lost high-resolution information, the U-Net concatenates the tensor state of the CNN at each encoding step on the left to the decoding state on the right following each up-sampling operation. This concatenation step allows high-resolution information to be passed from input to output, which enables the CNN architecture to handle complex, multi-scale

weather prediction tasks.

CNN will be used as the only map-based method in this study, where the two-dimensional maps atmospheric variables will be used as the inputs to feed into the CNN model, and the outputs will be the maps of observed lightning frequency, as illustrated in Figure 5.3.

Table 5.3: The hyperparameters of the ML models used in this study

Hyperparameter	Explored space	Selected value
Random Forest (RF)		
Maximum tree depth	2 - 32	20
Number of estimators	10 - 40	40
Neural Networks (NN)		
Number of layers	1 - 4	2
Neurons in each layer	10 - 40	40
Hidden layer activation function	*tanh*, *ReLU*	*ReLU*
Convolutional Neural Networks with U-Net (CNN)		
Number of layers	1 - 4	2
Number of filters	4 - 32	16
Hidden layer activation function	*tanh*, *ReLU*	*ReLU*

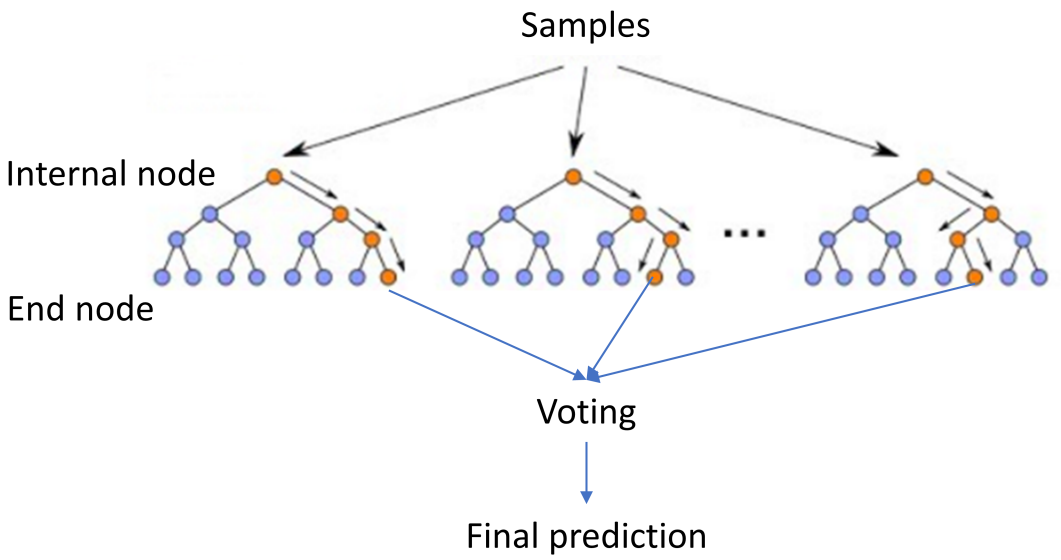

Figure 5.1: Schematic illustrating the architecture of the Random Forest algorithm.

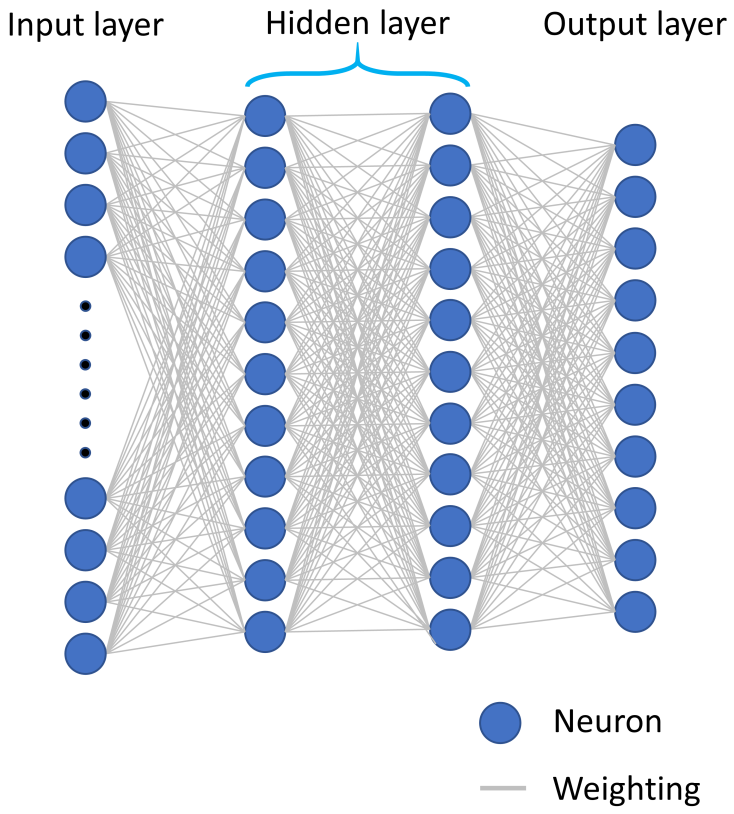

Figure 5.2: Schematic illustrating the architecture of the Neural Networks algorithm.

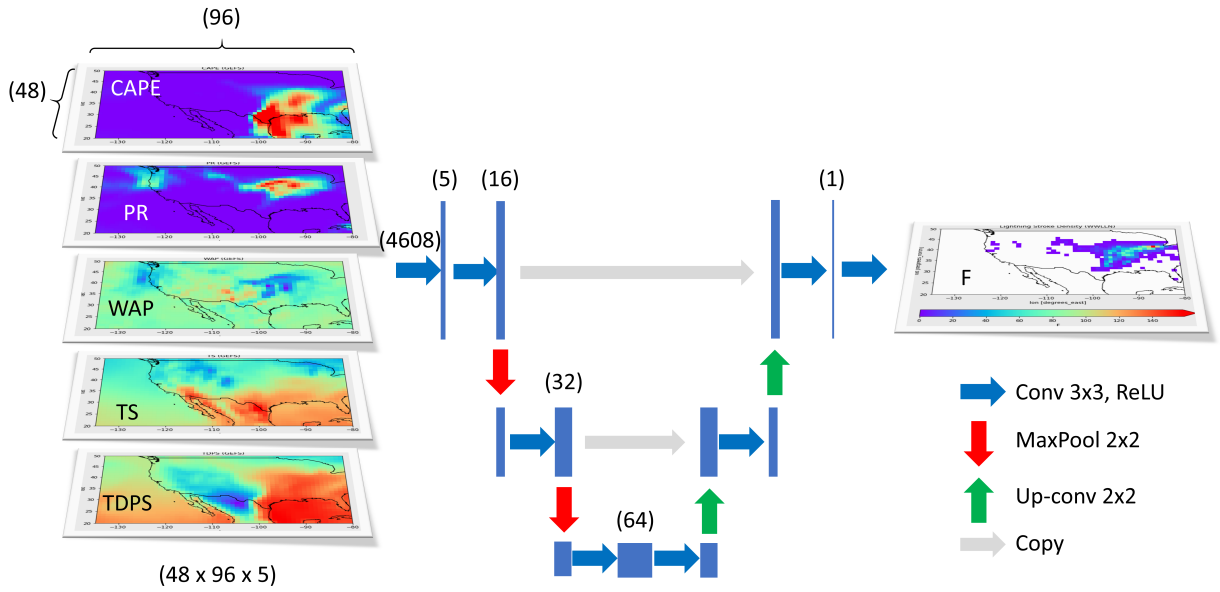

Figure 5.3: Schematic illustrating the architecture of our CNN based on the U-Net architecture. Each blue arrow represents a 2-D convolution, red and green arrows indicate max-pooling and up-sampling operations, respectively. The grey lines represent skip connections, whereby the blue state on the left is copied exactly and concatenated to the state on the right.

5.2 ML-based lightning schemes: implementations and performance

In this section, I implement various types of ML methods to represent f using grid-scale variables obtained from satellite and reanalysis products. As mentioned in the previous section, the ML methods include the column-based method using RF and NN, and the map-based method using CNN with a U-net structure. The performance of the ML-based lightning schemes will then be compared to and evaluated against the benchmark lightning scheme of R14.

5.2.1 Benchmarks

The R14 lightning scheme is used as the benchmark when evaluating the ML-based lightning schemes in this study. The R14 lightning scheme is chosen because studies have demonstrated that the R14 method reasonably replicates the spatial patterns, temporal variation on daily time scale, and seasonal maps of lightning over the CONUS (Romps et al., 2014; Tippett et al., 2018). In addition to its performance, the simplicity of R14 method also adds values to the scheme because the variables used (CAPE and precipitation) can be obtained easily either from observations or atmospheric models. For example, when investigating the predictability of lightning over the CONUS area, Tippett and Koshak (2018) chose the R14 method as their baseline lightning scheme, and used the CAPE and P from weather forecast model to make the lightning frequency forecast.

In this section, the ML models will be trained using the observations (see Table 5.1) from 2010 - 2016, and the performance will be examined using the test dataset from 2017 - 2019. The climatology of f, CAPE, P, and T2M over the CONUS area duing the testing period are shown in Figure 5.4. The performance will be evaluated using the R^2 skill score, which is proportional to the variance in the observed lightning frequency that can be explained by predicted values. Here, we will separate our evaluations into two parts. In the first part, we will evaluate the performance of ML-based lightning schemes by training them using only CAPE and P as input variables. The results of this task will show how much we can improve

the accuracy of lightning schemes by optimizing the simple formula proposed by R14. In the second part, we will increase the number of input variables, to fully capitalize on the strength of ML techniques, which is to find the best fitted relationship by searching through large data. By separating these two tasks, we can differentiate the contribution of ML that is due to the optimization of the mathematical formula from increasing the number of input variables, which may give us some insights on how to further improve the ML-based lightning schemes.

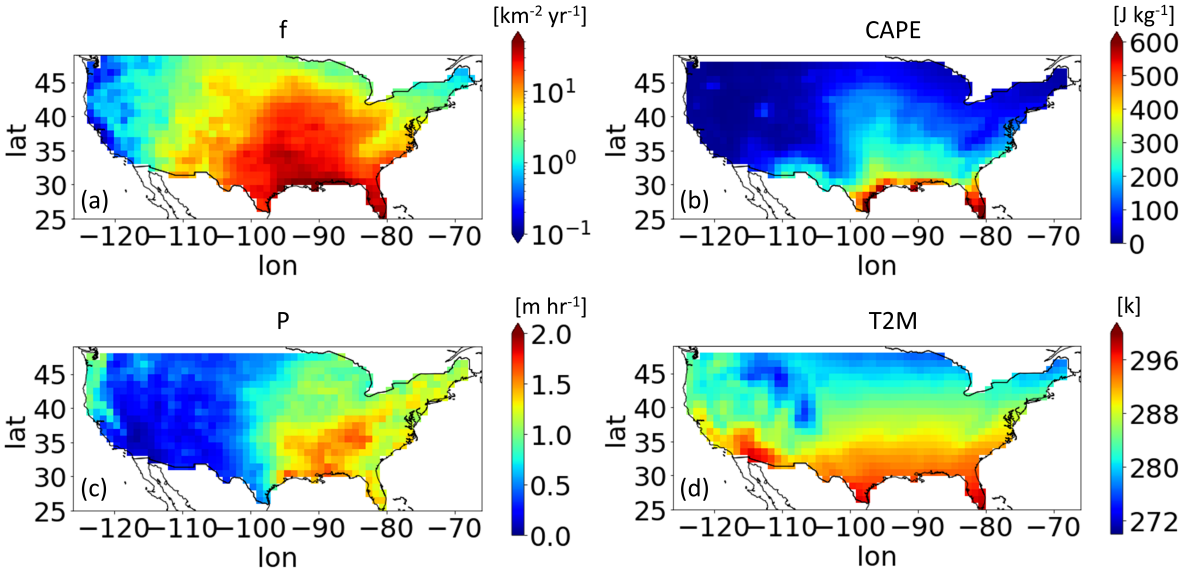

Figure 5.4: The climatology map of (a) f, (b) CAPE, (c) P, and (d) T2M over the CONUS area during the testing period from 2016 - 2019.

5.2.2 Performance

The R^2 score for the parameterized lightning frequency using the benchmark lightning scheme (R14) during the testing period from 2016 - 2019 are shown in Figure 5.5 (a). The results show that R14 generally performs well over CONUS with R^2 score above 0.3 in most regions over CONUS, suggesting the R14 method can explain more than 30% of the variance of the f in most regions over CONUS. It is worth noting that the performance of R14 is lower over the west coast area and the Southwest US, with R^2 score below 0.2. The poor performance over the west coast is likely because the majority of the precipitation over the west coast is non-convective precipitation, so precipitation is not a good estimator for lightning frequency. As for the Southwest region, the poor performance there is likely related to the difficulty in correctly calculating CAPE because of the complex topography.

Figures 5.5 (b) - (c) show the R^2 score for the column-based ML lightning schemes using RF and NN, respectively. The results show that the column-based ML lightning schemes improve the R^2 score over that of R14 over most of the region in the CONUS. The difference in the R^2 score between ML lightning schemes and R14 are shown in 5.6. Quantitatively, the column-based lightning schemes tested in this study improve the R^2 score for more than 0.2 for many regions, in particular, the South and Southeast US. The overall performance of these lightning schemes can be summarized using the f-weighted R^2 score over the CONUS, which gives a higher weighting over regions with more lightning (see Figure 5.4a). The f-weighted R^2 score is 0.24 for R14, 0.29 for RF, and 0.33 for NN. That the column-based ML lightning schemes improve the overall skill score over R14 indicates that there is room for improvement in the simple formula used in R14 method, and our results show that the improvement can be as large as more than 35% increase in the R^2 score with NN.

Figure 5.5 (d) shows the results from the map-based ML lightning scheme of CNN. It is found that the map-based CNN method is able to achieve a better performance when compared to the column-based method. This result may suggest that there are some information in the large-scale weather patterns that are important for lightning generation. In

particular, the large-scale weather patterns may be helpful for lightning parameterization, given that CNN performs better over the Southeast US (Figure 5.5d), because they provide some information about the storm size. For example, this is the region with high-CAPE environment (Figure 5.4b), and from results in the Chapter 4, we know that in the high-CAPE environment, the lightning frequency is less sensitive to CAPE, and is more sensitive to the storm size (Figure 4.11b). For the map-based CNN method, the two-dimensional map of precipitation may be able to provide some information about the scale of the convective systems in this region, to give a more accurate lightning representation. More detailed analysis is needed to determine if the storm size information is helpful for the map-based ML lightning scheme.

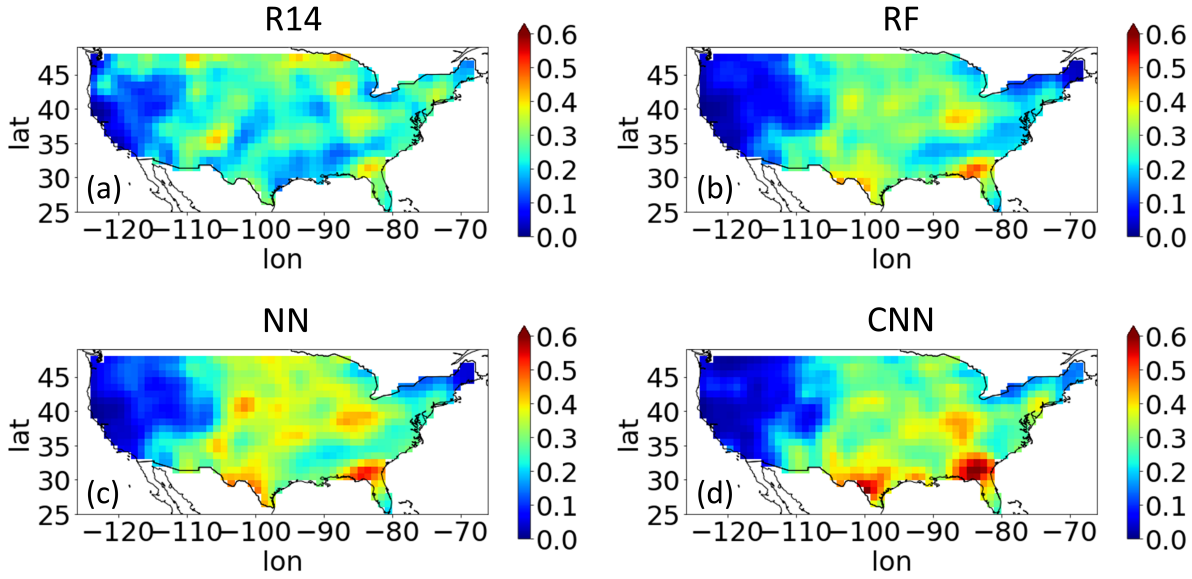

Figure 5.5: The R^2 skill score of lightning frequency for different lightning scheme: (a) R14, (b) RF, (c) NN, and (d) CNN during the testing period from 2016 - 2019. For (b) - (d), the ML models are trained using only CAPE and P as inputs. A Gaussian smoothing is applied to all figures to reduce the noise in the figures.

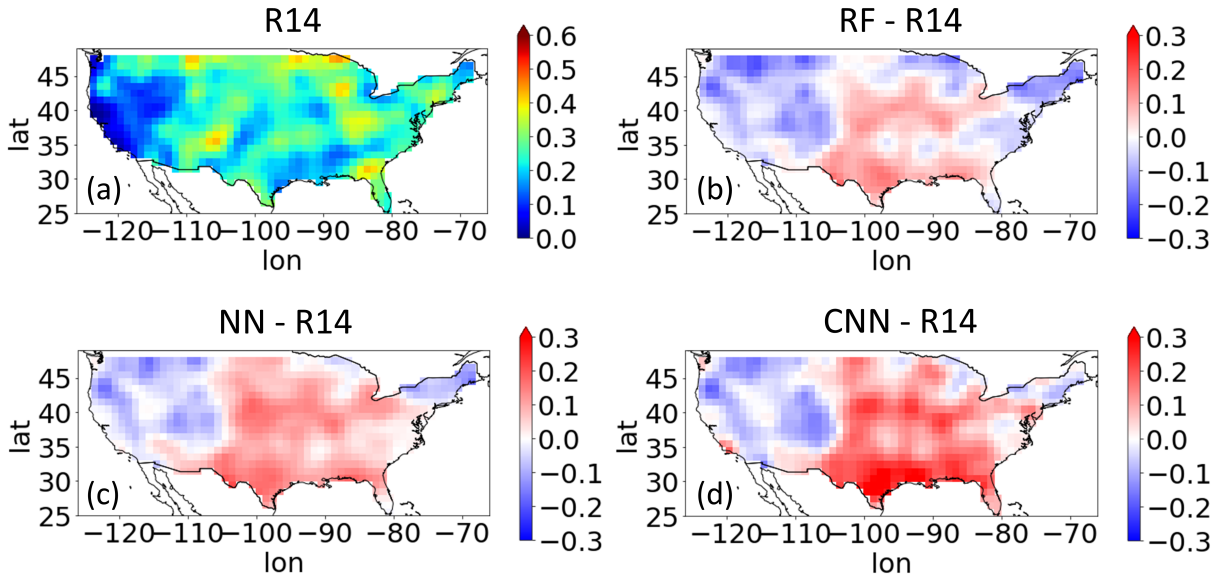

Figure 5.6: Same as Figure 5.5, except for (b) - (d) the shadings show the R^2 score difference between each methods and R14.

Figure 5.7 shows the results of using Z500, Z1000, Z300-700, T2M, in addition to CAPE and P as input to train the ML-based lightning schemes, and the associated difference in R^2 score between ML-based lightning schemes and R14 are shown in Figure 5.8. The figures suggest that increasing the number of input variables can provide more information for the ML methods, both column- and map-based method, to achieve a better performance.

The f-weighted R^2 score for R14 and each ML methods with different input variables are summarized in Figure 5.9. It is found that when all input variables are used, the map-based CNN method shows the best performance overall. In particular, Figure 5.8 shows that the ML methods can improve the R^2 score most significantly over the regions where lightning is more frequent. For example, all ML-based lightning schemes improve the R^2 score in Texas for more than 0.2, and CNN can improve the R^2 score by 0.3 over Florida, when compared to R14.

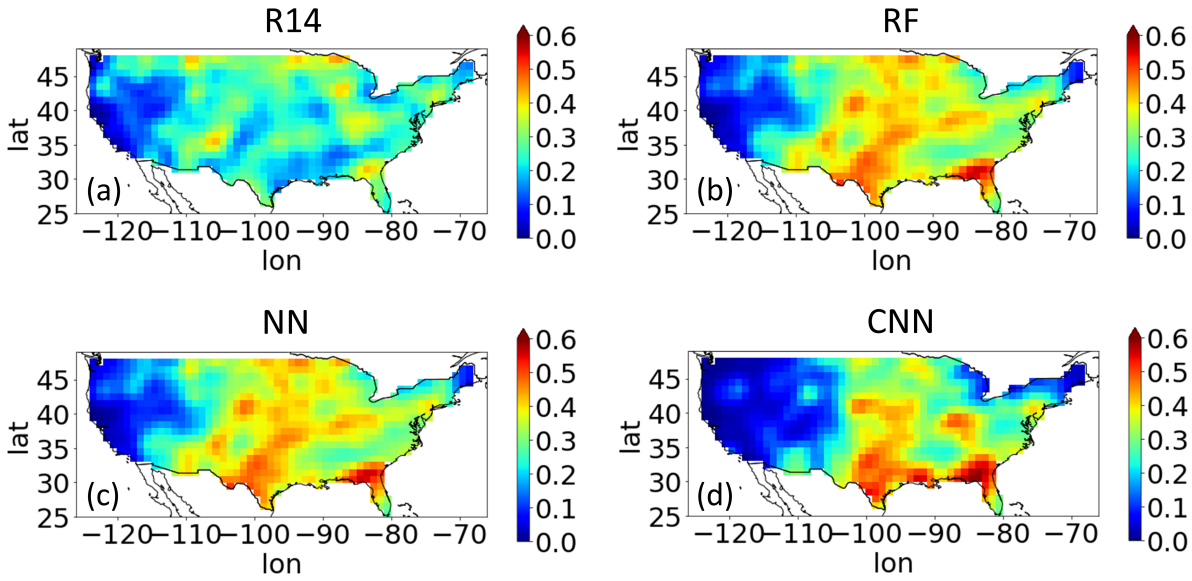

Figure 5.7: Same as Figure 5.5, except for (b) - (d), the ML models are trained using CAPE, P, Z500, Z1000, Z300-700, and T2m as inputs.

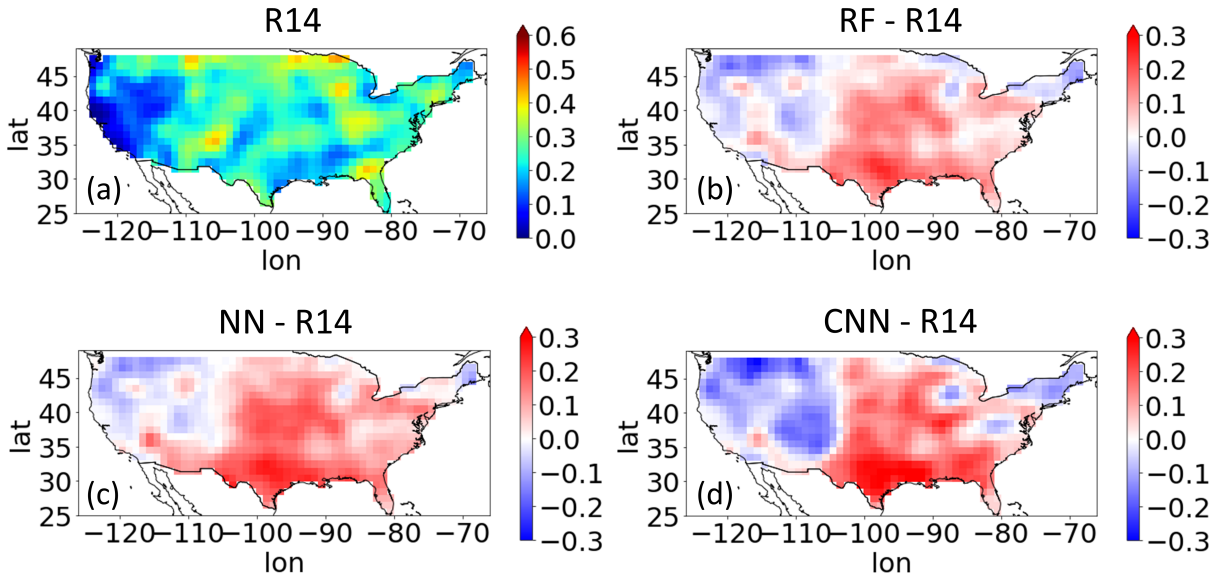

Figure 5.8: Same as Figure 5.7, except for (b) - (d) the shadings show the R^2 score difference between each methods and R14.

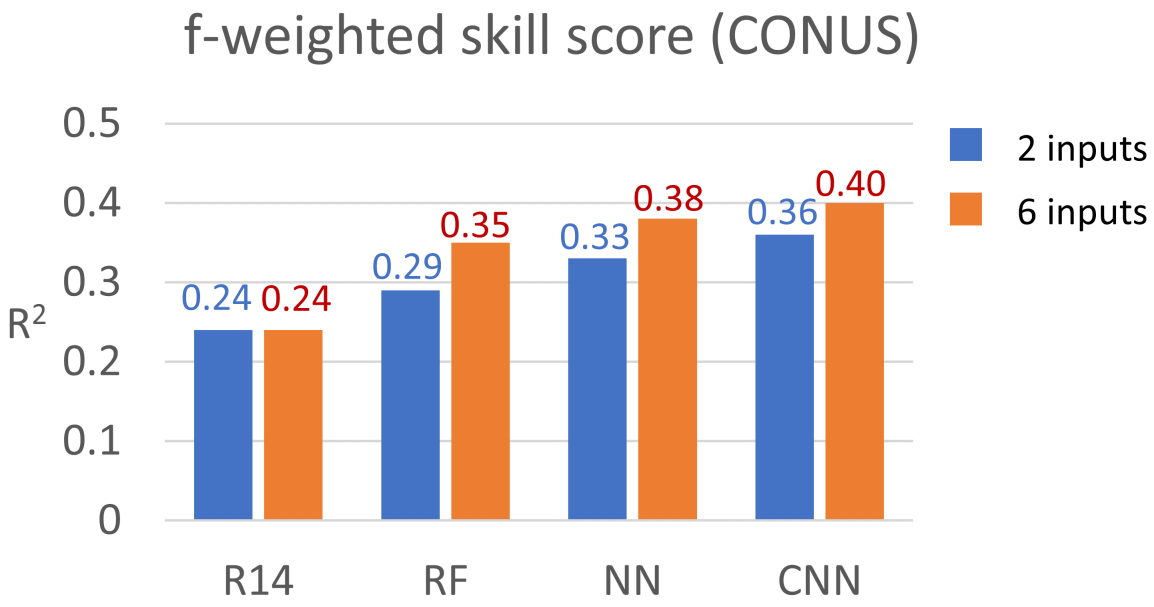

Figure 5.9: The f-weighted R^2 score for R14, RF, NN, and CNN during the testing period from 2016 - 2019. The blue bars indicate the results using only CAPE and P as inputs, and the orange bars indicate the results with four additional input variables (Z500, Z1000, Z300-700, and T2m).

Lastly, Figure 5.10 shows the scatter plots of the spatially averaged monthly lightning frequency climatology using R14 and ML-based lightning schemes (trained with all 6 input variables) against that from observations for each of four quadrants over CONUS (defined by boundaries at 99°W and 39°N). All of the lightning schemes perform well, with R^2 score values of 0.64 and higher. Figure 5.10 also shows that the ML-based lightning schemes are more accurate than R14 at capturing the monthly climatology of lightning frequency across the CONUS area. For example, it is found that R14 methods poorly represent the climatology of lightning over Southeast US, where the purple circles in Figure 5.10a are located away from the 1 to 1 line. The ML-based lightning schemes show significant improvement for this region, which is likely the main reason that the R^2 score show significant improvement for all ML-based methods. In particular, the R^2 score for CNN method is as high as 0.93, which suggests that the map-based ML lightning scheme also has the best performance at capturing the monthly climatology of lightning frequency.

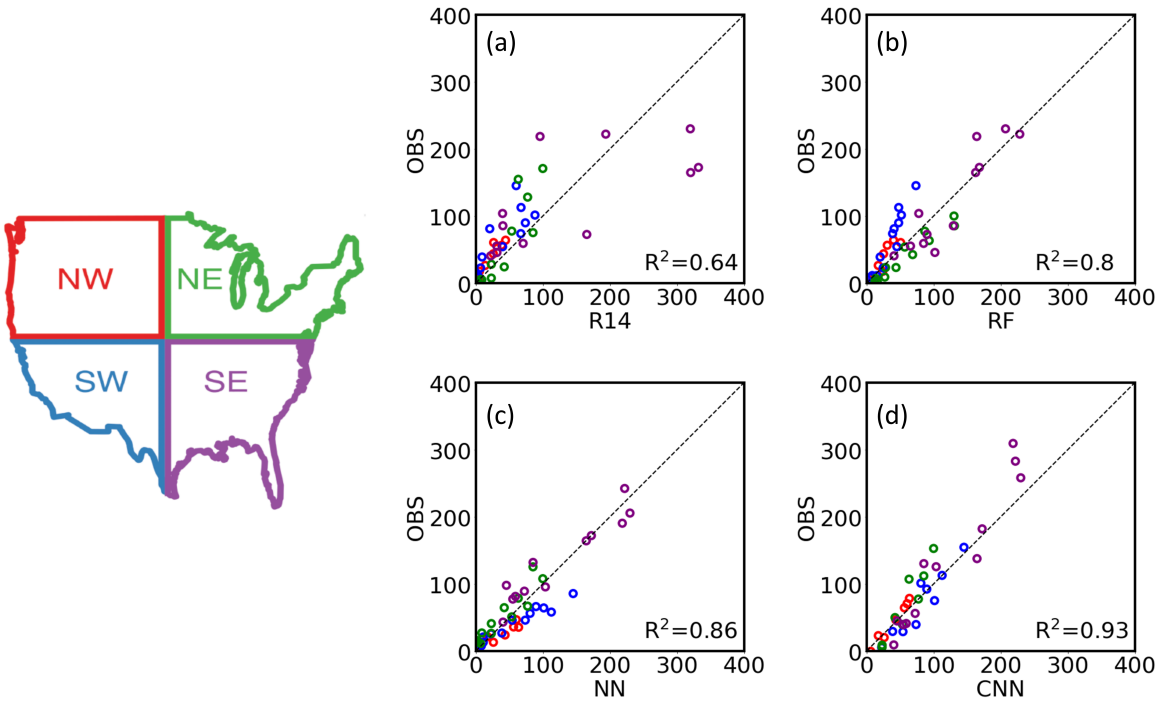

Figure 5.10: Monthly climatology of the observed lightning flash density versus the results of four lightning parameterization schemes for each of the four regions of CONUS (the four colors within each scatterplot). The four lightning paramterization schemes include a conventional lightning scheme (a; R14), and two column-based ML lightning scheme (b; RF, and c; NN), and a map-based ML lightning scheme (d; CNN). The results are obtained from 2017 to 2019. Each scatter plot has $4 \times 12 = 48$ points corresponding to a monthly climatology for each of the four regions.

5.2.3 Discussion

The results in Figure 5.8 shows that using the ML-based lightning schemes improve the accuracy of lightning diagnosis over that from the conventional lightning scheme of R14. It is worth noting that in this study, the full potential of ML methods is not yet explored as only 6 input variables are utilized. The goal of this study is to demonstrate the potential of using the ML techniques to better represent lightning frequency using large-scale variables. The results so far are promising and support the idea that ML techniques can help achieve better performance by optimizing the parameterization formula and taking advantage of the rich input data to fully capitalize on the big data generated from observations and atmospheric models.

An interesting finding from this study is that the improvement of ML-based lightning schemes is more significant over the regions where lightning is more frequent, in particular, over the Southeast US, for both daily time scale (Figure 5.8) and monthly climatology 5.10. This is likely because the ML algorithms are designed to minimize the cost function (i.e., the error), which is a measure of the difference between the predicted f and the observed f. For regions with climatologically low f, with the same fractional error, the magnitude of the error is more likely to be small, so ML algorithms will pay less attention to these smaller error. On the other hand, for regions with climatologically high f, the magnitude of the error will be larger for given fractional error, and ML algorithms will adjust the weights more quickly in the ML models to better predict f in these regions. As a result, ML-based lightning schemes are more accurate in the regions where the magnitude of f is larger. This is perhaps a favorable feature for lightning schemes, because the area with more frequent lightning may also be related to more lightning-induced hazards and therefore deserve more attention.

However, an accurate lightning representation in regions where lightning is less frequent may still be important for certain applications. For example, the "dry thunderstorms" (thunderstorms occurred with very little precipitation) over the Western US, while being

less frequent, has significant impact on the triggering of wildfire events (Westerling et al., 2006). Therefore, an accurate representation of lightning in such regions is still a desired feature for lightning schemes. To improve the performance of ML-based lightning schemes in these regions, the results in this study suggest that some modifications might be needed to prevent the ML methods to prioritize the accuracy over the lightning-rich regions. For example, a possible solution may be to train the ML-based lightning schemes separately from the lightning-rich regions, or adjust the cost function to be fractional error instead of total error during the training step. The degree to which such modifications can mitigate the issues are beyond the scope of this study, but are undoubtedly worthy of further investigation.

5.3 The lightning forecast skill using ML-based lightning parameterization schemes

In this section, I examine the lightning forecast skill by utilizing different lightning parameterization schemes, including R14, RF, NN, and CNN methods. In Chapter 2, it is discussed that an accurate lightning forecast relies on both accurate forecasts of atmospheric variables and an accurate lightning scheme. In the previous section, it is shown that the ML-based lightning schemes have the potential to represent lightning frequency more accurately. The goal in this section is to then investigate the extent to which the more accurate ML-based lightning schemes can improve the lightning forecast skill.

5.3.1 Benchmarks

In this section, the lightning forecasts are obtained by using the forecasted large-scale variables from the GEFS hindcast dataset as the inputs to the lightning schemes. The forecasted lightning frequency is then compared to the observed lightning frequency provided by WWLLN to assess the lightning forecast skill for each lightning scheme. The R14 is used as the baseline scheme in this section to evaluate the performance of the ML-based lightning scheme. In Tippett and Koshak (2018), the baseline predictability of lightning is examined using the R14 scheme, and it is found that for the CONUS-aggregated lightning frequency,

the forecast skill measured by R decreased gradually over time, starting from about 0.7 for day 1, and drops to about 0.4 after a week, and to below 0.1 after two weeks, depending on the corresponding seasons and the regions (see their Figure 2). In this study, the forecast skill is measured by the number of days it takes for R to drop below a reference level of 0.4, which gives the R14 with the CONUS-aggregated lightning forecast skill of approximately a week. It is also noted that changing this reference level does not affect the conclusions of this study significantly.

The ML-based lightning schemes are trained using the large-scale variables from the GEFS hindcast dataset for each different lead time. Following the previous section, the evaluations of the ML-based lightning schemes will be separated into two parts: the schemes that are trained using only CAPE and P, and the schemes trained using additional input variables including Ts, Tds, and w500. It is noted that the total data size is smaller than that used in the previous section, due to the shorter overlap period between the GEFS dataset and WWLLN. To ensure that the training samples and testing samples are independent and identically distributed, the 7 years of data (2010 - 2016) are randomly separated into training and testing datasets with the ratio of 5:2.

5.3.2 Performance

Since the R14 schemes are based entirely on the two variables CAPE and P, it is important to examine the predictability of CAPE and P along with the predictability of lightning. Figure 5.11 (b) and (d) show the forecast skill of P and CAPE from the GEFS hindcast dataset, which are obtained by comparing with the observed P from TRMM and CAPE from ERA5. The results show that the GEFS model has a decent forecast skill for these two variables, as the forecast skill is above 7 days for many regions over the CONUS. The figure also shows that there exists a substantial amount of spatial variability in the predictability of these two variables. For example, Figure 5.11 (b) shows that the predictability of P is higher along the west coast. This is likely because the precipitation in this region is often associated with synoptic-scale forcing, which can be better captured by the atmospheric model with a

higher forecast skill. Figure 5.11 (d) shows that CAPE has higher predictability over the Southern U.S. It is speculated that this is because the temperature and moisture profiles over this region are largely affected by the North American Monsoon in the warm season (Adams and Comrie, 1997), whose evolution may be captured by the atmospheric model. As CAPE is essentially a function of the temperature and moisture profiles, the atmospheric model can provide a better forecast skill of CAPE in this region.

Figure 5.11 (c) shows the lightning forecast skill using R14 scheme. The results show that the forecast skill is generally worse than both CAPE and P, as the forecast skill is well below 7 days in most regions over the CONUS. This result is not surprising, since it is expected that it is difficult to have an accurate lightning forecast without an accurate forecast of CAPE and P. In particular, 5.11 (c) also shows that the patterns of the forecast skill are also similar to that of CAPE and P. For example, there exist a local maximum in forecast skill over the Southern and Northwest US, corresponding to the regions with higher forecast skill of CAPE and P. In addition, the lightning forecast skill shows a local minimum over the Central US region, which is also associated with the low predictability of CAPE in this region, likely due to the difficulty in calculating CAPE in the mountainous area. The similarity between 5.11 (c) and (b), (d) suggests that the predictability of lightning frequency is limited by the predictability of CAPE and P.

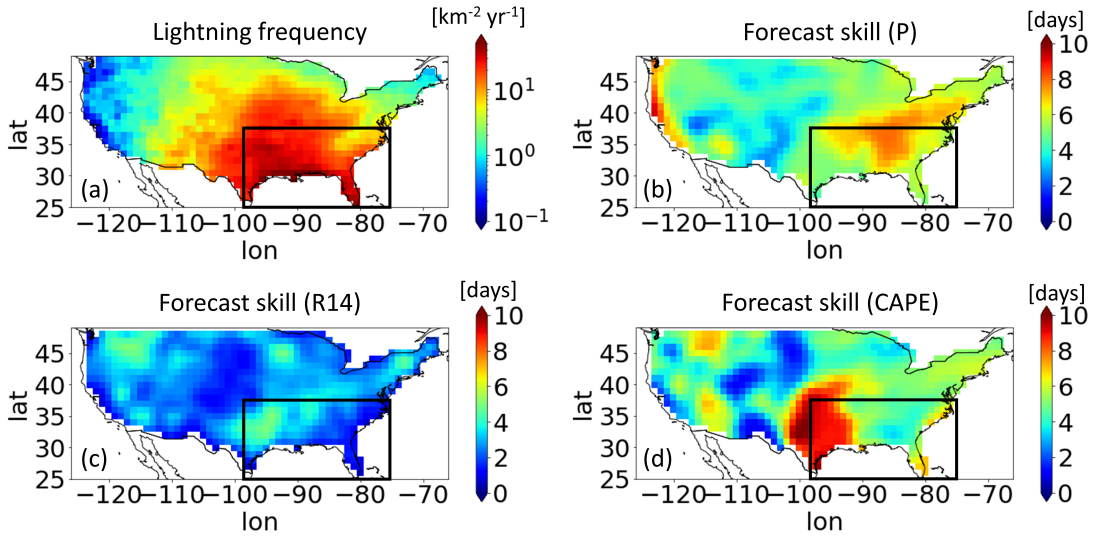

Figure 5.11: (a) The climatology of lightning frequency over CONUS area during 2010 - 2016. (b) - (d): The forecast skills map for P, f, and CAPE, respectively. The forecast skills are measured by the number of days it takes for the correlation coefficient to drop below 0.4. Gaussian smoothing is applied to (b) - (d) to reduce the noise in the figures. The domain used for the lightning forecast analysis over Southeast US is highlighted in the black box in the figures.

Figure 5.12 (a) shows the forecast skill map over the CONUS from the column-based NN method with all input variables, and the differences between the NN and R14 methods are plotted in Figure 5.12 (b). It is noted that while the NN method provides the best overall lightning forecast skill, other ML-based lightning schemes all have similar performance (not shown). The results show that the ML-based lightning scheme with NN improves the forecast skill over R14 in most regions CONUS. In the previous section, it is shown that the ML-based methods provide more accurate lightning representations, and it is shown in 5.12 (b) that the more accurate ML-based lightning can provide a higher lightning frequency forecast skill more than 1 day in most regions over CONUS. It is worth noting that the improvement over R14 is most significant over the Southeast US, corresponding to the regions where ML-based lightning schemes are most accurate. 5.12 (b) quantitatively confirms that the more accurate lightning schemes can provide a more accurate lightning forecast, with increased forecast skill by up to approximately 2 days.

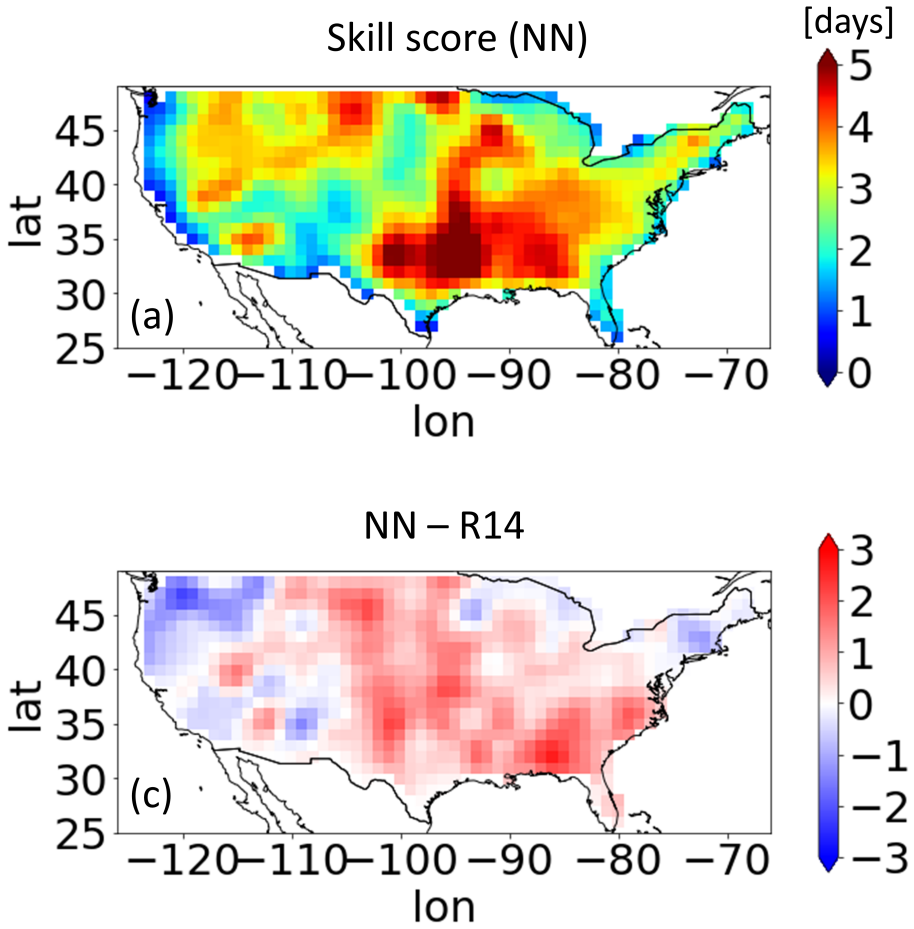

Figure 5.12: (a) The forecast skill map of f using the column-based NN lightning scheme. (b) The different between (a) and Figure 5.11 (c), as the red shadings indicate the regions where NN has a better forecast skill. A Gaussian smoothing is applied to all figures to reduce the noise in the figures.

To examine the forecast skill in more detail, I focus on the region with the most frequent lightning over the Southeast US (indicated as black boxes in Figure 5.11). Figure 5.13 shows the correlation coefficient (R) between the forecasted f from each lightning scheme and the observed f averaging over this region as a function of lead time. On the figure, the R for CAPE (blue dashed line) and P (light blue dashed line) are also plotted as references. The results show that in this region, the predictability of lightning frequency from R14 (red solid line) is generally worse than CAPE and P regardless of the lead time. It is found that, even with the same two input variables (CAPE and P), the column-based NN method can improve the forecast skill by up to two days (light green solid line), which is achieved purely by optimizing the simple formula of R14.

Next, I examine if an increasing number of input variables can further improve the lightning forecast skill. In the previous section, it is shown that the accuracy of lightning schemes can be further improved by increasing the number of input variables. However, the results in Figure 5.13 show that the lightning forecast skills do not improve significantly when the number of input variables is increased (dark green solid line for NN and brown solid line for RF). That the forecast skills of ML-based lightning schemes are not sensitive to the number of input variables can be due to several factors. First, the input variables are not the same between the GEFS hindcast dataset and that used in the previous section. In particular, the geopotential height information is not available in the GEFS dataset. The geopotential height information may be an important factor that leads to the more accurate lightning prediction in ML-based lightning schemes. Second, the ML-based lightning schemes may be sensitive to the forecast skills of the other input variables. Recall that these large-scale variables are forecasted by the GEFS model, and it is possible that some of these variables are not well-forecasted, which can ruin the lightning forecast skill of ML-based lightning schemes. Lastly, the training sample size can also be an issue, since we have a smaller training sample size from the GEFS dataset, and increasing the number of input variables may require more training samples to fully capture the patterns between these large-scale variables and lightning.

The forecast skill of CNN is examined and plotted in Figure 5.13 as the dark yellow solid line. While it is found in the previous section that the CNN has the best overall performance, it is shown in Figure 5.13 that the forecast skill of the map-based CNN method is not significantly different from the column-based methods. It is speculated that this is related to the training sample size. As the CNN with the U-net structure contains the most number of free parameters in the model, by design, it requires the most training samples to fully capture the relationship between the input variables and the output variables. Figure 5.14 shows the learning curve of RF, NN, and CNN using the reanalysis data as inputs. The figure shows that the CNN model requires more than 5 years of training data to achieve a better performance than the column-based method. The current training sample size of 5 years is limited by the short overlap between GEFS and WWLLN datasets, and it would be interesting to examine the lightning forecast skill of the map-based method once we have a larger sample size.

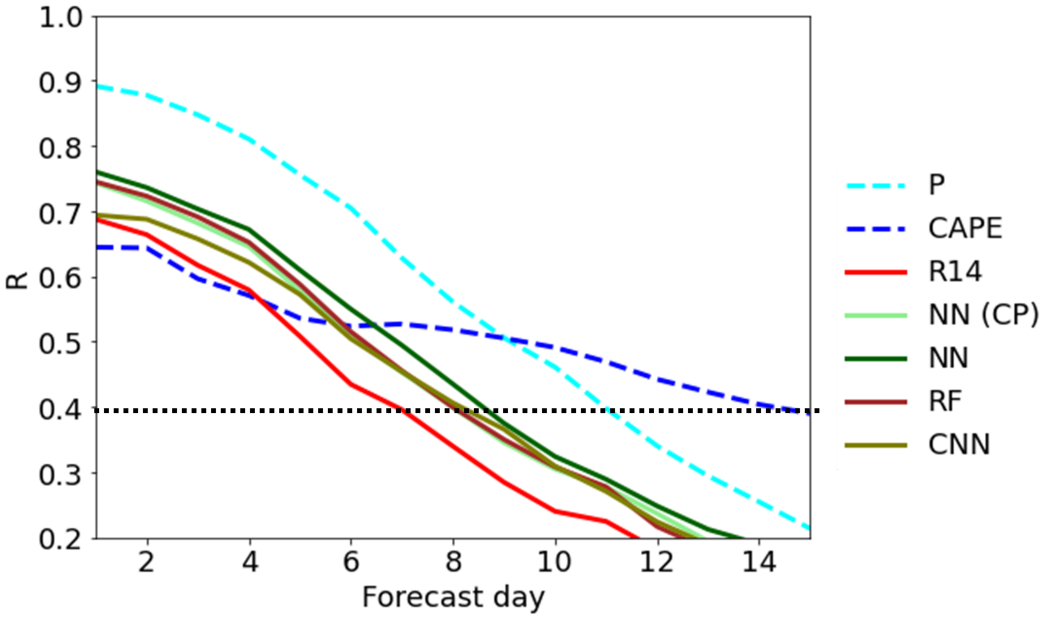

Figure 5.13: The correlation between observations and different forecasted fields as a function of lead time, including precipitation (P; lightning blue dashed line), CAPE (blue dashed line), f from R14 (red solid line), and various ML-based lightning schemes: NN (green solid line), RF (brown solid line), CNN (dark yellow solid line), and NN but with only CAPE and P as input variables (light green).

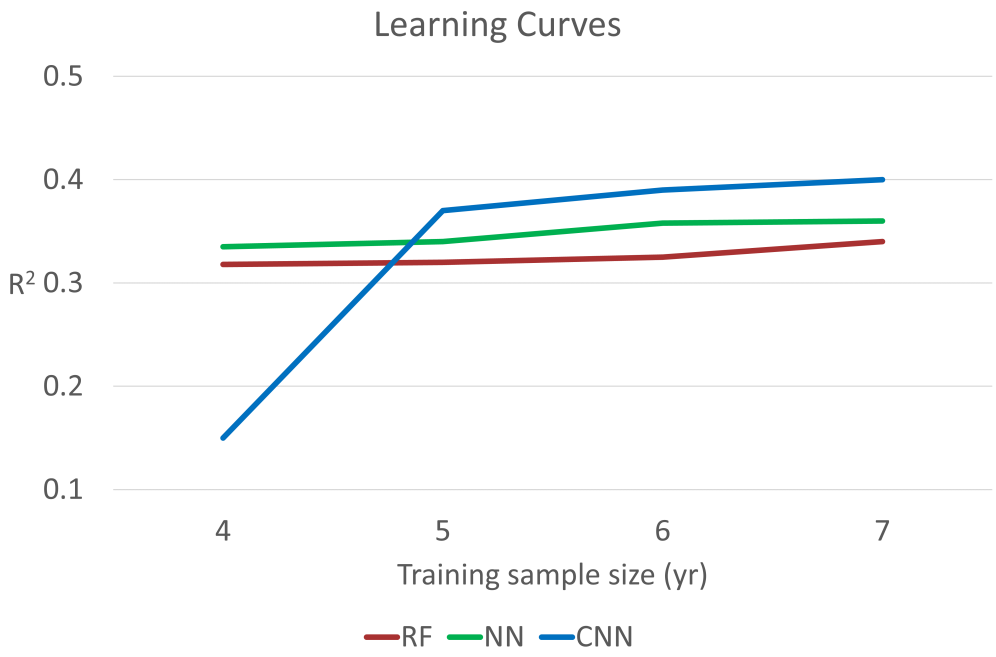

Figure 5.14: The learning curve for each ML-based lightning schemes. The schemes are trained using all observed large-scale fields listed in Table 5.1. The y-axis shows the f-weighted R^2 score, and the x-axis shows the number of samples used for training.

Lastly, it is also found that the lightning forecast skill is not uniformly distributed in different months. For the R14 scheme, the forecast correlations at short leads are noticeably lower during the warm seasons (Figure 5.15a). This result is consistent with Tippett and Koshak (2018), who attributed the lower level of skill to both the poorer forecast skill in CAPE and P, and the poorer performance of the R14 scheme during these months. The differences in the forecast correlation in different months for each ML-based lightning schemes are shown in Figure 5.15 (b) - (d). The figures show that all ML-based lightning schemes improve the forecast correlations in August-October for all lead time. This is likely, again, due to the characteristics of ML-based lightning schemes, where the ML algorithms are designed to prioritize the performance when lightning is more frequent. The results in 5.15 highlight that the ML-based lightning schemes are more skillful at forecasting lightning when lightning is more frequent, both spatially and temporally.

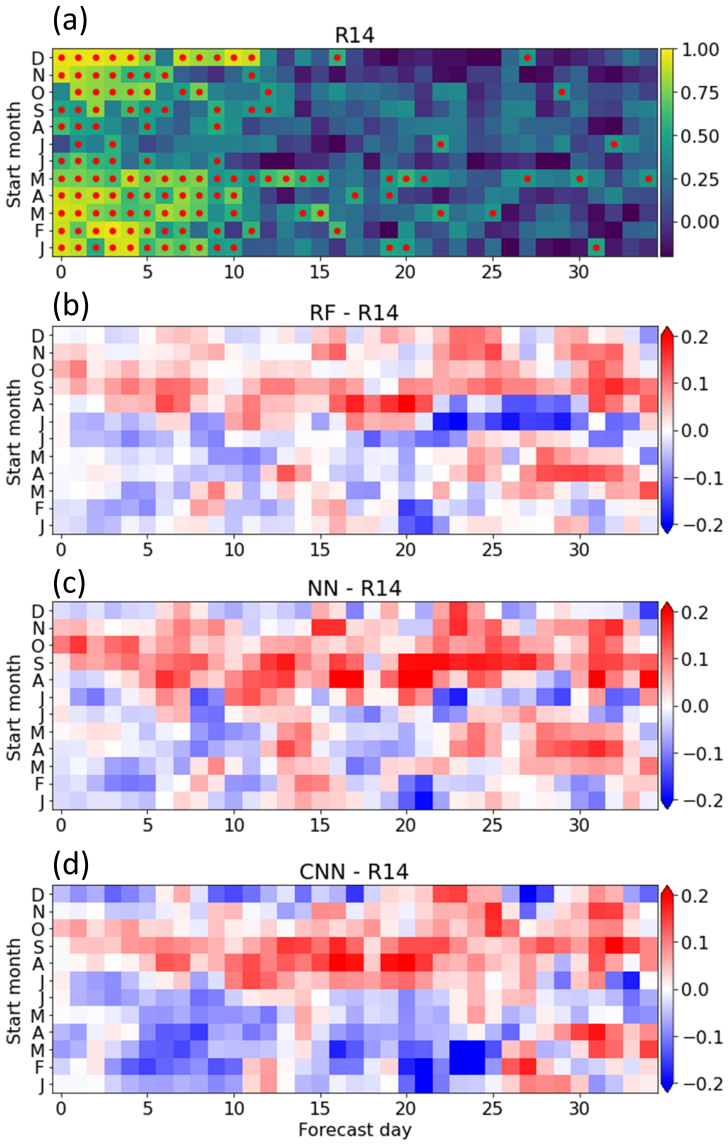

Figure 5.15: (a) The correlation (shadings) between observed f and the forecasts by using R14 scheme in different lead time and different months. (b) - (d): Same as (a), but for the difference between (b) RF, (c) NN, (d) CNN and R14.

5.3.3 Discussion

The results in this section confirm that the lightning forecast skill can be improved by using a more accurate lightning scheme. In particular, the results in Figure 5.13 show that using the ML-based lightning schemes improves the forecast skill over that of R14 by up to 2 days over the Southeast US. However, while the results in the previous section suggest that the map-based lightning scheme is more accurate, the results here show that the performance of the map-based lightning scheme is not significantly different from the column-based method, likely due to the constraints in sample size.

It is also found that, when compared to R14, the ML-based lightning schemes are more skillful in regions with more lightning, also in seasons with higher lightning frequency. This result is consistent with that in the previous section, which shows that ML-based lightning schemes are more accurate when lightning is more frequent, which has important implications for the applications of ML methods. For example, using the ML-based lightning schemes may have the advantage of guiding on preventing lightning-induced hazards, as the Southeast US accounts for the most deaths and injuries from lightning, especially in the warm seasons (Curran et al., 2000). The applications of the ML-based lightning schemes on the future projection of lightning are also worth further investigations.

Chapter 6

CONCLUSIONS

In this thesis, I have used both conventional and data-driven approaches to improve the lightning parameterization in the numerical models and the predictions of lightning. While the physical mechanisms of lightning and its relationship associated with large-scale variables are not yet fully understood, the recent advance in lightning observations, in particular, from WWLLN, have offered a new opportunity to study the physical mechanisms of lightning and to develop lightning parameterization schemes using data-driven approaches.

By using the rich lightning observations provided by WWLLN, I investigate the relationship between CAPE, precipitation, storm size, and lightning flash density (f) over the Central America region. It is found that the CAPE-f relationship is different between land and ocean: While f increases almost linearly with increasing $\text{CAPE}^{1/2}$ over the continental region, f is suppressed over the ocean when the $\text{CAPE}^{1/2}$ is smaller than a threshold-like value of approximately 15 [m s^{-1}] and increases rapidly once $\text{CAPE}^{1/2}$ exceeds this threshold value.

The CAPE-threshold feature for lightning over the ocean supports the hypothesis that the generation of lightning requires the updraft speed to exceed a certain threshold (Solomon and Baker, 1994; Williams, 1992; Zipser and Lutz, 1994). In the low-CAPE environment, since the environmental forcing is relatively weak, it is very difficult, even for large storms, to have updrafts whose speed is greater than the threshold to produce lightning. On the other hand, in the high-CAPE environment, since the environmental forcing is large, even smaller storms are capable of producing updraft speeds that are above the threshold value to produce lightning. When using the area of contiguous convective objects (CCOs) as a proxy to storm size, it is found that the storm size required for storms to produce lightning

appears to be disproportionately high in the low-CAPE regime, which further supports that the generation of lightning requires the updraft speed to exceed a certain threshold.

An accurate representation of f in the low-CAPE environment is critically important because the majority of oceanic environment is associated with CAPE below 625 [J kg^{-1}]. When using Romps et al. (2014)'s CAPE times P method in estimating the climatology of lightning frequency, it is found that their method overestimates f over the ocean (Romps et al., 2018). We argued that this is because their method produces too frequent lightning in the low-CAPE environment, where oceanic storms are often too small to produce strong updrafts to generate lightning. We showed that applying a threshold in CAPE over the ocean can significantly improve the representation of lightning climatology over the ocean. This suggests that to accurately represent the lightning frequency in lightning parameterization schemes, it is necessary to implement a CAPE-threshold in CAPE-based lightning parameterization schemes to consider the effect of storm size.

While CAPE has been considered as one of the key environmental factors for lightning (Solomon and Baker, 1998; Williams and Stanfill, 2002; Williams, 1992), the role of the storm size as a limiting factor for f has not yet drawn much attention in the lightning parameterization community. Recent studies have suggested that the spatial organization of convection may influence the lightning frequency via affecting the updraft velocity through the entrainment rate and the associated mesoscale circulation (Bang and Zipser, 2015, 2016; Mattos and Machado, 2011; Williams and Stanfill, 2002). Nevertheless, the horizontal scale of the storms is not considered in most lightning parameterization schemes. The result of this study suggested that to accurately parameterize f, it is necessary to incorporate storm size in the parameterization to accurately represent the effect of entrainment on convective updrafts.

A recent lightning parameterization scheme of Lopez (2016) attempted to incorporate the cloud base height as a proxy for the storm size. In Lopez (2016)'s parameterization, the lightning flash density is a function of CAPE, cloud ice and liquid hydrometeors content, and convective cloud base height. Lopez (2016) shows that the new lightning parameteri-

zation reasonably represents the land-sea contrast of lightning flash density and its seasonal variation when compared with the observations. However, there has not yet been a widely accepted approach to relate the convection size and the lightning frequency due to the lack of observations. The results in this study, therefore, provide the needed observational basis to relate the lightning frequency and storm size.

The lightning observations from WWLLN also provide a pathway to develop the lightning parameterization schemes via the data-driven approach by using machine learning (ML) techniques. There are two clear advantages of using ML techniques to develop lightning schemes. On one hand, because the conventional lightning parameterization schemes are designed to be human-interpretable, they often use a very simple formula which can sacrifice the performance. On the other hand, because the physical mechanisms of lightning are not yet fully understood, there are likely other important factors that are not used as inputs when using the conventional approaches. The ML-based lightning schemes can expand the input variables easily, which may help us fully capitalize on the big data generated from observations and atmospheric models. Two methods are proposed to utilize the ML techniques when developing lightning schemes. The first method is the column-based method, where the input variables are the atmospheric variables in a grid cell, and the output variable is f of the same grid cell. The second method is the map-based method, where the inputs are a set of two-dimensional maps of different atmospheric variables, and the output is the map of f.

By using the grid-scale variables obtained from satellite and reanalysis products, the performance of ML-based lightning schemes is examined and compared with R14 over the Contiguous United States (CONUS). The results show that using the ML-based lightning schemes improves the accuracy of lightning prediction over that of R14. Even with the same input variables (CAPE and P), the performance can be improved by more than 35%, showing room for improvement with the simple formula used in R14. It is also shown that the map-based ML lightning scheme of CNN can achieve better performance when compared to the column-based method. This result suggests that the large-scale weather patterns may

contain some information about the unresolved processes that are important for lightning generation. It is also found that the improvement of ML-based lightning schemes is more significant over the regions where lightning is more frequent, which is likely due to the design of the ML algorithms that will prioritize minimizing the error where the error may be the largest. As a result, the ML-based lightning schemes tend to have the better performance over the Southeast US, where lightning is most frequent over the CONUS.

As ML-based lightning schemes show promise in terms of accuracy of lightning representation, the extent to which we can improve the lightning forecast skill by using the more accurate ML-based lightning schemes is examined. The strategy used in this study for lightning forecasting is by utilizing the atmospheric model to forecast grid-scale variables, and use these variables to represent f using lightning parameterization schemes. The results show that using the more accurate ML-based lightning schemes can indeed improve the lightning forecast skill. Quantitatively, it is shown that using one of the ML-based lightning schemes improves the forecast skill over that of R14 by up to 2 days over the Southeast US, where the ML-based lightning scheme has the best performance.

That the ML-based lightning schemes provide more forecast skill over regions with more frequent lightning has important implications for the applications of ML-based lightning schemes. For example, ML-based lightning schemes may be a favorable choice for applications of using lightning forecasts to prevent lightning-induced hazards. Studies have suggested that over CONUS, most deaths and injuries caused by lightning are from regions with the most frequent lightning over the Southeast US (Curran et al., 2000). Globally, the lightning-related fatality rate is also highest in regions with most frequent lightning (e.g., countries in Africa and India, Holle (2016), 2016). A lightning scheme with higher forecast skill over these regions may be able to provide a more accurate warning earlier in time.

However, an accurate lightning representation in regions with relatively infrequent lightning may still be important. For example, the lightning over the Western US, while being less frequent, has significant impact on the triggering of wildfires (Westerling et al., 2006). In addition, while lightning is much more frequent over land than ocean, oceanic lightning

strokes still account for more than 40% total lightning globally based on WWLLN observations (Virts et al., 2013). The results of this study suggest that some caution might be needed for ML-based lightning schemes to accurately represent lightning in these regions with relatively infrequent lightning. For example, for global applications that covers both land and ocean, one may train the ML-based lightning schemes separately for land and ocean, or adjust the cost function to be fractional error instead of total error during the training step.

Finally, this study has implications for the future applications of ML techniques on the weather forecast. Recent studies show that ML models can learn the underlying physical relationships governing subgrid convection effectively and are computationally efficient once trained (Brenowitz and Bretherton, 2018; Rasp and Lerch, 2018). While challenges remain, subgrid parameterizations learned from numerical models have shown the potential to improve the weather forecast. In particular, this study has demonstrated that the ML models have the potential to improve the lightning forecast. Applications of ML on other severe weather systems such as tornadoes or hailstorms are therefore worthy of further investigation.

BIBLIOGRAPHY

Abarca, S. F., K. L. Corbosiero, and T. J. Galarneau Jr, 2010: An evaluation of the worldwide lightning location network (wwlln) using the national lightning detection network (nldn) as ground truth. *Journal of Geophysical Research: Atmospheres*, **115 (D18)**.

Abatzoglou, J. T., and A. P. Williams, 2016: Impact of anthropogenic climate change on wildfire across western us forests. *Proceedings of the National Academy of Sciences*, **113 (42)**, 11 770–11 775.

Abreu, D., D. Chandan, R. Holzworth, and K. Strong, 2010: A performance assessment of the world wide lightning location network (wwlln) via comparison with the canadian lightning detection network (cldn). *Atmospheric Measurement Techniques*, **3 (4)**, 1143–1153.

Adams, D. K., and A. C. Comrie, 1997: The north american monsoon. *Bulletin of the American Meteorological Society*, **78 (10)**, 2197–2214.

Allen, D., K. Pickering, B. Duncan, and M. Damon, 2010: Impact of lightning no emissions on north american photochemistry as determined using the global modeling initiative (gmi) model. *Journal of Geophysical Research: Atmospheres*, **115 (D22)**.

Allen, D., K. Pickering, R. Pinder, B. Henderson, K. Appel, and A. Prados, 2012: Impact of lightning-no on eastern united states photochemistry during the summer of 2006 as determined using the cmaq model. *Atmospheric Chemistry and Physics*, **12 (4)**, 1737–1758.

Allen, D. J., and K. E. Pickering, 2002: Evaluation of lightning flash rate parameterizations for use in a global chemical transport model. *Journal of Geophysical Research: Atmospheres*, **107 (D23)**, 1–21, doi:10.1029/2002JD002066.

Asakawa, H., G. Sazaki, K. Nagashima, S. Nakatsubo, and Y. Furukawa, 2016: Two types of quasi-liquid layers on ice crystals are formed kinetically. *Proceedings of the National Academy of Sciences*, **113 (7)**, 1749–1753.

Baker, M., and J. Dash, 1994: Mechanism of charge transfer between colliding ice particles in thunderstorms. *Journal of Geophysical Research: Atmospheres*, **99 (D5)**, 10 621–10 626.

Baldi, P., 2012: Autoencoders, unsupervised learning, and deep architectures. *Proceedings of ICML workshop on unsupervised and transfer learning*, JMLR Workshop and Conference Proceedings, 37–49.

Bang, S. D., and E. J. Zipser, 2015: Differences in size spectra of electrified storms over land and ocean. *Geophysical Research Letters*, **42 (16)**, 6844–6851, doi:10.1002/2015GL065264.

Bang, S. D., and E. J. Zipser, 2016: Seeking reasons for the differences in size spectra of electrified storms over land and ocean. *Journal of Geophysical Research: Atmospheres*, **121 (15)**, 9048–9068.

Bedka, K. M., and K. Khlopenkov, 2016: A probabilistic multispectral pattern recognition method for detection of overshooting cloud tops using passive satellite imager observations. *Journal of Applied Meteorology and Climatology*, **55 (9)**, 1983–2005.

Belochitski, A., P. Binev, R. DeVore, M. Fox-Rabinovitz, V. Krasnopolsky, and P. Lamby, 2011: Tree approximation of the long wave radiation parameterization in the ncar cam global climate model. *Journal of Computational and Applied Mathematics*, **236 (4)**, 447–460.

Betz, H. D., K. Schmidt, and W. P. Oettinger, 2009: Linet–an international vlf/lf lightning detection network in europe. *Lightning: principles, instruments and applications*, Springer, 115–140.

Boccippio, D. J., 2002: Lightning scaling relations revisited. *Journal of the Atmospheric Sciences*, **59 (6)**, 1086–1104, doi:10.1175/1520-0469(2002)059⟨1086:LSRR⟩2.0.CO;2.

Brenowitz, N. D., and C. S. Bretherton, 2018: Prognostic Validation of a Neural Network Unified Physics Parameterization. *Geophysical Research Letters*, **45 (12)**, 6289–6298, doi: 10.1029/2018GL078510.

Brooks, C., 1925: The distribution of thunderstorms over the globe. *Geophys. Mem. London*, **24**, 147 – 164.

Bürgesser, R. E., 2017: Assessment of the world wide lightning location network (wwlln) detection efficiency by comparison to the lightning imaging sensor (lis). *Quarterly Journal of the Royal Meteorological Society*, **143 (708)**, 2809–2817.

Burrows, W. R., P. King, P. J. Lewis, B. Kochtubajda, B. Snyder, and V. Turcotte, 2002: Lightning occurrence patterns over canada and adjacent united states from lightning detection network observations. *Atmosphere-ocean*, **40 (1)**, 59–80.

Cardoso, I., O. Pinto Jr, I. Pinto, and R. Holle, 2011: A new approach to estimate the annual number of global lightning fatalities. *Preprints, 14th Int. Conf. on Atmospheric Electricity, Rio de Janeiro, Brazil, IUGG/IAMAS International Commission on Atmospheric Electricity*, Vol. 4.

Cecil, D. J., D. E. Buechler, and R. J. Blakeslee, 2014: Gridded lightning climatology from TRMM-LIS and OTD: Dataset description. *Atmospheric Research*, **135-136**, 404–414, doi: 10.1016/j.atmosres.2012.06.028, URL http://dx.doi.org/10.1016/j.atmosres.2012.06.028.

Christian, H. J., and Coauthors, 2003: Global frequency and distribution of lightning as observed from space by the Optical Transient Detector. *Jounal of Geophysical Research*, **108**, doi:10.1029/2002JD002347.

Clark, A. J., W. A. Gallus Jr, M. Xue, and F. Kong, 2009: A comparison of precipitation forecast skill between small convection-allowing and large convection-parameterizing ensembles. *Weather and forecasting*, **24 (4)**, 1121–1140.

Clark, S. K., D. S. Ward, and N. M. Mahowald, 2017: Parameterization-based uncertainty in future lightning flash density. *Geophysical Research Letters*, **44 (6)**, 2893–2901, doi: 10.1002/2017GL073017.

Cooper, O. R., and Coauthors, 2007: Evidence for a recurring eastern north america upper tropospheric ozone maximum during summer. *Journal of Geophysical Research: Atmospheres*, **112 (D23)**.

Cummins, K. L., and M. J. Murphy, 2009: An overview of lightning locating systems: History, techniques, and data uses, with an in-depth look at the us nldn. *IEEE transactions on electromagnetic compatibility*, **51 (3)**, 499–518.

Curran, E. B., R. L. Holle, and R. E. Lopez, 2000: Lightning casualties and damages in the United States from 1959 to 1994. *Journal of Climate*, **13 (19)**, 3448–3464, doi:10.1175/1520-0442(2000)013⟨3448:LCADIT⟩2.0.CO;2.

Dahl, J. M., H. Höller, and U. Schumann, 2011: Modeling the flash rate of thunderstorms. part i: Framework. *Monthly weather review*, **139 (10)**, 3093–3111.

DeCaria, A. J., K. E. Pickering, G. L. Stenchikov, and L. E. Ott, 2005: Lightning-generated nox and its impact on tropospheric ozone production: A three-dimensional modeling study of a stratosphere-troposphere experiment: Radiation, aerosols and ozone (sterao-a) thunderstorm. *Journal of Geophysical Research: Atmospheres*, **110 (D14)**.

Deierling, W., and W. A. Petersen, 2008: Total lightning activity as an indicator of updraft characteristics. *Journal of Geophysical Research Atmospheres*, **113 (16)**, doi: 10.1029/2007JD009598.

Deierling, W., W. A. Petersen, J. Latham, S. Ellis, and H. J. Christian, 2008: The relationship between lightning activity and ice fluxes in thunderstorms. *Journal of Geophysical Research Atmospheres*, **113 (15)**, 1–20, doi:10.1029/2007JD009700.

Dewan, A., E. T. Ongee, M. Rafiuddin, M. M. Rahman, and R. Mahmood, 2018: Lightning activity associated with precipitation and CAPE over Bangladesh. *International Journal of Climatology*, **38 (4)**, 1649–1660, doi:10.1002/joc.5286.

Finney, D. L., R. M. Doherty, O. Wild, H. Huntrieser, H. C. Pumphrey, and A. M. Blyth, 2014: Using cloud ice flux to parametrise large-scale lightning. *Atmospheric Chemistry and Physics*, **14 (23)**, 12 665–12 682, doi:10.5194/acp-14-12665-2014.

Fuchs, B. R., and Coauthors, 2015: Environmental controls on storm intensity and charge structure in multiple regions of the continental United States. *Journal of Geophysical Research*, **120 (13)**, 6575–6596, doi:10.1002/2015JD023271.

Garolera, A. C., S. F. Madsen, M. Nissim, J. D. Myers, and J. Holboell, 2014: Lightning damage to wind turbine blades from wind farms in the us. *IEEE Transactions on Power Delivery*, **31 (3)**, 1043–1049.

Gordillo-Vázquez, F. J., F. J. Pérez-Invernón, H. Huntrieser, and A. K. Smith, 2019: Comparison of Six Lightning Parameterizations in CAM5 and the Impact on Global Atmospheric Chemistry. *Earth and Space Science*, **6 (12)**, 2317–2346, doi:10.1029/2019EA000873.

Goudsblom, J., 1992: *Fire and civilization*. Viking Adult.

Grewe, V., D. Brunner, M. Dameris, J. L. Grenfell, R. Hein, D. Shindell, and J. Staehelin, 2001: Origin and variability of upper tropospheric nitrogen oxides and ozone at northern mid-latitudes. *Atmospheric Environment*, **35 (20)**, 3421–3433, doi:10.1016/S1352-2310(01)00134-0.

Groenemeijer, P., T. Púčik, I. Tsonevsky, and P. Bechtold, 2019: An overview of convective available potential energy and convective inhibition provided by nwp models for operational forecasting. *ECMWF Technical Memoranda*, 1–19.

Ham, Y.-G., J.-H. Kim, and J.-J. Luo, 2019: Deep learning for multi-year enso forecasts. *Nature*, **573 (7775)**, 568–572.

Hauglustaine, D., C. Granier, G. Brasseur, and G. Mégie, 1994: Impact of present aircraft emissions of nitrogen oxides on tropospheric ozone and climate forcing. *Geophysical research letters*, **21 (18)**, 2031–2034.

He, Y., B. Gu, D. Zhang, W. Lu, C. W. Yu, and Z. Gu, 2018: Towards the understanding of ice crystal-graupel collision charging in thunderstorm electrification. *Preprints*, doi: 10.20944/preprints201811.0320.v1.

Hersbach, H., and Coauthors, 2020: The ERA5 global reanalysis. *Quarterly Journal of the Royal Meteorological Society*, **146 (730)**, 1999–2049, doi:10.1002/qj.3803.

Holle, R. L., 2016: The number of documented global lightning fatalities. *International Conference on Lightning Protection (ICLP 2016)*, 1–4.

Holle, R. L., and R. E. Lopez, 2003: A comparison of current lightning death rates in the US with other locations and times. *International Conference on Lightning and Static Electricity*, 16 – 18.

Holton, J. R., 2004: *An introduction to dynamic meteorology*. 4th ed., Academic Press.

Holzworth, R., M. McCarthy, J. Brundell, A. Jacobson, and C. Rodger, 2019: Global Distribution of Superbolts. *Journal of Geophysical Research: Atmospheres*, doi:10.1029/2019jd030975.

Hudman, R. C., and Coauthors, 2007: Surface and lightning sources of nitrogen oxides over the united states: Magnitudes, chemical evolution, and outflow. *Journal of Geophysical Research: Atmospheres*, **112 (D12)**.

Huffman, G. J., and Coauthors, 2007: The TRMM Multisatellite Precipitation Analysis

(TMPA): Quasi-global, multiyear, combined-sensor precipitation estimates at fine scales. *Journal of Hydrometeorology*, **8 (1)**, 38–55, doi:10.1175/JHM560.1.

Hutchins, M. L., R. H. Holzworth, C. J. Rodger, and J. B. Brundell, 2012: Far-Field power of lightning strokes as measured by the world wide lightning location network. *Journal of Atmospheric and Oceanic Technology*, **29 (8)**, 1102–1110, doi:10.1175/JTECH-D-11-00174.1.

Hutchins, M. L., R. H. Holzworth, K. S. Virts, J. M. Wallace, and S. Heckman, 2013: Radiated VLF energy differences of land and oceanic lightning. *Geophysical Research Letters*, **40 (10)**, 2390–2394, doi:10.1002/grl.50406.

Jaegle, L., D. J. Jacob, Y. Wang, A. J. Weinheimer, B. A. Ridley, T. L. Campos, G. W. Sachse, and D. E. Hagen, 1998: Sources and chemistry of nox in the upper troposphere over the united states. *Geophysical Research Letters*, **25 (10)**, 1705–1708.

Jaeglé, L., L. Steinberger, R. V. Martin, and K. Chance, 2005: Global partitioning of no x sources using satellite observations: Relative roles of fossil fuel combustion, biomass burning and soil emissions. *Faraday discussions*, **130**, 407–423.

Jayaratne, E., and C. Saunders, 1984: The "rain gush", lightning, and the lower positive charge center in thunderstorms. *Journal of Geophysical Research: Atmospheres*, **89 (D7)**, 11 816–11 818.

Jayaratne, E. R., C. P. Saunders, and J. Hallett, 1983: Laboratory studies of the charging of soft-hail during ice crystal interactions. *Quarterly Journal of the Royal Meteorological Society*, **109 (461)**, 609–630, doi:10.1002/qj.49710946111.

Kanata, J., A. Ametani, and K. Yamamoto, 2012: Threats of lightning current through an electric vehicle. *2012 International Conference on Lightning Protection (ICLP)*, IEEE, 1–6.

Knapp, K. R., and S. L. Wilkins, 2018: Gridded Satellite (GridSat) GOES and CONUS data. *Earth System Science Data*, **10 (3)**, 1417–1425, doi:10.5194/essd-10-1417-2018.

Koren, I., Y. J. Kaufman, D. Rosenfeld, L. A. Remer, and Y. Rudich, 2005: Aerosol invigoration and restructuring of atlantic convective clouds. *Geophysical Research Letters*, **32 (14)**.

Krause, A., S. Kloster, S. Wilkenskjeld, and H. Paeth, 2014: The sensitivity of global wildfires to simulated past, present, and future lightning frequency. *Journal of Geophysical Research: Biogeosciences*, **119 (3)**, 312–322.

Labrador, L. J., R. von Kuhlmann, and M. G. Lawrence, 2004: Strong sensitivity of the global mean oh concentration and the tropospheric oxidizing efficiency to the source of nox from lightning. *Geophysical research letters*, **31 (6)**.

Lamarque, J.-F., G. Brasseur, P. Hess, and J.-F. Müller, 1996: Three-dimensional study of the relative contributions of the different nitrogen sources in the troposphere. *Journal of Geophysical Research: Atmospheres*, **101 (D17)**, 22 955–22 968.

Larraondo, P. R., L. J. Renzullo, I. Inza, and J. A. Lozano, 2019: A data-driven approach to precipitation parameterizations using convolutional encoder-decoder neural networks. *arXiv preprint arXiv:1903.10274*.

Latham, D., and E. Williams, 2001: Lightning and forest fires. *Forest Fires*, Elsevier, 375–418.

Lewis, E., R. Harvey, and J. Rasmussen, 1960: Hyperbolic direction finding with sferics of transatlantic origin. *Journal of Geophysical Research*, **65 (7)**, 1879–1905.

Liaskos, C. E., D. J. Allen, and K. E. Pickering, 2015: Sensitivity of tropical tropospheric composition to lightning nox production as determined by replay simulations with geos-5. *Journal of Geophysical Research: Atmospheres*, **120 (16)**, 8512–8534.

Ling, J., A. Kurzawski, and J. Templeton, 2016: Reynolds averaged turbulence modelling using deep neural networks with embedded invariance. *Journal of Fluid Mechanics*, **807**, 155–166.

Liu, C., E. R. Williams, E. J. Zipser, and G. Burns, 2010: Diurnal variations of global thunderstorms and electrified shower clouds and their contribution to the global electrical circuit. *Journal of the Atmospheric Sciences*, **67 (2)**, 309–323, doi:10.1175/2009JAS3248.1.

Lopez, P., 2016: A Lightning Parameterization for the ECMWF Integrated Forecasting System. *Monthly Weather Review*, **144 (9)**, 3057–3075, doi:10.1175/mwr-d-16-0026.1.

Lucas, C., E. J. Zipser, and M. A. LeMone, 1994: Vertical velocity in oceanic convection off tropical Australia. *Journal of Atmospheric Sience*, **51 (21)**, 3183–3194.

MacGorman, D. R., W. D. Rust, and W. D. Rust, 1998: *The electrical nature of storms*. Oxford University Press on Demand.

Mach, D. M., R. J. Blakeslee, and M. G. Bateman, 2011: Global electric circuit implications of combined aircraft storm electric current measurements and satellite-based diurnal lightning statistics. *Journal of Geophysical Research: Atmospheres*, **116 (D5)**.

Mach, D. M., R. J. Blakeslee, M. G. Bateman, and J. C. Bailey, 2010: Comparisons of total currents based on storm location, polarity, and flash rates derived from high-altitude aircraft overflights. *Journal of Geophysical Research: Atmospheres*, **115 (D3)**.

Mallet, V., G. Stoltz, and B. Mauricette, 2009: Ozone ensemble forecast with machine learning algorithms. *Journal of Geophysical Research: Atmospheres*, **114 (D5)**.

Marion, G., R. J. Trapp, and S. W. Nesbitt, 2019: Using overshooting top area to discriminate potential for large, intense tornadoes. *Geophysical Research Letters*, **46 (21)**, 12 520–12 526.

Markowski, P., and Y. Richardson, 2011: *Mesoscale meteorology in midlatitudes*, Vol. 2. John Wiley & Sons.

Martin, R. V., B. Sauvage, I. Folkins, C. E. Sioris, C. Boone, P. Bernath, and J. Ziemke, 2007: Space-based constraints on the production of nitric oxide by lightning. *Journal of Geophysical Research: Atmospheres*, **112 (D9)**.

Mattos, E. V., and L. A. Machado, 2011: Cloud-to-ground lightning and Mesoscale Convective Systems. *Atmospheric Research*, **99 (3-4)**, 377–390, doi:10.1016/j.atmosres.2010.11.007, URL http://dx.doi.org/10.1016/j.atmosres.2010.11.007.

McCaul, E. W., S. J. Goodman, K. M. LaCasse, and D. J. Cecil, 2009: Forecasting lightning threat using cloud-resolving model simulations. *Weather and Forecasting*, **24 (3)**, 709–729, doi:10.1175/2008WAF2222152.1.

Meijer, E. W., P. F. Van Velthoven, D. W. Brunner, H. Huntrieser, and H. Kelder, 2001: Improvement and evaluation of the parameterisation of nitrogen oxide production by lightning. *Physics and Chemistry of the Earth, Part C: Solar, Terrestrial and Planetary Science*, **26 (8)**, 577–583, doi:10.1016/S1464-1917(01)00050-2.

Michalon, N., A. Nassif, T. Saouri, J. F. Royer, and C. A. Pontikis, 1999: Contribution to the climatological study of lightning. *Geophysical Research Letters*, **26 (20)**, 3097–3100, doi:10.1029/1999GL010837.

Montanyà, J., O. Van Der Velde, and E. R. Williams, 2014: Lightning discharges produced by wind turbines. *Journal of Geophysical Research: Atmospheres*, **119 (3)**, 1455–1462.

Mostajabi, A., D. L. Finney, M. Rubinstein, and F. Rachidi, 2019: Nowcasting lightning occurrence from commonly available meteorological parameters using machine learning techniques. *npj Climate and Atmospheric Science*, **2 (1)**, 1–15, doi:10.1038/s41612-019-0098-0, URL http://dx.doi.org/10.1038/s41612-019-0098-0.

Murray, L. T., J. A. Logan, and D. J. Jacob, 2013: Interannual variability in tropical tropospheric ozone and oh: The role of lightning. *Journal of Geophysical Research: Atmospheres*, **118 (19)**, 11–468.

Murugavel, P., S. D. Pawar, and V. Gopalakrishan, 2014: Climatology of lightning over Indian region and its relationship with convective available potential energy. *International Journal of Climatology*, **34 (11)**, 3179–3187, doi:10.1002/joc.3901.

Naccarato, K., and O. Pinto Jr, 2009: Improvements in the detection efficiency model for the brazilian lightning detection network (brasildat). *Atmospheric Research*, **91 (2-4)**, 546–563.

Norinder, H., 1953: Long distance location of thunderstorms. *Thunderstorm electricity*, 276–327.

Orville, R. E., 2008: Development of the national lightning detection network. *Bulletin of the American Meteorological Society*, **89 (2)**, 180–190.

Pawar, S. D., D. M. Lal, and P. Murugavel, 2012: Lightning characteristics over central India during Indian summer monsoon. *Atmospheric Research*, **106**, 44–49, doi:10.1016/j.atmosres.2011.11.007, URL http://dx.doi.org/10.1016/j.atmosres.2011.11.007.

Petersen, W. A., H. J. Christian, and S. A. Rutledge, 2005: TRMM observations of the global relationship between ice water content and lightning. *Geophysical Research Letters*, **32 (14)**, 1–4, doi:10.1029/2005GL023236.

Petersen, W. A., S. A. Rutledge, and R. E. Orville, 1996: Cloud-to-ground lightning observations from TOGA COARE: Selected results and lightning location algorithms. *Monthly Weather Review*, **124 (4)**, 602–620, doi:10.1175/1520-0493(1996)124⟨0602:CTGLOF⟩2.0.CO;2.

Petersen, W. A., S. A. Rutledge, and U. States, 1998: On the relationship between cloud-to-ground lightning and convective rainfall temporal and spatial scales and 104-105 of

the rain yield clustered near l0 s kg / fl for a large portion of the midcontinental yields were slightly lower over the arid southwes. *Journal of Geophysical Research*, **103 (97)**, 14 025–14 040.

Pickering, K. E., A. M. Thompson, R. R. Dickerson, W. T. Luke, D. P. McNamara, J. P. Greenberg, and P. R. Zimmerman, 1990: Model calculations of tropospheric ozone production potential following observed convective events. *Journal of Geophysical Research: Atmospheres*, **95 (D9)**, 14 049–14 062.

Pickering, K. E., Y. Wang, W.-K. Tao, C. Price, and J.-F. Müller, 1998: Vertical distributions of lightning nox for use in regional and global chemical transport models. *Journal of Geophysical Research: Atmospheres*, **103 (D23)**, 31 203–31 216.

Poelman, D. R., W. Schulz, G. Diendorfer, and M. Bernardi, 2016: The european lightning location system euclid–part 2: Observations. *Natural Hazards and Earth System Sciences*, **16 (2)**, 607–616.

Price, C., and D. Rind, 1992: A simple lightning parameterization for calculating global lightning distribution. *Journal of Geophysical Research*, **97 (92)**, 9919–9933.

Rasp, S., and S. Lerch, 2018: Neural networks for postprocessing ensemble weather forecasts. *Monthly Weather Review*, **146 (11)**, 3885–3900.

Riahi, K., and Coauthors, 2011: Rcp 8.5—a scenario of comparatively high greenhouse gas emissions. *Climatic change*, **109 (1)**, 33–57.

Rodger, C. J., S. Werner, J. B. Brundell, E. H. Lay, N. R. Thomson, R. H. Holzworth, and R. L. Dowden, 2006: Detection efficiency of the VLF World-Wide Lightning Location Network (WWLLN): Initial case study. *Annales Geophysicae*, **24 (12)**, 3197–3214, doi: 10.5194/angeo-24-3197-2006.

Romps, D. M., 2019: Evaluating the Future of Lightning in Cloud-Resolving Models. *Geophysical Research Letters*, **46 (24)**, 14 863–14 871, doi:10.1029/2019GL085748.

Romps, D. M., A. B. Charn, R. H. Holzworth, W. E. Lawrence, J. Molinari, and D. Vollaro, 2018: CAPE Times P Explains Lightning Over Land But Not the Land-Ocean Contrast. *Geophysical Research Letters*, **45 (22)**, 12,623–12,630, doi:10.1029/2018GL080267.

Romps, D. M., J. T. Seeley, D. Vollaro, and J. Molinari, 2014: Projected increase in lightning strikes in the united states due to global warming. *Science*, **346 (6211)**, 851–854, doi: 10.1126/science.1259100.

Ronneberger, O., P. Fischer, and T. Brox, 2015: U-net: Convolutional networks for biomedical image segmentation. *International Conference on Medical image computing and computer-assisted intervention*, Springer, 234–241.

Rudlosky, S. D., and D. T. Shea, 2013: Evaluating wwlln performance relative to trmm/lis. *Geophysical Research Letters*, **40 (10)**, 2344–2348.

Rutledge, S. A., E. R. Williams, and T. D. Keenan, 1992: The Down Under Doppler and Electricity Experiment (DUNDEE): overview and preliminary results. *Bulletin - American Meteorological Society*, **73 (1)**, 3–16, doi:10.1175/1520-0477(1992)073⟨0003:tdudae⟩2.0.co; 2.

Sauvage, B., and Coauthors, 2007: Remote sensed and in situ constraints on processes affecting tropical tropospheric ozone. *Atmospheric Chemistry and Physics*, **7 (3)**, 815–838.

Schulz, W., G. Diendorfer, S. Pedeboy, and D. R. Poelman, 2016: The european lightning location system euclid–part 1: Performance analysis and validation. *Natural Hazards and Earth System Sciences*, **16 (2)**, 595–605.

Shohag, M. A. S., E. C. Hammel, D. O. Olawale, and O. I. Okoli, 2017: Damage mitigation techniques in wind turbine blades: A review. *Wind Engineering*, **41 (3)**, 185–210.

Solomon, R., and M. Baker, 1994: Electrification of new mexico thunderstorms. *Monthly weather review*, **122 (8)**, 1878–1886.

Solomon, R., and M. Baker, 1998: Lightning flash rate and type in convective storms. *Journal of Geophysical Research Atmospheres*, **103 (D12)**, 14 041–14 057, doi:10.1029/97JD03323.

Stolz, D. C., S. A. Rutledge, and J. R. Pierce, 2015: Simultaneous influences of thermodynamics and aerosols on deep convection and lightning in the tropics. *Journal of Geophysical Research: Atmospheres*, **120 (12)**, 6207–6231.

Stolz, D. C., S. A. Rutledge, J. R. Pierce, and S. C. Van Den Heever, 2017: A global lightning parameterization based on statistical relationships among environmental factors, aerosols, and convective clouds in the TRMM climatology. *Journal of Geophysical Research*, **122 (14)**, 7461–7492, doi:10.1002/2016JD026220.

Stolzenburg, M., W. D. Rust, and T. C. Marshall, 1998: Electrical structure in thunderstorm convective regions 2. Isolated storms. *Journal of Geophysical Research Atmospheres*, **103 (D12)**, 14 079–14 096, doi:10.1029/97JD03547.

Sugita, A., and M. Matsui, 2012: Lightning characteristics in japan observed by the jldn from 2001 to 2010. *22nd International Lightning Detection Conference, Broomfield, Colorado*, 2–3.

Takahashi, T., 1978: Riming Electrification as a Charge Generation Mechanism in Thunderstorms. *Journal of the Atmospheric Science*, **35**, 1536 – 1548.

Talukdar, S., M. Venkat Ratnam, V. Ravikiran, and R. Chakraborty, 2019: Influence of Black Carbon Aerosol on the Atmospheric Instability. *Journal of Geophysical Research: Atmospheres*, **124 (10)**, 5539–5554, doi:10.1029/2018JD029611.

Tapia, A., J. A. Smith, and M. Dixon, 1998: Estimation of convective rainfall from lightning observations. *Journal of Applied Meteorology*, **37 (11)**, 1497–1509, doi:10.1175/1520-0450(1998)037⟨1497:eocrfl⟩2.0.co;2.

Thomson, A. M., and Coauthors, 2011: Rcp4. 5: a pathway for stabilization of radiative forcing by 2100. *Climatic change*, **109 (1)**, 77–94.

Thornton, J. A., K. S. Virts, R. H. Holzworth, and T. P. Mitchell, 2017: Lightning enhancement over major oceanic shipping lanes. *Geophysical Research Letters*, **44 (17)**, 9102–9111.

Tippett, M. K., and W. J. Koshak, 2018: A Baseline for the Predictability of U.S. Cloud-to-Ground Lightning. *Geophysical Research Letters*, **45 (19)**, 10,719–10,728, doi:10.1029/2018GL079750.

Tippett, M. K., C. Lepore, W. J. Koshak, T. Chronis, and B. Vant-Hull, 2018: Performance of a simple proxy for us cloud-to-ground lightning. *arXiv preprint arXiv:1810.00930*.

Tippett, M. K., C. Lepore, W. J. Koshak, T. Chronis, and B. Vant-Hull, 2019: Performance of a simple reanalysis proxy for U.S. cloud-to-ground lightning. *International Journal of Climatology*, **39 (10)**, 3932–3946, doi:10.1002/joc.6049.

Tobin, I., S. Bony, C. E. Holloway, J.-Y. Grandpeix, G. Sèze, D. Coppin, S. J. Woolnough, and R. Emy Roca, 2013: Does convective aggregation need to be represented in cumulus parameterizations? *Journal of Advances in Modeling Earth Systems*, **5**, 692–703, doi:10.1002/jame.20047.

Tobin, I., S. Bony, and R. Roca, 2012: Observational evidence for relationships between the degree of aggregation of deep convection, water vapor, surface fluxes, and radiation. *Journal of Climate*, **25 (20)**, 6885–6904, doi:10.1175/JCLI-D-11-00258.1.

Trapp, R. J., G. R. Marion, and S. W. Nesbitt, 2017: The regulation of tornado intensity by updraft width. *Journal of the Atmospheric Sciences*, **74 (12)**, 4199–4211.

Turner, A. J., I. Fung, V. Naik, L. W. Horowitz, and R. C. Cohen, 2018: Modulation of hydroxyl variability by enso in the absence of external forcing. *Proceedings of the National Academy of Sciences*, **115 (36)**, 8931–8936.

Ukkonen, P., and A. Mäkelä, 2019: Evaluation of Machine Learning Classifiers for Predicting Deep Convection. *Journal of Advances in Modeling Earth Systems*, doi:10.1029/2018MS001561.

Uman, M., and V. Rakov, 2003: The interaction of lightning with airborne vehicles. *Progress in Aerospace Sciences*, **39 (1)**, 61–81.

Ushio, T., S. J. Heckman, D. J. Boccippio, H. J. Christian, and Z.-I. Kawasaki, 2001: A survey of thunderstorm flash rates compared to cloud top height using trmm satellite data. *Journal of Geophysical Research: Atmospheres*, **106 (D20)**, 24 089–24 095.

Veraverbeke, S., B. M. Rogers, M. L. Goulden, R. R. Jandt, C. E. Miller, E. B. Wiggins, and J. T. Randerson, 2017: Lightning as a major driver of recent large fire years in north american boreal forests. *Nature Climate Change*, **7 (7)**, 529–534.

Viemeister, P., 1961: *The lightning book*. MIT Press (MA).

Virts, K. S., J. M. Wallace, M. L. Hutchins, and R. H. Holzworth, 2013: Diurnal Lightning Variability over the Maritime Continent: Impact of Low-Level Winds, Cloudiness, and the MJO. *Journal of the Atmospheric Sciences*, **70 (10)**, 3128–3146, doi:10.1175/jas-d-13-021.1.

Vonnegut, B., 1963: Some Facts and Speculation Concerning the Origin and Role of Thunderstorm Electricity. *Severe Local Storms, Meteor. Monogr.*, 224–241.

Walser, A., D. Lüthi, and C. Schär, 2004: Predictability of precipitation in a cloud-resolving model. *Monthly Weather Review*, **132 (2)**, 560–577.

Wang, J.-X., J.-L. Wu, and H. Xiao, 2017: Physics-informed machine learning approach for reconstructing reynolds stress modeling discrepancies based on dns data. *Physical Review Fluids*, **2 (3)**, 034 603.

Wang, X., and J. He, 2011: Mythology of lightning in ancient china. *2011 7th Asia-Pacific International Conference on Lightning*, IEEE, 840–843.

Westerling, A. L., H. G. Hidalgo, D. R. Cayan, and T. W. Swetnam, 2006: Warming and earlier spring increase western us forest wildfire activity. *science*, **313 (5789)**, 940–943.

Weyn, J. A., D. R. Durran, and R. Caruana, 2019: Can machines learn to predict weather? using deep learning to predict gridded 500-hpa geopotential height from historical weather data. *Journal of Advances in Modeling Earth Systems*, **11 (8)**, 2680–2693.

Weyn, J. A., D. R. Durran, and R. Caruana, 2020: Improving data-driven global weather prediction using deep convolutional neural networks on a cubed sphere. *Journal of Advances in Modeling Earth Systems*, **12 (9)**, e2020MS002 109.

Whipple, F., 1929: On the association of the diurnal variation of electric potential gradient in fine weather with the distribution of thunderstorms over the globe. *Quarterly Journal of the Royal Meteorological Society*, **55 (229)**, 1–18.

Williams, E., and S. Stanfill, 2002: The physical origin of the land-ocean contrast in lightning activity. *Comptes Rendus Physique*, **3 (10)**, 1277–1292, doi:10.1016/S1631-0705(02)01407-X.

Williams, E. R., 1992: The Schumann Resonance : A Global Tropical Thermometer. *Science*, **256 (5060)**, 1184–1187, URL http://search.proquest.com/docview/213547553?pq-origsite=gscholar.

Wilson, C. T. R., 1920: Investigations on lightning discharges and on the electric field of thunderstorms. *Philos. Trans. Roy. Soc. London*, **221A**, 73–115.

Winn, W. P., C. B. Moore, and C. R. Holmes, 1981: Electric field structure in an active part of a small, isolated thundercloud. *Journal of Geophysical Research*, **86 (C2)**, 1187, doi:10.1029/jc086ic02p01187.

Winn, W. P., G. W. Schwede, and C. B. Moore, 1974: Measurements of electric fields in thunderclouds. *Journal of Geophysical Research*, **79 (12)**, 1761–1767, doi:10.1029/jc079i012p01761.

Wrangham, R. W., and Coauthors, 1999: The raw and the stolen: cooking and the ecology of human origins. *Current anthropology*, **40 (5)**, 567–594.

Yair, Y., 2018: Lightning hazards to human societies in a changing climate. *Environmental research letters*, **13 (12)**, 123 002.

Yanagawa, S., K. Yamamoto, Y. Naito, N. Takahashi, and M. Matsui, 2016: Investigations of lightning accidents on automobiles. *Electric power systems research*, **139**, 2–9.

Yoshida, S., T. Morimoto, T. Ushio, and Z. Kawasaki, 2009: A fifth-power relationship for lightning activity from tropical rainfall measuring mission satellite observations. *Journal of Geophysical Research: Atmospheres*, **114 (D9)**.

Zhao, M., and Coauthors, 2016: Uncertainty in model climate sensitivity traced to representations of cumulus precipitation microphysics. *Journal of Climate*, **29 (2)**, 543–560.

Zhou, X., Y. Zhu, D. Hou, Y. Luo, J. Peng, and R. Wobus, 2017: Performance of the new ncep global ensemble forecast system in a parallel experiment. *Weather and Forecasting*, **32 (5)**, 1989–2004.

Ziegler, C. L., D. R. MacGorman, and J. M. Straka, 2001: A Lightning Parameterization for Numerical Cloud Models. *Journal of Applied Meteorology*, **40 (3)**, 459–478.

Zipser, E. J., and K. R. Lutz, 1994: The vertical profile of radar reflectivity of convective cells: A strong indicator of storm intensity and lightning probability? *Monthly Weather Review*, **122 (8)**, 1751–1759.

VITA

Wei-Yi Cheng grew up in Taipei, Taiwan, where he experienced many different types of severe weather systems. Experiencing the power of thunderstorms and hurricanes help triggered a love and fascination with tropical deep convection. Wei-Yi attended college at National Taiwan University where he majored in Atmospheric Sciences. In 2012, Wei-Yi started graduate school at the National Taiwan University working with Dr. Hung-Chi Kuo, who focuses on the tropical convection and tropical cyclone dynamics. Throughout his time in graduate school in National Taiwan University, Wei-Yi earned his master's degree and published a peer-reviewed articles focused on the tropical cyclone boundary layer dynamics.

In 2015, Wei-Yi entered the PhD program at University of Washington working with Daehyun Kim in the department of Atmospheric Sciences, who focuses on tropical dynamics and earth's climate system. Throughout the time in the University of Washington, Wei-Yi published two peer-reviewed articles focused on the physical processes of tropical convection. In 2020, with the experience of tropical convection, Wei-Yi had an opportunity to collaborate with Dr. Robert Holzworth in the department of Earth and Space Sciences to work on a global lightning observation project. The results of the project have been presented in multiple conferences, including 2021 AMS annual meeting where he won an award for the best student presentation. Wei-Yi completed a Master of Science in Atmospheric Science in 2018 and his PhD in Atmospheric Science in June 2021.